DEVELOPMENT OF A NOVEL GALERKIN TRANSFORMED DIFFERENTIAL QUADRATURE METHOD AND ITS APPLICATION TO SIZE DEPENDENT NONLINEAR VIBRATION ANALYSIS OF FLUID CONVEYING CARBON NANOTUBES

A THESIS SUBMITTED TO
THE GRADUATE SCHOOL OF NATURAL AND APPLIED SCIENCES
OF
MIDDLE EAST TECHNICAL UNIVERSITY

BY

DOĞUHAN NURI KILIÇARSLAN

IN PARTIAL FULFILLMENT OF THE REQUIREMENTS
FOR
THE DEGREE OF MASTER OF SCIENCE
IN
MECHANICAL ENGINEERING

SEPTEMBER 2023

Approval of the thesis:

DEVELOPMENT OF A NOVEL GALERKIN TRANSFORMED DIFFERENTIAL QUADRATURE METHOD AND ITS APPLICATION TO SIZE DEPENDENT NONLINEAR VIBRATION ANALYSIS OF FLUID CONVEYING CARBON NANOTUBES

submitted by **DOĞUHAN NURI KILIÇARSLAN** in partial fulfillment of the requirements for the degree of **Master of Science in Mechanical Engineering Department, Middle East Technical University** by,

Prof. Dr. Halil Kalıpçılar
Dean, Graduate School of **Natural and Applied Sciences**
Prof. Dr. M.A. Sahir Arıkan
Head of Department, **Mechanical Engineering**

Prof. Dr. Ender Ciğeroğlu
Supervisor, **Mechanical Engineering, METU**

Examining Committee Members:

Prof. Dr. Yiğit Yazıcıoğlu
Mechanical Engineering, METU

Prof. Dr. Ender Ciğeroğlu
Mechanical Engineering, METU

Assoc. Prof. Dr. M. Bülent Özer
Mechanical Engineering, METU

Assoc. Prof. Dr. Bülent Özkan
Mechanical Engineering, Gazi University

Assist. Prof. Dr. Orkun Özşahin
Mechanical Engineering, METU

Date:04.09.2023

I hereby declare that all information in this document has been obtained and presented in accordance with academic rules and ethical conduct. I also declare that, as required by these rules and conduct, I have fully cited and referenced all material and results that are not original to this work.

Name, Surname: Doğuhan Nuri Kılıçarslan

Signature :

ABSTRACT

DEVELOPMENT OF A NOVEL GALERKIN TRANSFORMED DIFFERENTIAL QUADRATURE METHOD AND ITS APPLICATION TO SIZE DEPENDENT NONLINEAR VIBRATION ANALYSIS OF FLUID CONVEYING CARBON NANOTUBES

Kılıçarslan, Doğuhan Nuri
M.S., Department of Mechanical Engineering
Supervisor: Prof. Dr. Ender Ciğeroğlu

September 2023, 133 pages

In this thesis, nonlinear vibration characteristics of fluid conveying carbon nanotubes (CNT) are examined using nonlocal strain gradient theory (NSGT) to capture the small-scale effects. CNT is modeled with Euler-Bernoulli beam assumptions with large deflection nonlinearity using von-Karman assumptions and the effect of the nonlinearity on the instabilities caused by the fluid flow is considered. Spatial discretization is performed with the novel approach of Galerkin transformed differential quadrature method (GtDQM) which can apply different higher-order boundary conditions and obtain symmetric system matrices. The spatially discretized nonlinear equation of motion is then converted to nonlinear algebraic equations using the harmonic balance method (HBM) to be solved by Newton's method with pseudo-arc-length continuation. Critical flow velocities that cause instabilities are found and limit cycle oscillation (LCO) characteristics due to nonlinearity are obtained in the frequency domain instead of using time domain simulations. Finally, the effects of changing nonlocal and length-scale parameters on the LCO characteristics for different vibration amplitudes are examined.

Keywords: Nonlinear Vibrations, Carbon Nanotubes, Differential Quadrature Method, Fluid-Structure Interaction, Harmonic Balance Method

ÖZ

GALERKİN DÖNÜŞÜMLÜ DİFERANSİYEL TÜMLEV METODUNUN GELİŞTİRİLMESİ VE AKIŞKAN TAŞIYAN KARBON NANOTÜPLERİN BOYUTA BAĞLI DOĞRUSAL OLMAYAN TİTREŞİMLERİNİN İNCELENMESİNDE KULLANIMI

Kılıçarslan, Doğuhan Nuri
Yüksek Lisans, Makina Mühendisliği Bölümü
Tez Yöneticisi: Prof. Dr. Ender Ciğeroğlu

Eylül 2023 , 133 sayfa

Bu çalışmada, akışkan taşıyan karbon nanotüplerin (KNT) doğrusal olmayan titreşim özellikleri, küçük ölçekli etkileri yakalamak için yerel olmayan gerinim gradyan teorisi kullanılarak incelenmiştir. KNT, Euler-Bernoulli kiriş varsayımları ve von-Karman varsayımları kullanılarak yüksek deformasyon doğrusalsızlığı ile modellenmiştir ve doğrusalsızlığın akışkan akışının neden olduğu kararsızlıklar üzerindeki etkisi dikkate alınmıştır. Uzaysal ayrıklaştırma, farklı üst düzey sınır koşullarını uygulayabilen ve simetrik sistem matrisleri elde edebilen yeni geliştirilmiş Galerkin dönüştürülmüş diferansiyel tümlev metodu (GdDTM) ile gerçekleştirilmiştir. Mekansal olarak ayrıklaştırılmış doğrusal olmayan hareket denklemi daha sonra harmonik denge yöntemi kullanılarak doğrusal olmayan cebirsel denklemlere dönüştürülür ve sözde yay uzunluğu sürekliliği kullanan Newton yöntemiyle çözülmüştür. Zaman simülasyonu yerine frekans alanında kararsızlıklara neden olan kritik akış hızları bulunmuş ve doğrusal olmama nedeniyle oluşan sınır döngü salınımı özellikleri elde edilmiştir. Son olarak, yerel olmayan ve uzunluk ölçeği parametrelerinin değiştirilmesinin farklı titreşim büyüklüklerindeki sınır döngü salınımı özellikleri üzerindeki etkileri incelenmiştir.

Anahtar Kelimeler: Doğrusal olmayan titreşimler, Karbon Nanotüpler, Diferansiyel Kareleme Metodu, Akış-Yapı Etkileşimleri, Harmonik Denge Metodu

To my wife & cats

ACKNOWLEDGMENTS

I would like to thank many people who have contributed significantly to the completion of this thesis.

First, I am indebted to my advisor, Prof. Dr. Ender Ciğeroğlu for his knowledge, guidance, support, and encouragement to do my best.

Also, I would like to thank my dear friend Güneş Kösterit, who helped me solve the problems and gave me insights into different subjects. Working with you and exchanging ideas has been a real support.

I would also like to thank my family, whose support and love I have always felt for me.

Many thanks to my friends for their patience and support.

I am also grateful to Ash and Nacho, who uplifted me whenever I was bored or overwhelmed. You are the most beautiful and gluttonous cats in the world.

Finally and most importantly, I would like to express my eternal gratitude to my wife for her patience, sacrifices, and her love.

TABLE OF CONTENTS

CHAPTERS

APPENDICES

LIST OF TABLES

TABLES

LIST OF FIGURES

FIGURES

LIST OF SYMBOLS

α	Normalized nonlocal parameter
β^{ij}	Nonlinear coefficient between i^{th} and j^{th} coordinates
γ	Loss factor for structural damping
δ	Small distance measure
ε	Strain
η	Damping ratio for viscous damping
λ	Eigenvalue
ξ	Normalized length-scale parameter
ρ	Density
σ	Stress
ω	Frequency of vibration
$u(x,t)$	Axial mid-plane displacement
$w(x,t)$	Transverse mid-plane displacement
A	Area
E	Young's Modulus
I	Moment of area
L	Length
e_0a	Nonlocal parameter
l	Length-scale parameter
N	Size of the total number of nodes
$\boldsymbol{A}^{(n)}$	Derivative matrix of n^{th} order
$\boldsymbol{M}$	Mass matrix

$\boldsymbol{K}$	Stiffness matrix
$\boldsymbol{C}$	Viscous damping matrix
$\boldsymbol{P}$	Integral of products matrix
$\boldsymbol{T}$	Transformation matrix obtained from boundary conditions
$\boldsymbol{\mathcal{T}}$	Up-scaling matrix

Subscripts

b	Boundary
d	Domain
f	Fluid
NL	Nonlinear

Abbreviations

BC	Boundary conditions
CNT	Carbon nanotube
EVP	Eigenvalue problem
HBM	Harmonic balance method
LCO	Limit cycle oscillations
MD	Molecular dynamic

CET	Classical elasticity theory
NET	Nonlocal elasticity theory
SGT	Strain gradient theory
NSGT	Nonlocal strain gradient theory
GDQM	Generalized differential quadrature method
GtDQM	Galerkin transformed differential quadrature method

CHAPTER 1

INTRODUCTION

1.1 Linear and Nonlinear Vibration Analysis

Vibration analysis is one of the most important steps of any product design that requires structural parts. Even if a design may withstand static loads applied by the working environment, it may fail to endure excessive loads occurring during oscillatory motion, especially if the excitation is around the resonance of the system. Furthermore, cyclic repetitive loads applied may also cause fatigue damage to the structure and cause failure even if the amplitude of the load is well within a tolerable range. Hence, vibration analysis is a well-investigated area of structural analysis and has developed very significantly over the decades.

While early into the 20^{th} century, solution methods ranged from analytical solutions to basic perturbation techniques. Around the middle of the century importance of vibration analysis became much more clear and different analytical methods have been developed, as well as numerical methods have emerged that can employ upcoming computational tools. This era of vibration research focused on the model size reduction by different methods such as modal reductions or condensations due to lack of computational power, or incorporation of time-dependent effects into the frequency domain analysis.

As the computational power became more abundant and easier to use more efficient and advanced designs could be made such that linear analysis was becoming insufficient. Hence, the focus of vibration research started to turn towards nonlinear analysis, especially in the frequency domain, which is still researched up to date as the state of the art. This increased effort led to truer vibration analysis and smart ways of using nonlinear structures for much more efficient designs. For example, introducing frictional losses to systems not only moves the resonance region further away but also lowers the peak amplitude along with it or the design of considerably smaller parts with snap-through configurations of small beams. Alongside the effective and advanced design nonlinear vibration analysis also led to the predictions of possible catastrophic failures such as flutter instabilities.

1.2 Applications of Carbon Nanotube

After Iijima produced the first carbon nanotubes (CNT) [1] world was very interested in this unusually small stable structure. Considering impressive structural strength, and very high thermal and electrical conductivity (in some cases it may be semi-conducting), the interest of many researchers focused on determining efficient production, determination, and prediction of material properties [2].

To obtain material or geometric properties of CNTs experiments may be conducted [3], since conducting experiments at the nanoscale is a challenge and costly endeavor, those properties instead be obtained by molecular dynamic simulations [4], even molecular dynamic simulations might be computationally expensive, such that continuum mechanics may also be used to predict the properties [5]. Note that, as the cost/effort gets lower accuracy also gets worse.

Even though CNTs have yet to deliver on the premise they were initially marketed as they are finding new areas of application such as mass sensing sensors at nanoscales [6] and its control algorithm that incorporates the geometric nonlinearity effect [7] or CNT is used as a reinforcement agent which increases the capacitance of a battery. Moreover, CNTs are also being applied for medical use such as biosensors [8] or even as a part of targeted cancer treatment methods.

1.3 Objectives and Outline

As will be summarized in the literature review chapter of this thesis, instabilities or structural property changes caused by fluid flow inside a tube (such as CNT) is an important problem in the analysis of CNTs. Considering time domain integration is a very slow method for nonlinear analysis, which is needed to explain behavior near instability of fluid conveying CNTs, frequency domain solution of such nonlinear structures becomes important.

Hence, the need for developing an efficient analysis method that should be able to produce results and predict instabilities in the frequency domain for geometrically nonlinear CNTs conveying a fluid flow has arisen and the objective of this thesis is to satisfy those needs.

While achieving the aforementioned objectives, there were several novel contributions to the literature such as:

- Modification of GDQM [9] to increase its stability, convergence rate, and areas of use for spatial discretization of the problem
- A new method of finding critical instability speed without solving the state space eigenvalue problem
- A new method of prediction for nonlinear post-buckling and post-flutter critical speeds in the frequency domain without the need for a time domain simulation
- A new method of obtaining the stable regime for a given maximum allowed deflection while changing a design parameter

In chapter two, a literature review will be given focusing on numerical solution methods, and small-scale elasticity theories that are needed to model CNTs and fluid-structure interaction.

Following that in chapter three, mathematical derivations will be completed which include the mathematical background for GDQM, novel parts added to the GDQM framework, nonlinear solution methods that will be utilized, and equation of motion for fluid conveying small-scale tubes.

In chapters four and five, obtained results will be presented; where chapter four focuses on the verification of newly proposed additions to the GDQM will be done with different basic case studies and chapter five focuses on results obtained for the critical speeds for instabilities, response-dependent evolution of critical speed, and effects of different parameters on critical speeds.

Finally, in the sixth chapter, a general summary will be given and the results obtained will be discussed, more importantly, possible directions for future work to take will be explained in great detail.

CHAPTER 2

LITERATURE REVIEW

In this section, brief reviews will be given for the respective topics that will be covered in this thesis. Since summarizing all the previous work for all the topics covered would be considerably wrong and is not generally in the scope of a master of science program. Hence, only relative information that will get the reader up to date will be summarized and most repetition studies or some tangent topics will not be included.

Although the sections of this chapter can include information that is relevant to either topic, most information can be divided up into three general topics which are numerical methods, size-dependent elasticity theories, and fluid conveying micro/nanotubes.

2.1 Numerical Methods

Many numerical solution techniques have emerged to handle nontraditional boundary conditions of varying types of differential equations that are used in many different fields of study. One such technique is Differential Quadrature Method (DQM). First proposed by Bellman and Casti [10], DQM aims to approximate derivatives of a function on a discretized domain using weighted function values inside that domain. However, due to problems while obtaining the weighting coefficients [11], DQM was not used until Shu and Richards [9, 12] formulated DQM into a much more stable form using Lagrange interpolating polynomials which is called Generalized Differential Quadrature Method (GDQM).

With this form, GDQM is used to solve problems that cannot be handled with the continuous solution approach due to nontraditional boundary conditions, non-uniform system properties, and/or complex nonlinear differential equations from different domains including structural mechanics [13–16], fluid mechanics [9, 17, 18], and even theoretical physics [19–21]. Since Lagrange interpolating polynomials do not necessarily satisfy boundary conditions, problem-specific boundary conditions need to be implemented in the formulation.

Implementation of boundary conditions can range from changing the final weighting coefficients [22] to cleverly manipulating the intermediate weighting coefficients [23, 24], however, the most general use case is to express points at the boundary in terms of points at the internal points by using boundary condition equations [25]. The latter method makes the GDQM very flexible in terms of problems it can be used on, and one of the easiest methods for general use. Yet, this formulation suffers by just solving the boundary condition equations at the points that are at the boundaries, instead of solving both boundary conditions and equations of motion. Moreover, higher-order differential equations need closely spaced grid points separated by δ, which can cause instabilities and convergence problems. Implementing higher-order boundary conditions without using the δ technique saw many attempts, from trying to use imaginary grid points outside the domain [26] to using extra imaginary grid points compromised of derivatives of boundaries [27, 28]. A more recent boundary condition application that tries to amend this problem proposes not using Dirichlet-type boundary conditions [29] or reformulation of a higher-order differential equation into several second-order differential equations [30].

In this thesis, it will be shown that the first problem is caused by the wrongful application of static condensation [22] and can be mended with a correct application of static condensation, in which boundary condition equations can be used as a coordinate transformation from internal points to the whole domain. By solving the first problem, the need for the δ technique becomes obsolete and the second of those problem is also solved. Moreover, using this transformation approach to applying boundary conditions allows us to use Galerkin weighted residual method [31] to make the final system matrices symmetric without determining a trial function. Galerkin method increases the stability and convergence rate of the solution compared to the collocation method which is analogous to the GDQM [27].

2.2 Size-Dependent Elasticity Theories

For micro/nano-sized structural components, theoretical analysis using classical elasticity theory fails to predict behavior observed with experiments[32] or ab inito molecular dynamic simulations[33–35]. This problem can be mended with different theoretical methods, in which two main techniques will be used in this thesis.

One such technique is to employ higher-order strain gradients in the strain energy formulation, such that strain energy is still linear but also has more material parameters than the two used in classical elasticity (Young's modulus and Poisson ratio or Lame's parameters). The other technique that will be discussed is to incorporate the stresses applied to a point originating from finitely separated points instead of only using the stresses originating from infinitesimally separated points.

2.2.1 Strain Gradient Theories

Formulating an elasticity theory that also has higher-order derivatives, analogous to increasing the order of approximation in Taylor series expansion, is first done by Mindlin and Tiersten[36], and Toupin [37] in 1962 using couple forces created by classical stresses. The idea is then further expanded by Mindlin [38] to obtain a more general expression containing all necessary derivatives in 1964. In 1965 Mindlin [39] simplified the theory to only employ second-order gradients at most such that only five independent new material length scale parameters are introduced to classical two which was named strain gradient theory (SGT).

Due to a lack of interest in micro/nanostructures at the time and the infeasible requirement of determining 7 material parameters experimentally before predicting any result, strain gradient theory was not used until three decades later when Fleck and Hutchinson used the strain gradient theory to obtain strain gradient plasticity theory in 1997 [40] and further refined it in 2001 to use less material parameters in 2001 [41].

Using similar simplifications modified couple stress theory (MCST) is developed by Yang et al. in 2002 [42] where the couple stresses are used as the reason for the higher-order gradient. By eliminating the strains that do not affect the strain energy they were able to obtain only a single material length scale parameter on top of the two classical ones. Lam et al. in 2003 [32] proposed the modified strain gradient theory (mSGT) where all necessary derivatives of the higher-order displacement gradient are used but refined to only include strain gradients that contribute to the strain energy, in which only three extra independent length scale parameters exist.

Those two theories are still being used without much change over the past two decades; from beams that employ linear Euler-Bernoulli kinematic assumptions [43,44] to nonlinear Euler-Bernoulli kinematic assumptions [45, 46]. Furthermore, to consider the rotational motion of beams, Timoshenko or Reddy-Levinson kinematic assumptions are solved for linear [13, 47–51] and nonlinear [14, 52] cases. mSGT and MCST are also used for plates [53–56], yet are not delved much deeper since the focus of the thesis is on the beams.

If the higher-order strain theory is used, whether it be MCST or mSGT, the resulting equation of motion has higher derivative orders and accordingly has more boundary conditions[57]. Due to these higher-order equilibrium equations and respective boundary conditions, analytical solutions as well as approximate results that employ numerical methods that use trial functions (such as Galerkin or Ritz [31]) are much harder to obtain, thus, more flexible numerical methods such as DQM is prevalent. For all physical applications of MCST or mSGT with different kinematic assumptions, the only effect is to increase the overall stiffness and produce a hardening effect for shortening length [58].

2.2.2 Nonlocal Theories

Another approach to considering length-scale effects for elasticity is to model the structure as a nonlocal one, where stresses not only affect the local region but also influence the regions that are relatively distant in the domain. This can be achieved using molecular dynamics by adding all of the intermolecular forces affecting a single atom and considering the motion of each atom one by one [59]. However, this method is very computationally expensive and virtually impossible to apply to relatively larger domains.

One can change the summation to an integration by assuming the domain is big enough to consider the intermolecular forces as a continuous function instead of emanating from discrete atoms. With this assumption, intermolecular forces can be approximated by pairwise force functions, and the integration of this force over the volume produces a continuous force field on every point in the domain. This theory is called the peridynamic theory [60, 61], which is most generally used to study the effects of cracks or discontinuities in the domain such as grain boundaries.

One further simplifying assumption is approximating intermolecular forces as stresses of classical elasticity that are caused by strains over some range of values. This was first formulated by Eringen in 1972 [62] and verified by obtaining dispersion solutions that can also be obtained by lattice dynamics at the length scale of atoms. It is further refined in 1983 by Eringen [63] by defining a nonlocal stress constructed by integrating local (classical) stresses over the domain of the body with a kernel function defined with specific properties and a nonlocal parameter such that a differential form can be attained using Green's function.

Similar to SGT, nonlocal elasticity theory (NET) had not seen widespread use until two decades earlier when it was popularized by Peddieson et al. [64] and Reddy[65]. Nearly unchanged over four decades NET is still being used to analyze beams [64–70] and plates [71, 72]

Although NET has excellent prediction power for wave solutions, dispersion, and attenuation curves; when used for static or free vibration solutions there were some problems with this theory where it might predict softening effects which is not seen in micro length scale but may present itself on macro scales[57]. Moreover, there are paradoxical solutions where nonlocality does not affect some boundary conditions [73], or obtaining opposite effects (softening/hardening) with different formulations (integral or differential) on some boundary conditions[74]. Even though these problems can be mended with different techniques [73, 75], it is an indication that this theory may not be a 'final' theory.

2.2.3 Nonlocal Strain Gradient Theory

Failure to predict correct dispersion relations of mSGT and failure to capture the hardening at micro scales can be mended by combining both of the theories to obtain a nonlocal strain gradient theory (NSGT). Unification of both theories with mathematical rigor has not been done until this point, yet in 2015 Lim et al. [76] combined the general effect of both theories with some simplifying assumptions. Such as using a single material length scale instead of three for mSGT, also using the same kernel function with the same parameters for both classical and higher-order stresses, moreover only expanding the terms up to linear dependence on nonlocal parameter.

In light of those simplifying assumptions, NSGT is still very effective in both of the shortcomings of these theories. Compared with molecular dynamic simulations, NSGT results have a good match for free vibration [77], wave propagation [76, 78], and static deflections [79]. NSGT is also used to analyze linear [80, 81] and nonlinear [82–84] beams as well as plates [85, 86].

NSGT solves the problem of extra boundary conditions needed for a higher-order theory obtained from strain gradients as well as the hardening effect for bending and natural frequencies which needed an aspect ratio dependent variable nonlocal parameter to be able to explain molecular dynamic simulations for NET[68]. Moreover, it predicts an asymptotic phase velocity [78] which can only be done with NSGT, however, this needs to be verified since available molecular dynamic data [87] does not cover the range needed to observe the effect.

Another advantage of NSGT is when the length scale parameter is taken to be zero NET is directly recovered while some simplified version of mSGT can be obtained by taking the nonlocal parameter as zero.

2.3 Fluid Conveying Carbon Nanotubes

While a tube is carrying a flowing fluid, whether it be a gas or a liquid, it is prone to instabilities due to fluid motion, caused by structural motion, increasing the structural motion further in a feedback loop [88].

According to Païdoussis[89] fluid-structure interaction for such a flow can be modeled by including the kinetic energy of the flowing fluid into the equation of motion of the structural part since the fluid itself can be assumed to have no potential energy storage capabilities but only viscous energy dissipation to an approximation. While considering this assumption, the flow's velocity field is assumed to be an equivalent uniform one which is not realistic and can be addressed by the correction made to the centrifugal term by Guo et al. [90].

Another correction to flow can be done by considering the no-slip boundary condition may not be applicable in micro and nano-sized channel flows as given by Beskos & Karniadakis [91] and flow velocity for nanotubes must be scaled accordingly [91,92]. There are also trying to model the fluid flow using simplified Navier-Stokes equations[93, 94], however, those studies are lacking the sources of equations or assumptions made to achieve those.

Following different elasticity theories and kinematic assumptions with different fluid-structure interaction modeling, many researchers obtained results for the case of fluid conveying micro/nanotubes. These researchers showed their findings using different methods such as; instability diagrams obtained by solving the eigenvalue problem (EVP) in state space form, bifurcation or phase diagrams obtained by time domain simulations, dispersion curves obtained by analytical manipulations, and frequency response functions (FRFs) using varying methods.

Initially, the problem of fluid conveying CNTs were being studied with CET, for example, Yoon et al. [88] examined instabilities of equivalent beam models using Galerkin method to discretize the spatial domain and assuming harmonic time response or Ni et. al. [95] used solved the same problem using DQM, Wang et al. [96] examined the temperature effects on instabilities of equivalent beam model with DQM to discretize spatial domain and assuming harmonic time response, Ghavanloo et al. [97] examined the instabilities of equivalent beam models using finite element methods (FEM) to discretize the spatial domain and assuming harmonic time response.

Further studies were conducted by NET, for example, Lee and Chang [98] examined instabilities of equivalent beam model with an analytical spatial solution assuming harmonic time response, Dai et al, [99] examined instabilities of the geometrically nonlinear equivalent beam with a post-buckling response by discretizing the spatial domain with Galerkin method and assuming harmonic time response, Askari and Esmailzadeh [100] studied instabilities and obtained FRFs of equivalent beam model on a foundation with quadratic and cubic nonlinearity by discretizing the spatial domain with Galerkin method and using the method of multiple scales (MMS) [101],

On the other side, MCST studies were conducted by Wang [102] to examine instabilities of an equivalent beam model with DQM spatial discretization and assuming harmonic time response and Aghazadeh [103], to study instabilities of axially functionally graded equivalent beam model by using DQM to discretize and assuming harmonic solutions. Moreover, Ansari et al. [104] used mSGT to study the instabilities of an equivalent beam model with geometric nonlinearity by discretizing using DQM and using the harmonic balance method (HBM) for temporal the solution.

After the combined theory of NSGT emerged, researchers mostly used NSGT to analyze the fluid conveying CNT problem. Li and Hu [78], studied wave dispersion of equivalent beam model by using analytical methods;

Mohammadi et al. [105] examined instabilities of shell model with DQM for spatial discretization and assuming harmonic time response, Li et al. [106], examined instabilities of equivalent beam model by using Galerkin method to discretize spatial part and using analytical solution for temporal part; Zhen and Zhou [107], studied wave dispersion relation under magnetic field effects of equivalent beam model by analytically solving it; Farajpour et al. [108], obtained FRF of equivalent beam model with geometric nonlinearity used Galerkin method to discretize the spatial domain and left out time temporal solution method with a mention of frequency continuation; Bahaadini et al. [109], examined instabilities of equivalent beam model by using Galerkin method to discretize and assuming temporal solution; Farajpour et al. [110], examined bifurcation and phase diagrams of geometrically nonlinear equivalent beam model by discretizing it with Galerkin method and using time domain integration; Ghane et al. [111], examined instabilities under magnetic field effects of equivalent beam model by using DQM to discretize and assuming harmonic time response;Atashafrooz et. al. [112] studied examined instabilities including surface effects of equivalent beam model by using Galerkin to discretize and assuming harmonic time response; Jin and Ren [113], examined bifurcation diagrams and obtained FRF of pre- and post- buckled configurations of equivalent beam models with geometric nonlinearity using Galerkin method for spatial discretization and the modified Lindstedt–Poincaré (MLP)[114] for temporal solution.

A summary of the fluid conveying CNT literature is given in table 2.1. The lack of nonlinear solutions that employ the pseudo-arc-length continuation method or HBM in obtaining solutions can easily be seen, which is one of the motivations of the current study.

2.3.1 Validity of Water Flow Inside a Carbon Nanotube

Considering the smallest length scales defining the fluid motion as a flow becomes questionable. Theories and results from experiments for fluid conveying micro and nano channels are extensively investigated by Karniadakis and Beskok [115], while the focus is more on the micro channels, results for nano channels are also included. Even though collected literature at the time agrees that the gaseous fluid flow can be predicted by current theories, aqueous flows does not obey the respective theories.

For that, molecular dynamic simulations or experimental investigations needs to be carried out to fully explain the water flow through a CNT, especially for a smaller diameter ones. Earliest experimental results comes from the Israelachvili in 1992 [116], where the change between bulk continuum motion to a quantized plug-like motion is investigated. For the water confined between two layers continuum mechanics starts to fail around 2 nm separation which approximately corresponds to 10 molecular length. It is noted that beyond that length scale, motion may be approximated as a continuum but there would be plug-like motion caused by the intermolecular interactions. These findings are later extended to water flow confined by CNTs of varying diameter by Thomas and McGaughey in 2009 [117] using molecular dynamic simulations. Since motion of each water molecule can be simulated and tracked, separation from bulk motion to the plug-like motion are reported to be occurring for the smaller diameters then 1.39 nm which corresponds to the (10,10) CNT. Simulations are carried below that diameter up to 0.83 nm diameter of (6,6) CNT. Even at the smallest scale pressure-driven flow can be observed even thought correction factors becomes unpredictable by continuum theories.

Similarly 0.81 nm diameter (6,6) armchair CNT is examined using molecular dynamic simulations by Hummer et al. [118]. Motion is noted to be chain-like without detail, however main focus was on the flow rate of the water where much higher intermolecular forces between water molecules are noted to cause hydrophobic properties to the CNTs without any special treatments. Due to higher flow rates caused by hydrophobic property of CNTs, it was theorized that it can be used as an efficient diffusion membrane. This theoretical prediction was later proved by Majumder et al. [119] for 7 nm pores and by Holt et al. [120] for 2 nm pores in a membrane, where the pores are constructed from CNTs. Predicted higher flow rate compared to bigger pore sizes are observed which increases as the CNT diameter gets smaller. Those experimental work are also modeled in detail by Thomas et al. [121] using molecular dynamic simulations where the motion characteristics are examined which have not yet been achieved in experimental setups.

For more information in water flowing through carbon nanotubes, a small review like article of Kannam et al. [122] may be used where the results validates the ability of water to flow through CNTs as small as (6,6) CNTs both with molecular dynamic simulations and experiments. Even though properties to be used in this thesis, (5,5) armchair CNT with 0.7 nm inner diameter, is not actually verified using experimental methods, flow is validated using molecular dynamic simulations while examining it in the use of diffusion membranes or syringes [123, 124]. More recently in 2021 ab-inito molecular dynamic simulations are used to simulate the desalination of water inside the CNT [125] to be used in desalination membranes.

Evidence to the validity of the water to flow through (5,5) CNT is shared with varying degrees of confidence, even if the fluid motion corresponding to a pressure gradient may need special methods to handle, since in this work CNT and water are taken to be not interacting (as is discovered by experiments) characteristics of the fluid-structure interaction should not change. If in the future, the experiments are done for the (5,5) CNT, fluid-structure interaction model can also be improved with the experimental results, likely without changing the logic behind the proposed method.

Table 2.1: Literature Review Summary

Reference	Year	Elasticity	Results	Spatial	Temporal	Nonlinearity
[88]	2005	CET	Instability	Galerkin	EVP	Linear
[96]	2008	CET	Instability	DQM	EVP	Linear
[98]	2008	NET	Instability	Analytical	EVP	Linear
[97]	2010	CET	Instability	FEM	EVP	Linear
[102]	2010	MCST	Instability	DQM	EVP	Linear
[95]	2011	CET	Instability	DQM	EVP	Linear
[104]	2014	mSGT	Instability	DQM	HBM	Geometric
[99]	2015	NET	Instability	Galerkin	EVP	Geometric
[78]	2016	NSGT	Dispersion	Analytical	Analytical	Linear
[106]	2016	NSGT	Instability	Galerkin	Analytical	Linear
[100]	2017	NET	Instability&FRF	Galerkin	MMS	Foundation
[107]	2017	NSGT	Dispersion	Analytical	Analytical	Linear
[105]	2018	NSGT	Instability	DQM	EVP	Linear
[108]	2018	NSGT	FRF	Galerkin	-	Geometric
[110]	2019	NSGT	Bifurcation	Galerkin	Integration	Geometric
[109]	2019	NSGT	Instability	Galerkin	EVP	Linear
[111]	2020	NSGT	Instability	DQM	EVP	Linear
[112]	2020	NSGT	Instability	Galerkin	EVP	Linear
[103]	2022	MCST	Instability	DQM	EVP	Linear
[113]	2022	NSGT	Bifurcation&FRF	Galerkin	MLP	Geometric

CHAPTER 3

MATHEMATICAL DERIVATIONS

In this section detailed mathematical derivations will be given for the novel method used for discretizing the equations of motion and also the equations of motion for the given problem. Since different topics are presented from structural mechanics, fluid mechanics, and numerical methods, great detail is given in each step of the derivation for the ease of following with different backgrounds in mathematics.

First, the summary of DQM will be given, followed by the novel additions to the method. Next, the methods used to solve nonlinear equations of motion will be summarized. Finally, fluid conveying tube equations will be derived and the implementation of earlier numerical methods will be summarized.

3.1 Generalized Differential Quadrature Method

To derive and differentiate the new methods presented in this paper in a self-consistent manner, a description of the GDQM formulation as well as common ways of applying boundary conditions is presented.

3.1.1 Differential Quadrature Coefficients

The DQM uses the premise that a derivative of a function at a point can be approximated in terms of the superposition of values of the function at a domain of points including the original point [10]. Which can be shown for the m^{th} derivative of a continuous function $f(x)$ at a discrete point x_i as

$$\left.\frac{\partial^m f}{\partial x^m}\right|_{x=x_i} = f^{(m)}(x_i) = \sum_{j=1}^{N} A_{ij}^{(m)} f(x_j), \tag{3.1}$$

where $A_{ij}^{(m)}$ are predetermined weighting coefficients that relate function values in the domain to the value of m^{th} order derivative at a point in the same domain, $f^{(m)}(x_i)$ is the shorthand notation that is m^{th} order derivative of the function $f(x)$ at the $x = x_i$ point, and N is the number of points sampled in the x-direction. It can be observed that this equation is a matrix-vector multiplication using index notation, so if all the values of the m^{th} order derivative need to be obtained in the given domain with N sample points a vector of derivative values can be acquired from a vector of function values at specified domain points by a matrix multiplication, which can be shown as

$$\boldsymbol{f}^{(m)} + \boldsymbol{\xi} = \boldsymbol{A}^{(m)} \boldsymbol{f} \tag{3.2}$$

Notation of bold capital letters denoting matrix and bold lower case letters denoting vector, regular capital letters with two indices denoting entries of a given matrix, and regular lower case letters with a single index denoting entries of a given vector are used hereafter. The problem then becomes how to determine the weighting coefficient matrix and possible grid point applications. If the function $f(x)$ can be expressed with good accuracy using test functions in the given domain, the weighting coefficient matrix $\boldsymbol{A}^{(m)}$ can be calculated beforehand irrespective of the used function. The popularity of the DQM method increased with the usage of Lagrange interpolation polynomials as test functions since it had a closed-form expression derived by Shu and Richards [9, 12] that is called Generalized DQM (GDQM), whose weighting coefficients for the first derivative is expressed as

$$A_{ij}^{(1)} = \begin{cases} \dfrac{M(x_i)}{(x_i - x_j)\, M(x_j)}, & \text{for } i \neq j, \quad i,j = 1,2,\ldots,N \\ -\displaystyle\sum_{k=1,k\neq i}^{N} A_{ik}^{(1)}, & \text{for } i = j, \quad i,j = 1,2,\ldots,N \end{cases}, \tag{3.3}$$

where the Lagrange interpolating polynomial is $L(x_i) = \frac{M(x_i)}{M(x_j)}$ and $M(x_i)$ is defined as

$$M(x_i) = \prod_{k=1,k\neq i}^{N} (x_i - x_k) \tag{3.4}$$

The higher-order derivative weighting coefficient matrix can be obtained either as a matrix multiplication of the first-order derivative matrix with the one lower-order derivative matrix as

$$\boldsymbol{A}^{(\boldsymbol{m})}=\boldsymbol{A}^{(\boldsymbol{1})}\boldsymbol{A}^{(\boldsymbol{m-1})} \tag{3.5}$$

or with a recurrence relation given by

$$\begin{aligned} A_{ij}^{(m)} =& m\left(A_{ii}^{(m-1)}A_{ij}^{(1)}-\frac{A_{ij}^{(m-1)}}{x_i-x_j}\right) \text{ for } i,j=1,2,\ldots,N \\ & \text{and } \ i\neq j \text{ and } \ m=2,3,\ldots,N-1 \end{aligned} \tag{3.6}$$

where diagonal terms can be calculated like done in equation (3.3).

Equally spaced grid points to define the domain is a natural and easy-to-implement method, however, while solving equations of motion, more points are needed near boundaries. Hence a more stable and more accurate [126] choice of grid points is to use Gauss-Lobatto-Chebyshev points that are given by

$$x_i=\frac{1}{2}\left(1-\cos\frac{(i-1)\,\pi}{N-1}\right) \qquad i=1,2,\ldots,N \tag{3.7}$$

For the rest of the thesis weighting coefficients obtained by the GDQM method will be employed, however, in principle other weighting coefficients [127] can similarly be manipulated to obtain similar results. For example, an Euler-Bernoulli beam equation and its discretized GDQM partner can be written as

$$\begin{aligned} EI\frac{\partial^4 w}{\partial x^4}+\rho A\frac{\partial^2 w}{\partial t^2}=q, \ \ EI\sum_{j=1}^{N}A_{ij}^{(4)}w(x_j,t)+\rho A\ddot{w}(x_i,t)=q\left(x_i,t\right) \\ i=1,2,\ldots,N \end{aligned} \tag{3.8}$$

where EI, ρ, A, w, $\ddot{w}$ and q are flexural rigidity, density, cross-sectional area, transverse deflection, transverse acceleration of the beam and distributed transverse load, respectively. Equivalently the GDQM equation can be shown in matrix form as

$$EI\boldsymbol{A}^{(\boldsymbol{4})}\boldsymbol{w}+\rho A\boldsymbol{I}\ddot{\boldsymbol{w}}=\boldsymbol{q} \tag{3.9}$$

where $\boldsymbol{I}$ is the identity matrix with adequate size. Since matrix form is cleaner and easier to interpret for certain cases, mostly matrix form will be used while using GDQM unless a new definition is being done. Using the matrix definition static deflection, buckling, free vibration, or forced vibration analysis can be done as if any other discretization method is used. Note that, this example of the Euler-Bernoulli beam will be used while explaining the method at hand.

3.1.2 Implementation of Boundary Conditions

To solve differential equations with this method, boundary conditions that define the boundaries of the problem domain need to be applied. These boundary conditions can be written in terms of weighting coefficient matrices in the most general form as

$$B_{ij}\left(A_{ij}^{(1)}, A_{ij}^{(2)}, \ldots, A_{ij}^{(N-1)}\right) = g_i \;\; i = 1, 2, \ldots, M, \quad j = 1, 2, \ldots, N \tag{3.10}$$

where $\boldsymbol{B_{M\times N}}$ is the matrix that gives boundary conditions, M is the number of boundary conditions, and $\boldsymbol{g}$ is the vector for a general equated factor of the boundaries which generally take the value $\mathbf{0}$.

It should be noted that for problems that have more than one boundary equation at a single point, δ-point technique is generally employed which changes the grid point distribution such that there is more than one point very near to the boundary which is separated by δ amount (generally in the order of $\sim 10^{-5}$). For example, to describe two boundary points that can be used for four boundary conditions of the Euler-Bernoulli beam equation, the grid points can be selected as

$$\begin{aligned} &x_i = \frac{1}{2}\left(1 - \cos\frac{(i-2)\,\pi}{N-3}\right) \qquad i = 1, 3, 4, \ldots, (N-2)\,, N \\ &\text{and } x_2 = x_1 + \delta,\; x_{N-1} = x_N - \delta \end{aligned} \tag{3.11}$$

At this point, it should be noted that usage of δ-point technique generally causes stability and convergence problems since the numerical scale of distance between two boundary points is very different from the distance between two inner nodes.

Finally, to make matrices easier to work with boundary points can be reordered to appear at the top part of the matrices, such as

$$EI\begin{bmatrix} \boldsymbol{A_{bb}^{(4)}} & \boldsymbol{A_{bd}^{(4)}} \\ \boldsymbol{A_{db}^{(4)}} & \boldsymbol{A_{dd}^{(4)}} \end{bmatrix}\begin{Bmatrix} \boldsymbol{w_b} \\ \boldsymbol{w_d} \end{Bmatrix} + \rho A\begin{bmatrix} \boldsymbol{I} & 0 \\ 0 & \boldsymbol{I} \end{bmatrix}\begin{Bmatrix} \boldsymbol{\ddot{w}_b} \\ \boldsymbol{\ddot{w}_d} \end{Bmatrix} = \begin{Bmatrix} \boldsymbol{q_b} \\ \boldsymbol{q_d} \end{Bmatrix} \tag{3.12}$$

where $\mathbf{0}$ is the matrix, whose elements are zero with adequate size and subscript b, d donate to grid points that represent boundary points and internal domain points, respectively.

Current methods of boundary condition applications can be divided into three parts, each having its own pros and cons.

Method 1: Direct Replacement

The most basic method of applying boundary conditions is to replace the equation of motion with boundary condition equations that correspond to boundary points. For the example of both ends simply supported Euler-Bernoulli beam problem boundary conditions can be written in a discretized form as

$$w_1 = 0, \quad \sum_{j=1}^{N} A_{1j}^{(2)} w_j = 0, \quad \sum_{j=1}^{N} A_{Nj}^{(2)} w_j = 0, \quad w_N = 0 \tag{3.13}$$

and using the boundary conditions instead of the equation of motion the modified equation of motion with boundary conditions is written as

$$EI \begin{bmatrix} \boldsymbol{B_{bb}} & \boldsymbol{B_{bd}} \\ \boldsymbol{A_{db}^{(4)}} & \boldsymbol{A_{dd}^{(4)}} \end{bmatrix} \begin{Bmatrix} \boldsymbol{w_b} \\ \boldsymbol{w_d} \end{Bmatrix} + \rho A \begin{bmatrix} 0 & 0 \\ 0 & \boldsymbol{I} \end{bmatrix} \begin{Bmatrix} \boldsymbol{\ddot{w}_b} \\ \boldsymbol{\ddot{w}_d} \end{Bmatrix} = \begin{Bmatrix} \boldsymbol{0} \\ \boldsymbol{q_d} \end{Bmatrix}, \tag{3.14}$$

where the boundary condition sub-matrices can be written as

$$\boldsymbol{B_{bb}} = \begin{bmatrix} 1 & 0 & 0 \\ A_{11}^{(2)} & A_{12}^{(2)} & A_{1(N-1)}^{(2)} \\ A_{N1}^{(2)} & A_{N2}^{(2)} & A_{N(N-1)}^{(2)} \\ 0 & 0 & 0 \end{bmatrix} \quad \boldsymbol{B_{bd}} = \begin{bmatrix} 0 & \cdots & 0 \\ A_{13}^{(2)} & \cdots & A_{1(N-2)}^{(2)} \\ A_{N3}^{(2)} & \cdots & A_{N(N-2)}^{(2)} \\ 0 & \cdots & 0 \end{bmatrix} \tag{3.15}$$

As it can be seen using equation (3.7) not only $i = 1, N$ points are used as boundaries but also $i = 2, N - 1$ are used as boundary points and written on the top side of the matrix for convenience.

Method 2: Indirect Replacement (Modifying weighting coefficient matrices)

Another way of implementing boundary condition which gives better accuracy and stability is to implement the boundary conditions into the lower order weighting coefficients before writing the equation of motion [23, 24]. So that both the boundary condition equation and the equation of motion can be solved simultaneously on the boundary points, which is actually what is needed.

To illustrate simply supported end conditions for the Euler-Bernoulli beam are built into the second-order matrix. For both boundaries, displacement boundary condition $(w_1 = w_N = 0)$ is written as

$$\bar{\boldsymbol{A}}^{(\mathbf{1})}\boldsymbol{w} = \begin{Bmatrix} w_1^{(1)} \\ w_2^{(1)} \\ \vdots \\ w_{(N-1)}^{(1)} \\ w_N^{(1)} \end{Bmatrix} = \begin{bmatrix} 0 & A_{12}^{(1)} & \cdots & A_{1(N-1)}^{(1)} & 0 \\ 0 & A_{22}^{(1)} & \cdots & A_{2(N-1)}^{(1)} & 0 \\ \vdots & \vdots & \cdots & \vdots & \vdots \\ 0 & A_{(N-1)2}^{(1)} & \cdots & A_{(N-1)(N-1)}^{(1)} & 0 \\ 0 & A_{N2}^{(1)} & \cdots & A_{N(N-1)}^{(1)} & 0 \end{bmatrix} \begin{Bmatrix} w_1 \\ w_2 \\ \vdots \\ w_{(N-1)} \\ w_N \end{Bmatrix} \tag{3.16}$$

so that w_1 and w_N coordinates do not affect higher-order derivatives and act as if they are zero. Following that, the second derivative can be written as

$$\bar{\boldsymbol{A}}^{(\mathbf{2})} = \boldsymbol{A}^{(1)}\bar{\boldsymbol{A}}^{(\mathbf{1})} \tag{3.17}$$

which still carries the column of zeros property of the first-order matrix.

To apply the zero-moment boundary condition (i.e., $w_1^{(2)} = w_N^{(2)} = 0$) the fourth-order derivative matrix can be directly written from a second-order derivative values as

$$\boldsymbol{w}^{(\mathbf{4})} = \widetilde{\boldsymbol{A}}^{(\mathbf{2})}\boldsymbol{w}^{(\mathbf{2})} = \widetilde{\boldsymbol{A}}^{(\mathbf{2})}\bar{\boldsymbol{A}}^{(\mathbf{2})}\boldsymbol{w} = \bar{\boldsymbol{A}}^{(\mathbf{2})}\bar{\boldsymbol{A}}^{(\mathbf{2})}\boldsymbol{w} \tag{3.18}$$

where $\widetilde{\boldsymbol{A}}^{(\mathbf{2})}$ turns out to be same as $\bar{\boldsymbol{A}}^{(\mathbf{2})}$ for this case of boundary conditions.

Notice that although it is very hard to write more general boundary conditions and changes should be made on a problem basis, this method does not require δ-point technique which should increase stability and convergence.

Method 3: Elimination (Directly coupling the boundary conditions)

The earlier two methods might be easy to implement and effective for simple boundary conditions, but they both have drawbacks when being applied to a more general boundary condition problem. However, these rather simple boundary condition problems may be solved more efficiently using continuous methods such as Galerkin or Rayleigh-Ritz method [31]. To be able to apply more general boundary conditions, boundary conditions can be written using weighting coefficient matrices where each row is the boundary equation. For example, for a simply supported end condition, each equation can be written as

$$\boldsymbol{B}\boldsymbol{w} = \begin{bmatrix} \boldsymbol{B}_{bb} & \boldsymbol{B}_{bd} \end{bmatrix} \begin{Bmatrix} \boldsymbol{w}_b \\ \boldsymbol{w}_d \end{Bmatrix} = \begin{Bmatrix} 0 \\ 0 \end{Bmatrix} \tag{3.19}$$

where the boundary condition sub matrices $\boldsymbol{B_{bb}}$ and $\boldsymbol{B_{bd}}$ are as same as in equation (3.15).

Expanding the sub-matrix multiplication for a more general case as given in equation (3.10)

$$\begin{bmatrix} \boldsymbol{B_{bb}} & \boldsymbol{B_{bd}} \end{bmatrix} \begin{Bmatrix} \boldsymbol{w_b} \\ \boldsymbol{w_d} \end{Bmatrix} = \boldsymbol{B_{bb}}_{M \times M} \boldsymbol{w_b}_{M \times 1} + \boldsymbol{B_{bd}}_{M \times (N-M)} \boldsymbol{w_d}_{(N-M) \times 1} = \boldsymbol{g} \tag{3.20}$$

Here sizes of each dimension are given for easier following. Boundary points can be written in terms of domain points by solving the equation (3.20) for boundary point vector

$$\boldsymbol{w_b} = -\boldsymbol{B_{bb}}^{-1} \boldsymbol{B_{bd}} \boldsymbol{w_d} + \boldsymbol{B_{bb}}^{-1} \boldsymbol{g} \tag{3.21}$$

The generic equation of motion can also be written as given below where $\boldsymbol{A}$ represents a general stiffness matrix while$\boldsymbol{D}$ represents a general inertia matrix:

$$\begin{bmatrix} \boldsymbol{A_{bb}} & \boldsymbol{A_{bd}} \\ \boldsymbol{A_{db}} & \boldsymbol{A_{dd}} \end{bmatrix} \begin{Bmatrix} \boldsymbol{w_b} \\ \boldsymbol{w_d} \end{Bmatrix} + \begin{bmatrix} \boldsymbol{D_{bb}} & \boldsymbol{D_{bd}} \\ \boldsymbol{D_{db}} & \boldsymbol{D_{dd}} \end{bmatrix} \begin{Bmatrix} \boldsymbol{\ddot{w}_b} \\ \boldsymbol{\ddot{w}_d} \end{Bmatrix} = \begin{Bmatrix} \boldsymbol{q_b} \\ \boldsymbol{q_d} \end{Bmatrix} \tag{3.22}$$

Substituting equation (3.21) into equation (3.22) and expanding it according to the sub-matrix multiplication,

$$\begin{aligned} &\begin{bmatrix} -\boldsymbol{A_{bb}} \boldsymbol{B_{bb}^{-1}} \boldsymbol{B_{bd}} + \boldsymbol{A_{bd}} \\ -\boldsymbol{A_{db}} \boldsymbol{B_{bb}^{-1}} \boldsymbol{B_{bd}} + \boldsymbol{A_{dd}} \end{bmatrix} \boldsymbol{w_d} + \begin{bmatrix} -\boldsymbol{D_{bb}} \boldsymbol{B_{bb}^{-1}} \boldsymbol{B_{bd}} + \boldsymbol{D_{bd}} \\ -\boldsymbol{D_{db}} \boldsymbol{B_{bb}^{-1}} \boldsymbol{B_{bd}} + \boldsymbol{D_{dd}} \end{bmatrix} \boldsymbol{w_d} = \\ &\begin{Bmatrix} \boldsymbol{q_b} \\ \boldsymbol{q_d} \end{Bmatrix} - \begin{Bmatrix} \boldsymbol{A_{bb}} \boldsymbol{B_{bb}^{-1}} \boldsymbol{g} + \boldsymbol{D_{bb}} \boldsymbol{B_{bb}^{-1}} \boldsymbol{\ddot{g}} \\ \boldsymbol{A_{db}} \boldsymbol{B_{bb}^{-1}} \boldsymbol{g} + \boldsymbol{D_{db}} \boldsymbol{B_{bb}^{-1}} \boldsymbol{\ddot{g}} \end{Bmatrix} \end{aligned} \tag{3.23}$$

noticing that this form of stiffness and inertia matrices are not square matrices but of matrix size $N \times (N - M)$, the upper portion corresponding to boundary nodes' equation of motion is ignored as is done in [25] and system matrices of size $(N - M) \times (N - M)$ are obtained as:

$$\boldsymbol{K} = \left[-\boldsymbol{A_{db}} \boldsymbol{B_{bb}^{-1}} \boldsymbol{B_{bd}} + \boldsymbol{A_{dd}}\right], \qquad \boldsymbol{M} = \left[-\boldsymbol{D_{db}} \boldsymbol{B_{bb}^{-1}} \boldsymbol{B_{bd}} + \boldsymbol{D_{dd}}\right] \tag{3.24}$$

Even though this method still suffers from δ-point techniques' drawbacks, easy implementation and flexibility to apply general boundary conditions make this method much more popular than the earlier two methods. To the knowledge of the author, this method is not applied while retaining the upper part of equation (3.23), which results in the boundary nodes not obeying the equation of motion but only boundary conditions. This unnoticed shortcoming of the GDQM for nearly three decades is addressed in the following section and will be further improved.

3.2 Galerkin Transformed Differential Quadrature Method

In this section how coordinate transformation works and how the Galerkin method can be implemented in the currently used GDQM formulation is shown.

3.2.1 Implementation of Boundary Conditions

If the elimination process is thought as a coordinate transformation, the equation (3.21) could be rewritten in the matrix form as

$$\boldsymbol{w} = \begin{Bmatrix} \boldsymbol{w_b} \\ \boldsymbol{w_d} \end{Bmatrix} = \begin{Bmatrix} -\boldsymbol{B_{bb}^{-1}} \boldsymbol{B_{bd}} \\ \boldsymbol{I} \end{Bmatrix} \boldsymbol{w_d} + \begin{Bmatrix} \boldsymbol{B_{bb}^{-1}} \boldsymbol{g} \\ 0 \end{Bmatrix} = \boldsymbol{T} \boldsymbol{w_d} + \boldsymbol{g_T} \tag{3.25}$$

Then substituting the transformation matrix $\boldsymbol{T}$ into equation (3.22) without sub-matrix expansion as

$$\boldsymbol{A} \boldsymbol{T} \boldsymbol{w_d} + \boldsymbol{D} \boldsymbol{T} \ddot{\boldsymbol{w}}_{\boldsymbol{d}} = \boldsymbol{q} - \boldsymbol{A} \boldsymbol{g_T} - \boldsymbol{D} \ddot{\boldsymbol{g_T}} \tag{3.26}$$

this is equivalent to the equation (3.23) but if the equation is pre-multiplied with $\boldsymbol{T}^T$, equations reduce to a square matrix with size $(N - M) \times (N - M)$. Hence, the final form of equations can be obtained as

$$\boldsymbol{K} \boldsymbol{w_d} + \boldsymbol{M} \ddot{\boldsymbol{w}}_{\boldsymbol{d}} = \boldsymbol{f} + \bar{\boldsymbol{g_T}} + \bar{\ddot{\boldsymbol{g_T}}} \tag{3.27}$$

where $\boldsymbol{K}$, $\boldsymbol{M}$, $\boldsymbol{F}$, $\bar{\boldsymbol{g_T}}$ and $\bar{\ddot{\boldsymbol{g_T}}}$ are the stiffness matrix, inertia matrix, forcing vector, static boundary effect vector and dynamic boundary effect vector for the differential equation that also satisfies the boundary conditions, respectively. Each matrix can be written in sub-matrix expanded form for completeness as

$$
\begin{aligned}
\boldsymbol{K} = \boldsymbol{T}^T \boldsymbol{A} \boldsymbol{T} \quad &= \textcolor{red}{\boldsymbol{B}_{\boldsymbol{bd}}^T (\boldsymbol{B}_{\boldsymbol{bb}}^{-1})^T \boldsymbol{A}_{\boldsymbol{bb}} \boldsymbol{B}_{\boldsymbol{bb}}^{-1} \boldsymbol{B}_{\boldsymbol{bd}} - \boldsymbol{B}_{\boldsymbol{bd}}^T (\boldsymbol{B}_{\boldsymbol{bb}}^{-1})^T \boldsymbol{A}_{\boldsymbol{bd}}} \\
&\quad - \boldsymbol{A}_{\boldsymbol{db}} \boldsymbol{B}_{\boldsymbol{bb}}^{-1} \boldsymbol{B}_{\boldsymbol{bd}} + \boldsymbol{A}_{\boldsymbol{dd}} \\
\boldsymbol{M} = \boldsymbol{T}^T \boldsymbol{D} \boldsymbol{T} \quad &= \textcolor{red}{\boldsymbol{B}_{\boldsymbol{bd}}^T (\boldsymbol{B}_{\boldsymbol{bb}}^{-1})^T \boldsymbol{D}_{\boldsymbol{bb}} \boldsymbol{B}_{\boldsymbol{bb}}^{-1} \boldsymbol{B}_{\boldsymbol{bd}} - \boldsymbol{B}_{\boldsymbol{bd}}^T (\boldsymbol{B}_{\boldsymbol{bb}}^{-1})^T \boldsymbol{D}_{\boldsymbol{bd}}} \\
&\quad - \boldsymbol{D}_{\boldsymbol{db}} \boldsymbol{B}_{\boldsymbol{bb}}^{-1} \boldsymbol{B}_{\boldsymbol{bd}} + \boldsymbol{D}_{\boldsymbol{dd}} \qquad (3.28) \\
\boldsymbol{f} = \boldsymbol{T}^T \boldsymbol{q} \quad &= \textcolor{red}{-\boldsymbol{B}_{\boldsymbol{bd}}^T (\boldsymbol{B}_{\boldsymbol{bb}}^{-1})^T \boldsymbol{q}_{\boldsymbol{b}}} + \boldsymbol{q}_{\boldsymbol{d}} \\
\bar{\boldsymbol{g}}_{\boldsymbol{T}} = -\boldsymbol{T}^T \boldsymbol{A} \boldsymbol{g}_{\boldsymbol{T}} &= \textcolor{red}{\boldsymbol{B}_{\boldsymbol{bd}}^T (\boldsymbol{B}_{\boldsymbol{bb}}^{-1})^T \boldsymbol{A}_{\boldsymbol{bb}} \boldsymbol{B}_{\boldsymbol{bb}}^{-1} \boldsymbol{g}} - \boldsymbol{A}_{\boldsymbol{db}} \boldsymbol{B}_{\boldsymbol{bb}}^{-1} \boldsymbol{g} \\
\ddot{\bar{\boldsymbol{g}}}_{\boldsymbol{T}} = -\boldsymbol{T}^T \boldsymbol{D} \boldsymbol{g}_{\boldsymbol{T}} &= \textcolor{red}{\boldsymbol{B}_{\boldsymbol{bd}}^T (\boldsymbol{B}_{\boldsymbol{bb}}^{-1})^T \boldsymbol{D}_{\boldsymbol{bb}} \boldsymbol{B}_{\boldsymbol{bb}}^{-1} \ddot{\boldsymbol{g}}} - \boldsymbol{D}_{\boldsymbol{db}} \boldsymbol{B}_{\boldsymbol{bb}}^{-1} \ddot{\boldsymbol{g}}
\end{aligned}
$$

Red terms are correction terms that incorporate the boundary points into the equation of motion and solve the differential equations without truncation. Note that these correction terms are mostly very large in numerical greatness if checked element by element, yet they affect all the matrices nearly at the same scale so that change in the solution is not obvious.

As far as the author can conclude by examining the 30 years old literature, the main oversight happens while trying to apply a static condensation type of transformation while the boundary condition matrix is not a part of the initial stiffness matrix. Considering boundary matrix equations as the part of the initial stiffness matrix (i.e., $\boldsymbol{B}_{\boldsymbol{bb}} = \boldsymbol{A}_{\boldsymbol{bb}}$, $\boldsymbol{B}_{\boldsymbol{bd}} = \boldsymbol{A}_{\boldsymbol{bd}}$), it can be seen that red terms in equation (3.28) cancel each other.

By using this method to implement boundary conditions, the equation of motion can be solved for all points while also solving boundary conditions in boundary points. However, this does not provide any advantage compared with the elimination method explicitly. The main advantage comes from not needing to use δ-point technique which increases stability and convergence as it will be shown in the verification section. Since the elimination method does not solve the equation of motion for the points that are denoted as boundaries, extra boundary points need to be very close to the boundaries. This is needed because when they are ignored while solving the equation of motion, and loss of information is low since their function values are very similar to the actual boundaries. However, if they were taken to be normally separated points, they are different in function value, and the equation of motion needs to be solved for those extra boundary points. On the other hand, in the transformation method, the boundary nodes are expressed in terms of domain nodes, but the boundary does not need to be very close to the boundary but any point that does not make $\boldsymbol{B_{bb}}$ sub-matrix singular since what has been done is a coordinate transformation using the extra information of boundary equations. Even though, this point of changing the boundary points to any domain node does not change the results significantly, to stick to historical conventions and to have higher stability boundary nodes are chosen as the closest nodes to the actual boundaries.

3.2.2 Imposing Symmetry to the System Matrices

Weighted residual methods are a class of numerical solution methods that are used to solve eigenvalue problems [31, 128]. In general terms, the eigenfunction is approximated by a trial function that satisfies the boundary conditions and then a residual is defined which should be equal to zero if the approximation is exact as,

$$A[W] = \lambda D[W], \;\; W\left(x\right) \cong \bar{\phi}\left(x\right), \;\; \rightarrow \quad R\left(\bar{\phi}, x\right) = A[\bar{\phi}] - \lambda D[\bar{\phi}] \cong 0 \tag{3.29}$$

where $A[\;]$ and $D[\;]$ are linear operators that may include differentiation or integration, λ and $W\left(x\right)$ are eigenvalue and eigenvector, respectively. To obtain the residual, $R\left(\bar{\phi}, x\right)$, eigenfunction $W\left(x\right)$ is replaced with an approximating function $\bar{\phi}\left(x\right)$. The approximating function $\bar{\phi}\left(x\right)$ is chosen so that the residual is close to zero as possible.

A condition that the residual is nearly zero on every point in the domain is achieved by multiplying the residual with a weighting function $g(x)$ and integrating it over the domain and equating it to zero as,

$$\int g(x) R\left(\bar{\phi}, x\right) dx = 0 \tag{3.30}$$

The definition of the weighting function and method of obtaining the approximation changes the name of the method under the family of methods called weighted residual methods. Both Galerkin and Collocation method uses trial function expansion while calculating the approximation function as

$$W\left(x\right) \cong \bar{\phi}\left(x\right) = \sum_{i=1}^{n} c_i \phi_i(x) \tag{3.31}$$

where c_i is the weighting coefficient, n is the number of terms that will be used in the expansion, and $\phi_i(x)$ is the trial function that satisfies some or all boundary conditions depending on the application. Galerkin and collocation methods differ from each other while defining the weighting function. Collocation method uses a Dirac delta ($\delta(x)$) weighting function that is sampled at n points in the domain as,

$$\begin{aligned} &\int \delta\left(x-x_i\right) R\left(\bar{\phi}, x\right) dx = R\left(\bar{\phi}\left(x_i\right), x_i\right) \\ &= A\left[\sum_{j=1}^{n} c_j \phi_j\left(x_i\right)\right] - \lambda D\left[\sum_{j=1}^{n} c_j \phi_j\left(x_i\right)\right] = 0, \;\; i = 1, 2, \ldots, n \end{aligned} \tag{3.32}$$

With this definition of the weighting function, the procedure of calculating the integral is avoided and the residual is equated to zero at grid points, which in turn makes the solution exact at grid points and may have error between those grid points.

Galerkin method uses the trial functions themselves as weighting function which necessitates the calculation of the integral as

$$\begin{aligned} &\int \phi_i R\left(\bar{\phi}, x\right) dx = \\ &\sum_{j=1}^{n} c_j \int A\left[\phi_i\left(x\right)\right] \phi_j\left(x\right) dx - \lambda \sum_{j=1}^{n} c_j \int D\left[\phi_i\left(x\right)\right] \phi_j\left(x\right) dx = 0, \\ &i = 1, 2, \ldots, n \end{aligned} \tag{3.33}$$

With this definition of the weighting function, if trial functions are chosen to be orthogonal then the resulting system matrices will be symmetric. Both methods transform the continuous eigenvalue problem with eigenvectors $W\left(x\right)$ into a discrete eigenvalue problem with weighting coefficients c_j replacing the eigenvectors as

$$\left(k_{ij} - \lambda m_{ij}\right) c_j = 0, \;\; i, j = 1, 2, 3, \ldots, n, \tag{3.34}$$

where k_{ij} and m_{ij} are elements of stiffness and mass matrix, respectively, and can be defined as

$$\begin{aligned} K_{collocation} &: k_{ij} = A\left[\phi_j\left(x_i\right)\right], & K_{Galerkin} &: k_{ij} = \int A\left[\phi_i\left(x\right)\right] \phi_j\left(x\right) dx \\ M_{collocation} &: m_{ij} = D\left[\phi_j\left(x_i\right)\right], & M_{Galerkin} &: m_{ij} = \int D\left[\phi_i\left(x\right)\right] \phi_j\left(x\right) dx \end{aligned} \tag{3.35}$$

If $A[\;\;]$ and $D[\;\;]$ were to be considered as operators that are formed with matrices for the collocation method, then GDQM formulation can be retrieved. In that regard, GDQM can be thought of as a special case of the collocation method where the trial function is Lagrange interpolating polynomial and boundary conditions are satisfied while solving the eigenvalue problem.

Due to this analogy, GDQM suffers from similar drawbacks to the collocation method where matrices are not symmetric and prone to ill-conditioning. On the other hand, the Galerkin method does not suffer from these problems if orthogonal trial functions are used. For that matter, Lagrange interpolating polynomials are orthogonal and can take derivatives or integrals as simple as matrix/vector multiplication such that both drawbacks, which are the calculation of the integral and determining an orthogonal trial function that also satisfies boundary conditions, of the Galerkin method can also be handled by GDQM if it can be formulated.

Integral of Products in GDQM

Following the procedure explained by Yagci et. al. [129] due to the similarity of the goal, starting by approximating a definite integral over a domain as a matrix-vector multiplication as,

$$\int_{x_a}^{x_b} f(x)dx = \sum_{k=1}^{N} c_k f\left(x_k\right) \tag{3.36}$$

From the Ph.D. dissertation of Shu [12] integration coefficient can directly be defined,

$$c_k^{ab} = w_{ak}^I - w_{bk}^I, \tag{3.37}$$

where a and b refer to discretized grid points that coincide with the integral boundaries x_a and x_b, moreover, w_{ak}^I are the elements of a matrix that is defined as the inverse of specially defined derivation matrix $\widetilde{A}$. Elements of this matrix $\widetilde{A}$ are defined as,

$$\widetilde{A}_{ij} = \frac{x_i + \delta}{x_j + \delta} A_{ij}^{(1)} \; for \; i \neq j \quad and \; \widetilde{A}_{ii} = A_{ii}^{(1)} + \frac{1}{x_i + \delta} \tag{3.38}$$

here $A_{ij}^{(1)}$ are the elements of the first-order derivation matrix as defined in equation (3.3) and δ is a small shifting constant that ensures any grid point will be sufficiently away from zero as it would cause a singularity ($\sim \delta = 10^{-3}$ are observed to be satisfactory).

Now that the formal definition of an integrating vector is done, a way of integrating two multiplied functions is needed. Assume $h(x)$ and $g(x)$ are smooth and continuous functions over the domain $[x_a, x_b]$ and can be constructed with a polynomial of degree at most N. Then, function $f(x)$ that is obtained by multiplying $h(x)$ and $g(x)$ should be smooth, continuous, and can be constructed with a polynomial of degree at most $2N$.

To be able to accommodate the degree of a polynomial of the function $f(x)$, $2N$ sampling points are necessary, such that Lagrange interpolating polynomial can be a polynomial of the degree $2N$. A matrix that changes the grid points used can easily be defined as,

$$\mathcal{T}_{ij} = \prod_{k=1,k\neq j}^{N} \frac{x_i' - x_k}{x_j - x_k}, \tag{3.39}$$

where $\mathcal{T}_{ij}$ are the elements of the coordinate up-scaling matrix $\mathcal{T}$ that when it pre-multiplies a vector of values, it changes the values obtained at grid points x_j into values that correspond to new grid points x_i'. Technically any type of grid points can be used to up-scale the number of grind points and they should produce the same results for low N, however after a certain number of grid points uniform grid points cause problems and Gauss-Lobatto-Chebyshev sampling should be preferred while up-scaling.

Writing $g(x)$ and $h(x)$ in the up-scaled discretized domain as,

$$\boldsymbol{g}'_{2N\times 1} = \mathcal{T}_{2N\times N}\boldsymbol{g}_{N\times 1}, \qquad \boldsymbol{h}'_{2N\times 1} = \mathcal{T}_{2N\times N}\boldsymbol{h}_{N\times 1} \tag{3.40}$$

so that Integral can be written as

$$\int_{x_a}^{x_b} g\left(x\right) h\left(x\right) dx = \sum_{k}^{2N} c_k^{ab} g\left(x_k\right) h\left(x_k\right) = \boldsymbol{c}^T \left(\boldsymbol{g}' \odot \boldsymbol{h}'\right), \tag{3.41}$$

where $\odot$ is the element-wise (Hadamard) product of two vectors. For convenience that will be clear later, the matrix-Hadamard multiplication [130] can be rearranged as

$$\boldsymbol{c}^T \left(\boldsymbol{g}' \odot \boldsymbol{h}'\right) = \left(\boldsymbol{g}'\right)^T \left(\boldsymbol{c} \odot \boldsymbol{h}'\right) = \left(\boldsymbol{g}'\right)^T \boldsymbol{D_c} \boldsymbol{h}' \tag{3.42}$$

where $\boldsymbol{D_c}$ is the diagonal matrix where diagonal entries are formed by entries of $\boldsymbol{c}$ vector. Next, the up-scaling of grid points is incorporated into the integral matrix itself as

$$\int_{x_a}^{x_b} g\left(x\right) h\left(x\right) dx = \left(\boldsymbol{g}'\right)^T \boldsymbol{D_c} \boldsymbol{h}' = \left(\boldsymbol{g}'\right)^T \mathcal{T}^T \boldsymbol{D_c} \mathcal{T} \boldsymbol{h}' = \boldsymbol{g}^T \boldsymbol{P} \boldsymbol{h} \tag{3.43}$$

where, $\boldsymbol{P} = \mathcal{T}^T \boldsymbol{D_c} \mathcal{T}$ is the integral of products matrix between two vectors.

Galerkin Formulation

All the tools needed are derived up to now; the next step is to formulate a classical eigenvalue problem in terms of the Galerkin method. Writing the residual equation (3.33) using derivative weighting coefficient matrices

$$\int w_i R\left(w_j, x\right) dx = \int \sum_{j=1}^{n} A_{jk} w_k\left(x\right) w_i\left(x\right) dx - \lambda \int \sum_{j=1}^{n} D_{jk} w_k\left(x\right) w_i\left(x\right) dx = 0 \tag{3.44}$$

Here A_{jk} and D_{jk} are the elements of operator matrices that are obtained by writing them using derivative weighting coefficients. Thus, system matrices obtained using Galerkin weighted residual method can be written as

$$\begin{aligned} k'_{ij} &= \int_{x_a}^{x_b} \sum_{j=1}^{n} A_{jk} w_k\left(x\right) w_i\left(x\right) dx = \boldsymbol{w}^T \boldsymbol{P}\left(\boldsymbol{A}\boldsymbol{w}\right) = \boldsymbol{w}_{\boldsymbol{d}}^T \boldsymbol{T}^T \boldsymbol{P}\boldsymbol{A}\boldsymbol{T}\boldsymbol{w}_{\boldsymbol{d}} \\ m'_{ij} &= \int_{x_a}^{x_b} \sum_{j=1}^{n} D_{jk} w_k\left(x\right) w_i\left(x\right) dx = \boldsymbol{w}^T \boldsymbol{P}\left(\boldsymbol{D}\boldsymbol{w}\right) = \boldsymbol{w}_{\boldsymbol{d}}^T \boldsymbol{T}^T \boldsymbol{P}\boldsymbol{D}\boldsymbol{T}\boldsymbol{w}_{\boldsymbol{d}} \end{aligned} \tag{3.45}$$

Here, notice that the function values at grid points are not available, and these system matrices cannot be written before solving the problem. Thus, the residual equation can be reformulated and written in the parentheses of $\boldsymbol{w}_{\boldsymbol{d}}^T$ as,

$$\boldsymbol{w}_{\boldsymbol{d}}^T\left(\boldsymbol{T}^T \boldsymbol{P}\boldsymbol{A}\boldsymbol{T}\boldsymbol{w}_{\boldsymbol{d}}\right) - \boldsymbol{w}_{\boldsymbol{d}}^T\left(\boldsymbol{T}^T \boldsymbol{P}\boldsymbol{D}\boldsymbol{T}\boldsymbol{w}_{\boldsymbol{d}}\right) = 0 \tag{3.46}$$

Assuming $\boldsymbol{w}_{\boldsymbol{d}} \neq 0$ for a non-trivial solution, the inside of the parenthesis needs to be solved and respective system matrices can be written as the matrices that pre-multiplies the eigenvectors

$$\boldsymbol{K} = \boldsymbol{T}^T \boldsymbol{P}\boldsymbol{A}\boldsymbol{T}, \qquad \boldsymbol{M} = \boldsymbol{T}^T \boldsymbol{P}\boldsymbol{D}\boldsymbol{T} \tag{3.47}$$

Similarly, without a loss of generality, if the equation (3.26) is pre-multiplied with $\boldsymbol{T}^T \boldsymbol{P}$, the equation of motion for the time domain can be obtained as,

$$\boldsymbol{T}^T \boldsymbol{P}\boldsymbol{A}\boldsymbol{T}\boldsymbol{w}_{\boldsymbol{d}} + \boldsymbol{T}^T \boldsymbol{P}\boldsymbol{D}\boldsymbol{T}\ddot{\boldsymbol{w}}_{\boldsymbol{d}} = \boldsymbol{T}^T \boldsymbol{P}\boldsymbol{q} - \boldsymbol{T}^T \boldsymbol{P}\boldsymbol{A}\boldsymbol{g}_{\boldsymbol{T}} - \boldsymbol{T}^T \boldsymbol{P}\boldsymbol{D}\ddot{\boldsymbol{g}}_{\boldsymbol{T}} \tag{3.48}$$

which can be obtained from defining a residual to a solution of the time domain equation if more rigor of derivation is needed. Re-defining the final system matrices for completeness as,

$$\begin{gathered}\boldsymbol{K}\boldsymbol{w_d}+\boldsymbol{M}\ddot{\boldsymbol{w}}_{\boldsymbol{d}}=\boldsymbol{f}+\bar{\boldsymbol{g}}_{\boldsymbol{T}}+\ddot{\bar{\boldsymbol{g}}}_{\boldsymbol{T}}\\ \text{where}\qquad \boldsymbol{K}=\boldsymbol{T}^T\boldsymbol{PAT}\qquad \boldsymbol{M}=\boldsymbol{T}^T\boldsymbol{PDT}\\ \boldsymbol{f}=\boldsymbol{T}^T\boldsymbol{Pq}\qquad \bar{\boldsymbol{g}}_{\boldsymbol{T}}=-\boldsymbol{T}^T\boldsymbol{PA}\boldsymbol{g_T}\qquad \ddot{\bar{\boldsymbol{g}}}_{\boldsymbol{T}}=-\boldsymbol{T}^T\boldsymbol{PD}\ddot{\boldsymbol{g}}_{\boldsymbol{T}}\end{gathered}\tag{3.49}$$

Symmetry of System Matrices

For any self-adjoint operator $A[\ ]$, and two arbitrary functions that satisfy the boundary conditions in the domain $[x_a, x_b]$, $g(x)$ and $h(x)$; the condition of symmetry can be written, that is by definition satisfied for self-adjoint operators, as

$$\int_{x_a}^{x_b} g\left(x\right) A[h\left(x\right)]dx = \int_{x_a}^{x_b} h\left(x\right) A[g\left(x\right)]dx \tag{3.50}$$

Assuming functions $g(x)$ and $h(x)$ can be expanded exactly using $(N-1)^{th}$ order polynomial, equation (3.50) can be written using the GDQM discretization methods similar to the equation (3.44),

$$\boldsymbol{g}_{\boldsymbol{d}}^T\boldsymbol{T}^T\boldsymbol{PAT}\boldsymbol{h_d}=\boldsymbol{h}_{\boldsymbol{d}}^T\boldsymbol{T}^T\boldsymbol{PAT}\boldsymbol{g_d}\quad\rightarrow\quad \boldsymbol{g}_{\boldsymbol{d}}^T\boldsymbol{K}\boldsymbol{h_d}=\boldsymbol{h}_{\boldsymbol{d}}^T\boldsymbol{K}\boldsymbol{g_d} \tag{3.51}$$

where $\boldsymbol{g_d}$ and $\boldsymbol{h_d}$ are function values at the domain points. Since both sides of the equality are actually matrix with 1×1 dimensions (i.e., scalar), the transpose of one side without changing the equality can be taken as,

$$\boldsymbol{g}_{\boldsymbol{d}}^T\boldsymbol{K}\boldsymbol{h_d}=\boldsymbol{g}_{\boldsymbol{d}}^T\boldsymbol{K}\boldsymbol{h_d} \tag{3.52}$$

which would only hold true if and only if $\boldsymbol{K}^T = \boldsymbol{K}$. Since an explicit formula for the operator is not defined, this symmetry proof can be used for any problem that can be encountered as long as the functions and the operated functions can be exactly expressed with $(N-1)^{th}$ order polynomial.

Hence, by applying a coordinate transformation to incorporate boundary conditions followed by a Galerkin weighted residual technique to the already existing GDQM formulation, a superior method without any drawbacks are obtained which is named as Galerkin transformed Differential Quadrature Method (GtDQM).

3.3 Nonlinear Numerical Methods

Most of the structural problems can be modeled with linear differential equations using different assumptions or linearizations. However, in real life, models are only applicable to a certain degree, and generally, nonlinear corrections are necessary to increase the limits of the model. Hence a need for different nonlinear techniques has evolved, one that will be described in this section utilizes periodic solutions to obtain nonlinear algebraic equations from nonlinear differential equations. These equations can be solved with numerical solution methods such as Newton's method and solution paths can be followed by the likes of pseudo arc-length continuation.

3.3.1 Harmonic Balance Method

The harmonic balance method uses the assumption of harmonic response, generally with an included phase which is needed if nonlinearity creates damping-type effects. Even though this phase difference can be shown with complex numbers or phase angles, it is more likely to assume a separate sine and cosine with different coefficients as,

$$x(t) = x_s \sin\theta + x_c \cos\theta \tag{3.53}$$

where x_s and x_s are sine and cosine coefficients of harmonic expansion and θ is the angle between 0 and 2π for a representative period and also defined as $\theta = \omega t$ where ω is the vibration frequency.

When this form of assumed response is substituted into the differential equation of motion, the algebraic equation of motion can be obtained by balancing the sine and cosine coefficients to the one coming from the forcing. This procedure doubles the size of the equation of motion since each coefficient of sine or cosine needs to be balanced separately. If the complex response was assumed, similarly, the solution would need to double the size of the original equation of motion since there are two real components to each complex coefficient.

This procedure may also be assumed as finding the Fourier coefficients of the nonlinear force corresponding to the assumed harmonic motion. Even though an expansion may lead to coefficients of integer multiples of the original frequency ($n\theta$) they cannot be balanced since our original harmonic expansion only has a single frequency in it. To accommodate this fact multiple harmonics may be used in the assumption of the response which can generally be written as,

$$x(t) = x_0 + \sum_{n=1}^{N} x_{s_n} \sin n\theta + x_{c_n} \cos n\theta \tag{3.54}$$

where x_0 is the bias term and may be important in nonlinearities that do not produce a symmetric forcing compared to the motion. Note that this expansion can exactly express the possible response and the respective nonlinear forcing in the frequency domain, it needs an infinite number of components which is not feasible and is generally cut off when the necessary accuracy is reached.

At the multiple harmonic level, it is easier to define Fourier integrals for coefficient determination since the trigonometric manipulations needed gets much trickier. Moreover, with integral definitions higher harmonic contributions coming from expansion are not calculated. Integral for each term can be defined as,

$$\begin{aligned} f_0^{nl} &= \frac{1}{2\pi} \int_0^{2\pi} f_{nl}(x) d\theta \\ f_{s_n}^{nl} &= \frac{1}{\pi} \int_0^{2\pi} f_{nl}(x) \sin(n\theta) d\theta \\ f_{c_n}^{nl} &= \frac{1}{\pi} \int_0^{2\pi} f_{nl}(x) \cos(n\theta) d\theta \end{aligned} \tag{3.55}$$

where $f_{nl}(x)$ is the nonlinear forcing, f_0^{nl} is the bias coefficient, $f_{s_n}^{nl}$ and $f_{c_n}^{nl}$ are the sine and cosine coefficients of n^{th} harmonic. The resulting nonlinear forcing vector may also sometimes be defined as a response-dependent nonlinearity matrix.

Equivalently describing function method [131] can also be used especially if the goal is to obtain a nonlinearity matrix. Yet, in this work, the harmonic balance method is preferred.

3.3.2 Pseudo Arc-length Continuation with Newton's Method

While solving nonlinear algebraic equations an iterative procedure is needed if an analytical solution method is not applicable, since the nonlinear effect may depend on the response amplitude. One such method is Newton's method which is relatively simple to apply and has a relatively high convergence rate [132]. The main premise of Newton's method is to linearly approximate the zero point for a residual function using the 'slope' of the current solution point to predict the next solution point, which may be illustrated by the figure 3.1.

For a one-dimensional case, the next iteration for the root may mathematically be calculated from the earlier prediction as,

$$x_{i+1} = x_i - \frac{f(x_i)}{f'(x_i)} \tag{3.56}$$

where the prime denotes the first derivative of the residual concerning the variable in question and i is the current iteration step. To change the method to a higher dimensional case is to change the division by a derivative to an inverse multiplication by a Jacobian ($\boldsymbol{J}$). Where the Jacobian is the matrix formed by the partial derivatives of a function that outputs a vector of values. Mathematically Newton's next iteration step and definition of Jacobian can be written as,

$$\boldsymbol{x}^{i+1} = \boldsymbol{x}^{i} - \boldsymbol{J}(\boldsymbol{x}^{i})^{-1}\boldsymbol{R}(\boldsymbol{x}^{i}) \qquad \text{where } J_{jk} = \frac{\partial R_j(x^i)}{\partial x_k^i} \tag{3.57}$$

where superscript denotes the value of the variable at the given iteration step and subscripts j, k denote the elements of the given matrix or vector.

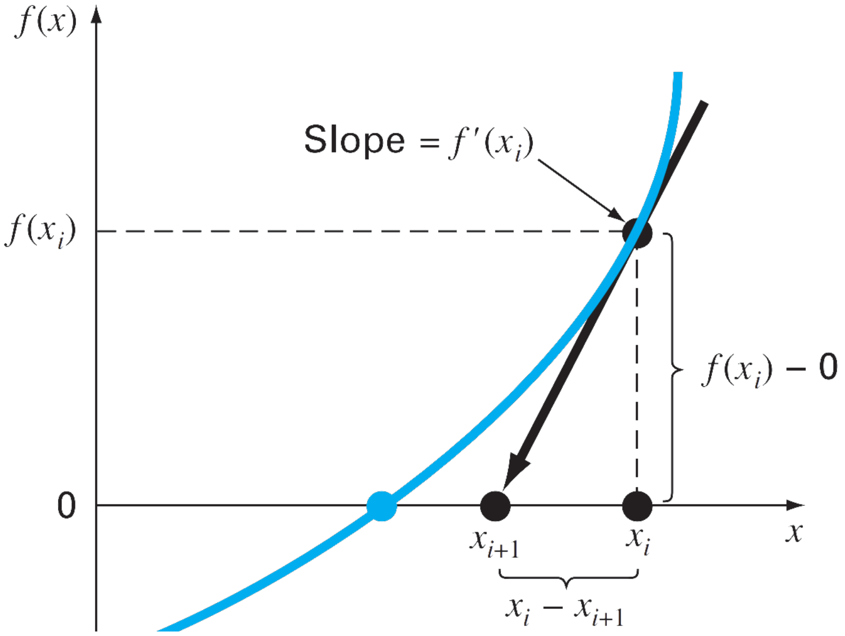

Figure 3.1: Illustration of Newton's method in one dimensions, taken from [132]

This method can be used to find the response of a nonlinear system to harmonic forcing at a single specified frequency, to cover a frequency range of interest (i.e., to obtain a frequency response function (FRF)) excitation frequency may be increased after each solution step and a new solution at the new frequency can be obtained. This is the basics of a Homotopy continuation algorithm, where the parameter that needs to cover a range (such as excitation frequency) is directly followed. With this method unstable solution branches cannot be obtained and instead seen as a discontinuity in the FRF.

To mend such a problem and apply it to other problems pseudo arc-length continuation can be used, which adds another parameter to be followed. This change makes the extra parameter an unknown, increasing the number of unknowns by one, and to match the number of equations to the number of unknowns, the method adds a hyper-sphere equation. The added equation makes the next solution step to be on the intersection of the hyper-sphere surface and the solution curve. This allows the solution of multiple points at a single frequency while also being able to change directions and show unstable branches.

For an example vibration problem that produces a residual of the form $\boldsymbol{R}(\boldsymbol{x}, \omega) = \boldsymbol{K} - \boldsymbol{\omega^2} \boldsymbol{M} + \boldsymbol{f^{NL}} - \boldsymbol{f^{ext}}$ at N discrete coordinate points, initial prediction for the next solution point can be calculated by

$$\boldsymbol{q^{k+1}} = \boldsymbol{q^k} - \boldsymbol{J'}(\boldsymbol{q^k})^{\boldsymbol{-1}} \boldsymbol{R'}(\boldsymbol{q^k}) \quad \text{where} \quad \boldsymbol{q} = \begin{Bmatrix} \boldsymbol{x} \\ \omega \end{Bmatrix} \tag{3.58}$$

where augmented Jacobian $\boldsymbol{J'}(q^k)$ is calculated using the augmented residual $\boldsymbol{R'}(q^k)$ which can be obtained by adding a hyper-sphere (or an ellipse for that matter) of the form,

$$\boldsymbol{R'}(\boldsymbol{q^k}) = \begin{Bmatrix} \boldsymbol{R}(\boldsymbol{x^k}, \omega^k) \\ (\boldsymbol{q^k} - \boldsymbol{q^{k-1}})^T (\boldsymbol{q^k} - \boldsymbol{q^{k-1}}) - \Delta s^2 \end{Bmatrix} \tag{3.59}$$

where s is the total arc length covered so far and $\Delta s = s^k - s^{k-1}$ is the radius of the hyper-sphere defined around the earlier solution point of q^{k-1}. When the prediction for the next iteration step $\boldsymbol{q^{k+1}}$ is found, then this initial prediction can be used in Newton's method of equation (3.57) until a convergence criterion is met. Convergence criteria are generally taken as the maximum of absolute differences between residuals and zero.

This explanation of arc-length continuation is the basics and the method can be made much faster and more robust by slight modifications such as the addition of sophisticated initial guess methods than Jacobian, or determination of step-size to adapt according to the difficulty of solution at a point.

3.3.3 Time Integration

Even though time domain integration is a computationally very expensive tool, it may be necessary to correctly determine the response of the system such that verification can be conducted. The simplest time integration method is the Euler's method where the velocity ($\dot{y}$) of the next time step is found by a state space form using the displacement (y) of the current time step and increasing the next time step displacement value by multiplying the time step and velocity ($y^{new} = y^{old} + \dot{y}^{old}dt$). A more general method is the Runge-Kutta family of methods where the velocity of the next time step is calculated by dividing the interval by several sub-steps and the number of sub-steps determines the order of the method, where 4^{th} order Runge-Kutta is generally preferred, determined by the optimization of lower computation time and the bigger possible step size in time.

Since the main focus is not on the time domain simulations a commercially available ordinary differential equation solver is used such that sophisticated improvements needed are not employed. For that purpose ode45() or ode23s() commands of Matlab [133] is used to obtain time domain response depending on the characteristics. To obtain convergence faster, either linear or closest (amplitude vise) last known nonlinear mode shape is given as deflection shape which also minimizes the effects of other modes while examining the free vibration characteristics.

To extract natural frequency, the most common method is to convert the time domain response to frequency response by the fast Fourier transformation (FFT) method. By looking at the spectral response, additional effects of higher harmonics or other modes can be seen, however, it is another layer of relatively computationally expensive step and to increase the accuracy of the natural frequency estimation, time domain simulations need to increase in length.

Alternatively, the frequency might also be calculated from each half period of each cycle by looking at the velocity response and determining the times at which the velocity becomes zero by linear interpolation. However, the obtained frequencies are generally dominated by higher frequency effects even though they are small in amplitude they are very frequent by definition. This problem can be mended to some degree by smoothing the time domain velocity response with an averaging window that is of appropriate length to eliminate higher frequencies. During the smoothing process, higher frequency components affect the resulting natural frequency estimation as a random error, such that a single frequency can be estimated with an approximate normally distributed error. Moreover, a change in natural frequency can also be obtained if it changes with time.

Details of the method shown here are not cited to a source, since it is not found in the literature even though it must have been used somewhere due to the simplicity of the method. More detail is given in the Appendix A.1.

3.4 Fluid Conveying Beam Theory with Nonlocal Strain Gradient Elasticity

In this section, equations of motion that can be used to examine fluid flow in small-scale tubes will be derived using Hamilton's principle. First, the potential and kinetic energy of the tube will be derived using an equivalent beam with Euler-Bernoulli kinematic assumptions, then fluid-structure interaction will be incorporated into the equation of motion with different corrections. Finally, spatial discretization will be applied, and other solution methods will be shown considering the case at hand.

Figure 3.2 is given to represent the geometry of the model graphically, where r_{in}, r_{out}, t, L, and U are inner radius, outer radius, thickness of the wall, length of the tube and the fluid flow speed.

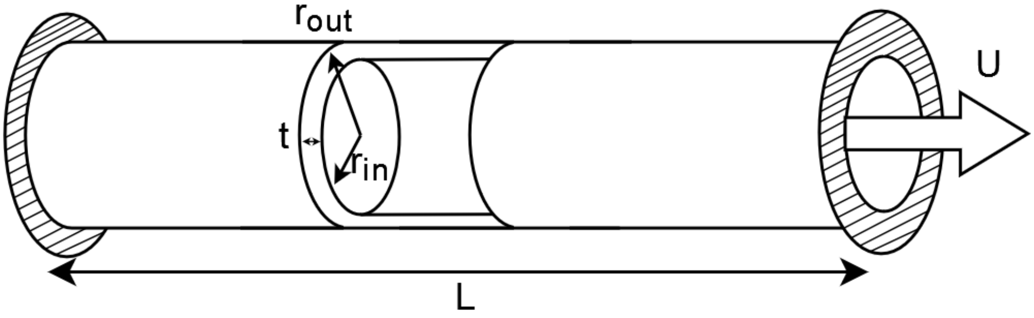

Figure 3.2: Schematic of the clamped-clamped fluid conveying tube with fluid flow

3.4.1 Euler Bernoulli Beam Theory with Large Deflection Nonlinearity

By using Euler-Bernoulli beam kinematic assumptions the displacement fields can be defined as u_1, u_2, u_3 along x, y, z, respectively as the following,

$$\begin{aligned} u_1(x,z,t) &= u(x,t) - z\frac{\partial w}{\partial x} \\ u_2(x,z,t) &= 0 \\ u_3(x,z,t) &= w(x,t) \end{aligned} \tag{3.60}$$

where $\frac{\partial w}{\partial x}$ is the neutral surface rotation, u and w are the displacement of the neutral surface, which corresponds to the middle surface for uniform beams, along the x and z directions, respectively. Following that, Cauchy (infinitesimal) strain tensor, Green-Lagrange (finite) strain tensor, and second-order deformation gradient tensor (η_{ijk}) can be defined as,

$$\begin{aligned} \varepsilon_{ij_{Cauchy}} &= \frac{1}{2}\left(\frac{\partial u_i}{\partial x_j} + \frac{\partial u_j}{\partial x_j}\right) \\ \varepsilon_{ij_{Green-Lagrange}} &= \frac{1}{2}\left(\frac{\partial u_i}{\partial x_j} + \frac{\partial u_j}{\partial x_j} + \frac{\partial u_k}{\partial x_i}\frac{\partial u_k}{\partial x_j}\right) \\ \eta_{ijk} &= \frac{\partial^2 u_k}{\partial x_j \partial x_i} \end{aligned} \tag{3.61}$$

where indices $i, j, k = 1, 2, 3$ defines the corresponding displacement and coordinate for the given direction (i.e., $x_1 = x,\ x_2 = y,\ x_3 = z$), moreover repeated indices imply summation over the range.

From there the work conjugate stresses corresponding to the given strain measures of equation (3.61) can be defined as,

$$\sigma_{ij} = \frac{\partial W}{\partial \varepsilon_{ij}}, \qquad \tau_{ijk} = \frac{\partial W}{\partial \eta_{ijk}}, \tag{3.62}$$

where W is the strain energy density, σ_{ij}, and τ_{ijk} are Cauchy stress tensor, and double stress tensor, respectively.

second-order deformation gradient tensor can be split down into three independent parts that contribute to the strain energy as is done by Lam et al. [32], however, to introduce non-locality to the higher-order theory approach done by Lim et al. [76] will be used for simplification. Hence, only explicitly calculating the first-order strains are necessary.

Substituting displacements of equation (3.60) into Green-Lagrange strain definition given in equation (3.61),

$$\varepsilon_{xx} = \frac{1}{2}\left(\frac{\partial u}{\partial x}\right)^2 + \frac{\partial u}{\partial x} + \frac{z^2}{2}\left(\frac{\partial^2 w}{\partial x^2}\right)^2 - z\frac{\partial^2 w}{\partial x^2} + \frac{1}{2}\left(\frac{\partial w}{\partial x}\right)^2 - z\frac{\partial u}{\partial x}\frac{\partial^2 w}{\partial x^2} \tag{3.63}$$

By applying von-Karman nonlinear assumptions of considering the case for moderate rotations and small strains (i.e., only considering multiplication terms coming from mid-plane rotation $\frac{\partial w}{\partial x}$ and neglecting terms coming from mid-plane stretching $\frac{\partial u}{\partial x}$), simplified strain relation can be obtained,

$$\varepsilon_{xx} = \frac{\partial u}{\partial x} - z\frac{\partial^2 w}{\partial x^2} + \frac{1}{2}\left(\frac{\partial w}{\partial x}\right)^2 \tag{3.64}$$

Only considering the axial normal stress, the strain energy of the beam can be written as,

$$U = \frac{1}{2}\int_V \left(\sigma_{xx}\varepsilon_{xx} + \tau_{xxx}\eta_{xxx}\right) dV = \frac{1}{2}\int_V \left(\sigma_{xx}\varepsilon_{xx} + \sigma_{xx}^{(1)}\frac{\partial \varepsilon_{xx}}{\partial x}\right) dV \tag{3.65}$$

where the second form is given since it is used in the derivation of Lim et al. [76], similarly using the same naming convention, $\sigma_{xx}^{(1)}$ is the higher-order stress and σ_{xx} is the classical stress. Stresses are then defined in the framework of nonlocal elasticity theory by the given constitutive relations,

$$\begin{aligned} \sigma_{xx} &= \int_0^L E\alpha_0(x, x', e_0 a)\varepsilon'_{xx} dx' \\ \sigma_{xx}^{(1)} &= l^2 \int_0^L E\alpha_1(x, x', e_1 a)\frac{\partial \varepsilon'_{xx}}{\partial x} dx' \end{aligned} \tag{3.66}$$

where L is the length of the domain, l is the length scale material parameter, e_0a and e_1a are the nonlocal parameters, and α_0 and α_1 are the nonlocal kernels that account for the distribution of the nonlocal effect for classical and higher-order theories, respectively.

Note that, this formulation method is somewhat in line with nonlocal elasticity theory, however, strain gradient theory is not fully accounted for with this formulation and contains lots of simplifications without any rigorous proof. Even though the presented formulation is not complete, considering this is the only formulation that couples nonlocal and higher-order effects together and the aim of this thesis is not to develop a new theory of elasticity, the formulation is used without modification.

To combine classical and higher-order stresses the variation of the potential energy of equation (3.65) can be modified to obtain higher-order boundary conditions as is done by Mindlin [39], or by Lam et al. [32] as,

$$\begin{aligned}\delta U &= \frac{1}{2}\int_V \left(\sigma_{xx}\delta\varepsilon_{xx} + \sigma_{xx}^{(1)}\frac{\partial\delta\varepsilon_{xx}}{\partial x}\right) dV \\ &= \frac{1}{2}\int_V \left(\sigma_{xx}\delta\varepsilon_{xx} - \frac{\partial\sigma_{xx}^{(1)}}{\partial x}\delta\varepsilon_{xx}\right) dV + \frac{1}{2}\left[\int_A \sigma_{xx}^{(1)}\delta\varepsilon_{xx} dA\right]\Bigg|_0^L \\ &= \frac{1}{2}\int_V \left(t_{xx}\delta\varepsilon_{xx}\right) dV + \frac{1}{2}\left[\int_A \sigma_{xx}^{(1)}\delta\varepsilon_{xx} dA\right]\Bigg|_0^L\end{aligned} \tag{3.67}$$

where the second part will be used to obtain the higher-order boundary conditions, A is the cross-sectional area, and t_{xx} is the total axial stress and is defined as,

$$t_{xx} = \sigma_{xx} - \frac{\partial\sigma_{xx}^{(1)}}{\partial x} \tag{3.68}$$

Since total stress does not have an explicit formula in terms of displacements, equation (3.67) can be alternatively written by the use of stress resultants and substituting the axial strain from equation (3.64) as,

$$\begin{aligned}\delta U dt = \int_0^L \left(N\frac{\partial w}{\partial x}\frac{\partial\delta w}{\partial x} + N\frac{\partial\delta u}{\partial x} - M\frac{\partial^2\delta w}{\partial x^2}\right) dx + \\ \left[N^{(1)}\frac{\partial w}{\partial x}\frac{\partial\delta w}{\partial x} + N^{(1)}\frac{\partial\delta u}{\partial x} - M^{(1)}\frac{\partial^2\delta w}{\partial x^2}\right]\Bigg|_0^L\end{aligned} \tag{3.69}$$

where M, N, $M^{(1)}$, and $N^{(1)}$ are resultant total moment, total normal force, higher-order moment, and higher-order normal force, respectively; and they are defined as,

$$\{M, N, M^{(1)}, N^{(1)}\} = \int_A \{z t_{xx}, t_{xx}, z\sigma_{xx}^{(1)}, \sigma_{xx}^{(1)}\} \, dA \tag{3.70}$$

To be able to write the stress resultants in terms of displacement to be used further in the derivation, an easier form for the constitutive relations needs to be derived. By assuming kernel function given in equation (3.66) are the same for both classical and higher-order stresses and are defined by Eringen [63], a linear differential operator that works as the inverse of the convolution integral can be found using Green's function,

$$\mathcal{L}_i = 1 - (e_i a)^2 \nabla^2 \tag{3.71}$$

where ∇^2 is the Laplacian operator and is $\frac{\partial^2}{\partial x^2}$ for one dimensional case. By applying the linear differential operator of equation (3.71) twice (once per type of stress) on the total stress defined by equation (3.68) and substituting the constitutive relations given by equation (3.66),

$$\begin{aligned} &\left[1 - (e_0 a)^2 \nabla^2\right] \left[1 - (e_1 a)^2 \nabla^2\right] t_{xx} = \\ &E \left[1 - (e_1 a)^2 \nabla^2\right] \varepsilon_{xx} - E l^2 \left[1 - (e_0 a)^2 \nabla^2\right] \frac{\partial}{\partial x} \frac{\partial \varepsilon_{xx}}{\partial x} \end{aligned} \tag{3.72}$$

Further expanding the expression by explicitly writing the Laplacian,

$$\begin{aligned} &\left[1 - (e_0 a)^2 \frac{\partial^2}{\partial x^2} - (e_1 a)^2 \frac{\partial^2}{\partial x^2} - (e_0 a)^2 (e_1 a)^2 \frac{\partial^4}{\partial x^4}\right] t_{xx} = \\ &E\varepsilon_{xx} - E(e_0 a)^2 \frac{\partial^2 \varepsilon_{xx}}{\partial x^2} - E l^2 \frac{\partial^2 \varepsilon_{xx}}{\partial x^2} - E l^2 (e_1 a)^2 \frac{\partial^4 \varepsilon_{xx}}{\partial x^4} = \\ &E \left[1 - (e_0 a)^2 \frac{\partial^2}{\partial x^2} - l^2 \frac{\partial^2}{\partial x^2} - l^2 (e_1 a)^2 \frac{\partial^4}{\partial x^4}\right] \varepsilon_{xx} \end{aligned} \tag{3.73}$$

Following Lim et al. [76] derivation, by assuming there is a single nonlocal parameter for both classical and higher-order stresses (i.e., $e_0 a = e_1 a = ea$) and neglecting the terms higher derivative order than two (i.e., retaining the terms of order $\frac{\partial^2}{\partial x^2}$), simplified form can be found as

$$\left[1 - 2(ea)^2 \frac{\partial^2}{\partial x^2}\right] t_{xx} = E \left[1 - (ea)^2 \frac{\partial^2}{\partial x^2} - l^2 \frac{\partial^2}{\partial x^2}\right] \varepsilon_{xx} \tag{3.74}$$

which is not the one that is presented and is used in the literature. Taking the simplified constitutive relation directly from Lim et al. [76] it can be written as,

$$\left[1 - (ea)^2 \frac{\partial^2}{\partial x^2}\right] t_{xx} = E \left[1 - l^2 \frac{\partial^2}{\partial x^2}\right] \varepsilon_{xx} \tag{3.75}$$

which can only be obtained if and only if equality of nonlocal parameters are assumed equal before expanding, and then the extra linear differential operators are simplified using convolution integral.

A much easier and mathematically applicable method is to assume equality of non-local parameters for the linear differential operator defined in equation (3.71) and multiply both sides of equation (3.68) once and substitute the constitutive relations given by equation (3.66)

$$\left[1-(ea)^2\frac{\partial^2}{\partial x^2}\right]t_{xx}=E\varepsilon_{xx}-El^2\frac{\partial}{\partial x}\frac{\partial\varepsilon_{xx}}{\partial x}=E\left[1-l^2\frac{\partial^2}{\partial x^2}\right]\varepsilon_{xx} \tag{3.76}$$

Without further corrections or modifications to the NSGT formulation, multiplying both sides of the equation (3.70) by the linear differential operator defined in equation (3.71) stress resultants can be turned into a form that can utilize the constitutive relations,

$$\begin{aligned}&\left[1-(ea)^2\nabla^2\right]\{M,N,M^{(1)},N^{(1)}\}=\\&\left[1-(ea)^2\nabla^2\right]\int_A\left\{zt_{xx},t_{xx},z\sigma_{xx}^{(1)},\sigma_{xx}^{(1)}\right\}dA\end{aligned} \tag{3.77}$$

Since the area integral does not contain any x dependence, $\mathcal{L}$ can be moved inside of the integral and can directly be applied to the total and higher-order stresses, at which equation (3.76) can be substituted as,

$$\begin{aligned}&\left[1-(ea)^2\nabla^2\right]\{M,N,M^{(1)},N^{(1)}\}=\\&E\int_A\left\{z\left[1-l^2\frac{\partial^2}{\partial x^2}\right]\varepsilon_{xx},\left[1-l^2\frac{\partial^2}{\partial x^2}\right]\varepsilon_{xx},zl^2\frac{\partial^2}{\partial x^2}\varepsilon_{xx},l^2\frac{\partial^2}{\partial x^2}\varepsilon_{xx}\right\}dA\end{aligned} \tag{3.78}$$

Note that, strains can be expanded in terms of displacements using equation (3.64), however, it is left as it is for clarity.

With the variation of potential energy expression taken care of, kinetic energy and distributed external transverse load can be written as is done in the classical elasticity theory,

$$\begin{aligned}T_t&=\frac{1}{2}\int_V\rho_t\left[\left(\frac{\partial u_1}{\partial t}\right)^2+\left(\frac{\partial u_3}{\partial t}\right)^2\right]dV\\W&=\int_0^L(qw)\,dx\end{aligned} \tag{3.79}$$

where T_t is the kinetic energy of the tube, W is the non-conservative external work done on the system, and q is the force per unit area applied vertically to the system.

Substituting the displacements of equation (3.60) into the equation (3.79), kinetic energy expression can be written as,

$$T_t=\rho_t\int_0^L\left[I\left(\frac{\partial^2 w}{\partial x\,\partial t}\right)^2+A\left(\frac{\partial u}{\partial t}\right)^2+A\left(\frac{\partial w}{\partial t}\right)^2\right]dx \tag{3.80}$$

where I is the second moment of area and ρ_t is the density of the tube. For Euler-Beronulli beam theory rotary part is neglected as is done here, however, when it is not neglected beam theory becomes Rayleigh beam theory. Combining all terms of the total energy coming from equations (3.69)(3.79)(3.80) and equating its variation to zero as Hamilton's principle dictates as,

$$\int_{t_1}^{t_2} \delta\left(T_t - U + W\right) dt = 0 \tag{3.81}$$

Using integration by parts on equation (3.81), collecting coefficients of each individual displacement's variation and equating them to zero, the equation of motion without flow can be obtained,

$$\begin{aligned} \delta w \ &: \frac{\partial^2 M}{\partial x^2} + \frac{\partial N}{\partial x}\frac{\partial w}{\partial x} + N\frac{\partial^2 w}{\partial x^2} - \rho_t A\frac{\partial^2 w}{\partial t^2} = q \\ \delta u \ &: \frac{\partial N}{\partial x} - \rho_t A\frac{\partial^2 u}{\partial t^2} = 0 \end{aligned} \tag{3.82}$$

and corresponding boundary conditions are

$$\begin{aligned} N &= 0 && \text{or} && u = 0 && \text{at } x = 0, L \\ N^{(1)} &= 0 && \text{or} && \frac{\partial u}{\partial x} = 0 && \text{at } x = 0, L \\ \frac{\partial M}{\partial x} + \frac{\partial w}{\partial x}N &= 0 && \text{or} && w = 0 && \text{at } x = 0, L \\ M - \frac{\partial w}{\partial x}N^{(1)} &= 0 && \text{or} && \frac{\partial w}{\partial x} = 0 && \text{at } x = 0, L \\ M^{(1)} &= 0 && \text{or} && \frac{\partial^2 w}{\partial x^2} = 0 && \text{at } x = 0, L \end{aligned} \tag{3.83}$$

Writing the equation of motion can still be done at this step, however, it will be done for the final equation of motion where the fluid flow is also incorporated.

Instead by multiplying the axial part of the equation (3.82) by $\mathcal{L}$ and assuming the axial inertia is negligible, the equation can be simplified as the normal force becomes constant (C) after integrating. Integration constant C can be found following the procedure explained by Şimşek [83], first, the normal force resultant is written in terms of displacements using equation (3.78) and substituting equation (3.64),

$$\begin{aligned}
&N = E\int_A \left[1 - l^2\frac{\partial^2}{\partial x^2}\right]\left[\frac{\partial u}{\partial x} - z\frac{\partial^2 w}{\partial x^2} + \frac{1}{2}\left(\frac{\partial w}{\partial x}\right)^2\right] dA = C \\
&EA\left[\frac{\partial u}{\partial x} + \frac{1}{2}\left(\frac{\partial w}{\partial x}\right)^2\right] - EAl^2\left[\frac{\partial^3 u}{\partial x^3} + \frac{\partial^3 w}{\partial x^3}\frac{\partial w}{\partial x} + \left(\frac{\partial w^2}{\partial x^2}\right)^2\right] = C \qquad (3.84) \\
&\text{Alternatively : } \quad N = EA\left[\frac{\partial u}{\partial x} + \frac{1}{2}\left(\frac{\partial w}{\partial x}\right)^2\right] - EAN^{(1)} = C
\end{aligned}$$

Note that for mathematical rigor, the same manipulation can be made by first differentiating the axial part of the equation (3.82) and substituting the second derivative into the definition of total normal force definition of equation (3.78). To apply the boundary conditions of immovable ends which are

$$\begin{aligned}
&u(0,t) = 0, \quad u(L,t) = 0, \\
&\left.\frac{\partial u}{\partial x}\right|_{x=0} = 0, \quad \left.\frac{\partial u}{\partial x}\right|_{x=L} = 0 \quad \text{or} \quad N^{(1)}(0,t) = 0, \quad N^{(1)}(L,t) = 0
\end{aligned} \qquad (3.85)$$

where the first set is the classical conditions which has a physical meaning while the second set is the higher-order boundary conditions and does not have a physical analog. Hence, the choice between the two is ambiguous and the literature chooses the geometric one yet MD simulation calibration suggests that the natural one might be better [77].

Interestingly, Şimşek [83] does not use either of the higher-order boundary conditions, but equates the second-order derivative of axial displacement to zero with referencing to an article by Aifantis [134] in which the used boundary condition is not mentioned but only the higher order boundary condition for transverse direction is mentioned as is derived in equation (3.83). For completeness, and to not separate too far from the generally used methods, two derivations will be carried out, one using the $\frac{\partial^2 u}{\partial x^2}$ and the other one is the natural boundary condition coming from equation (3.85). Note that, the geometric one of equation (3.85) was not used because it produced a non-trivial solution for the displacement and at that point, it is not very far from solving two equations.

First, utilizing Şimşek's boundary condition; by integrating both sides of the equation (3.84) between 0 and L produces

$$\begin{aligned} &\underbrace{\left[u(L,t) - u(0,t) - l^2 \left.\frac{\partial^2 u}{\partial x^2}\right|_{x=L} + l^2 \left.\frac{\partial^2 u}{\partial x^2}\right|_{x=0}\right]}_{=0} \\ &+ \frac{1}{2}\int_0^L \left\{ \left(\frac{\partial w}{\partial x}\right)^2 - 2l^2 \left[\frac{\partial^3 w}{\partial x^3}\frac{\partial w}{\partial x} + \left(\frac{\partial w^2}{\partial x^2}\right)^2\right]\right\} dx = \frac{CL}{EA} \\ &\rightarrow C = \frac{EA}{2L}\int_0^L \left\{ \left(\frac{\partial w}{\partial x}\right)^2 - 2l^2 \left[\frac{\partial^3 w}{\partial x^3}\frac{\partial w}{\partial x} + \left(\frac{\partial w^2}{\partial x^2}\right)^2\right]\right\} dx \end{aligned} \tag{3.86}$$

Now, utilizing the natural boundary condition of equation (3.85); by integrating both sides of the alternative form of the equation (3.84) between 0 and L produces,

$$\begin{aligned} &\underbrace{\left[u(L,t) - u(0,t) + N^{(1)}(0,t) - N^{(1)}(L,t)\right]}_{=0} + \frac{1}{2}\int_0^L \left(\frac{\partial w}{\partial x}\right)^2 dx = \frac{CL}{EA} \\ &\rightarrow C = \frac{EA}{2L}\int_0^L \left(\frac{\partial w}{\partial x}\right)^2 dx \end{aligned} \tag{3.87}$$

where the integration constant becomes the one obtained with CET. Another fact that is noticed later in the study is that if the extra part of the integrand in equation (3.86) is examined, it can be written as the derivative of a function of x and t. Since the separation of variables will be assumed in any method of solution, under that assumption, integral can also be written in terms of the first derivative x as,

$$\int_0^x \left[\frac{\partial^3 w}{\partial x'^3}\frac{\partial w}{\partial x'} + \left(\frac{\partial w^2}{\partial x'^2}\right)^2\right] dx' = \int_0^x \frac{\partial}{\partial x'}\left[\frac{\partial^2 w}{\partial x'^2}\frac{\partial w}{\partial x'}\right] dx' \tag{3.88}$$

such that the fundamental theorem of calculus can be utilized (skipping the separation of variables and recombination) to obtain the solution analytically in terms of derivatives of w as,

$$F(x) = \int_0^x \frac{\partial}{\partial x'}\left[\frac{\partial^2 w}{\partial x'^2}\frac{\partial w}{\partial x'}\right] dx' = \frac{\partial^2 w}{\partial x^2}\frac{\partial w}{\partial x} \tag{3.89}$$

For $x = L$ or $x = 0$, either the first derivative or the second becomes zero for any boundary condition possible that can be written with equation (3.83), hence the extra part introduced does not contribute to nonlinearity at all. This is also the observation that is made using the GtDQM matrix form during the solution, such that only the form in equation (3.87) will be used.

The reduced form can now be obtained if equation (3.87) is used while defining the integration constant. Substituting the definition of $N(x,t) = C$ into equation (3.82),

$$\frac{\partial^2 M}{\partial x^2} + C\frac{\partial^2 w}{\partial x^2} - \rho_t A\frac{\partial^2 w}{\partial t^2} = q \tag{3.90}$$

3.4.2 Fluid-Structure interaction of Fluid Flow

Fluid-structure interaction terms can now be added to the nonlinear beam equation of motion separately. The most common way of including the effects of fluid flow is to model it as if an equivalent uniform flow is moving through the beam, in which fluid acts as a solid [89]. Furthermore, interaction terms can easily be obtained by writing the kinetic energy of the flowing fluid, since potential energy storage is limited.

Considering Euler-Bernoulli assumptions states that the slope at a point is directly the first derivative of the transverse deflection (i.e., $\frac{\partial w}{\partial x}$, and fluid is following the deformed beam the fluid kinetic energy can be written as,

$$T_f = \rho_f \int_V \left[\left(\frac{\partial u_1}{\partial t} + U \sqrt{1 - \left(\frac{\partial w}{\partial x} \right)^2} \right)^2 + \left(\frac{\partial u_3}{\partial t} + U \frac{\partial w}{\partial x} \right)^2 \right] dV \tag{3.91}$$

where ρ_f is fluid density, U is the flow velocity. Alternatively, Païdoussis [89] and other current literature [108, 113] uses the kinetic energy term derived without considering the motion difference along the z direction and uses mid-plane deflections to reflect the motion of the whole body. Using the inextensibility condition of clamped-clamped beams and using binomial approximation Païdoussis [89] derives the given kinetic energy definition for nonlinear (i.e., large deflection) beams,

$$T_f = \rho_f A_f \int_0^L \left[\left(\frac{\partial u}{\partial t} + U \left(1 + \frac{\partial u}{\partial x} \right) \right)^2 + \left(\frac{\partial w}{\partial t} + U \frac{\partial w}{\partial x} \right)^2 \right] dx \tag{3.92}$$

where A_f is the area where fluid can flow. Since, the scope of the thesis is to show the solution concept rather than correctly model the fluid-structure interaction, one used in the literature will be used.

Applying Hamilton's principle so that the fluid kinetic energy is the same as the rest of the equation of motion, its effect can be calculated as,

$$\begin{aligned} \delta w \ &: \frac{\partial^2 w}{\partial x^2} A_f \rho_f U^2 + 2 \frac{\partial^2 w}{\partial x \, \partial t} A_f \rho_f U + \frac{\partial^2 w}{\partial t^2} A_f \rho_f \\ \delta u \ &: \frac{\partial^2 u}{\partial x^2} A_f \rho_f U^2 + 2 \frac{\partial^2 u}{\partial x \, \partial t} A_f \rho_f U + \frac{\partial^2 u}{\partial t^2} A_f \rho_f \end{aligned} \tag{3.93}$$

At this stage, there are two corrections to the formula that is frequently used in literature. One is to multiply the centrifugal term (i.e., the term with U^2) with a correction factor that takes care of the actual non-uniformity of the flow profile while taking the cross-section integral between equations (3.91) and (3.92). For a fully developed and laminar flow parabolic flow profile gives a correction factor of $4/3$ while a turbulent flow generally produces a correction factor between 1 and $4/3$ depending on the turbulent characteristics of the flow [90].

Another, possibly more important, correction is to the changing mechanics of the flow in the nanoscale. Since the Knudsen number (Kn) is comparable to unity in very small length scales, which is the ratio of the molecular free path to the representative length of the flow, continuum flow assumptions may fail. One such assumption is the no-slip boundary condition at the fluid-structure interface fails and there becomes a non-zero slip velocity at the interface. This problem is somewhat mended by Beskok & Karniadakis [91] such that an effective flow speed is used which is a correction factor multiple of the expected flow speed of no-slip boundary condition. This correction factor may range from 1 to 5 for gaseous flows while it is very close to unity for nano-liquid flows [92], while experimental verification for the correction factor is needed, generally used correction factor is around 1.4 for comparison in the literature[108].

Since these correction factors do not modify the characteristics of interaction and are just a scale factor for the velocity, the main formula stays the same such that the method developed can be used with any correction that does not change the polynomial degree of the flow speed. Similar methods can also be applied to interaction models that rely on simplified Navier-Stokes equation solutions since nonlinear solution already needs iterations. However, in this work, no correction will be applied since the methods are still applicable with the only change being the scale of velocity.

Following the same derivation that is done to reduce the dependency of axial displacement, axial inertia terms are neglected and equation (3.93) is added to the equation (3.90)

$$\frac{\partial^2 M}{\partial x^2} + C\frac{\partial^2 w}{\partial x^2} - m\frac{\partial^2 w}{\partial t^2} - M_f\left(\frac{\partial^2 w}{\partial x^2}U^2 + 2U\frac{\partial^2 w}{\partial x\,\partial t} + \frac{\partial^2 w}{\partial t^2}\right) = q \tag{3.94}$$

where m, and M_f are the mass per unit length of the tube ($\rho_t A$), and mass per unit length of the fluid ($\rho_f A_f$), respectively.

To be able to use the constitutive relations, multiply both sides of equation (3.94) with $\mathcal{L}$. From the resulting equation, using the definitions of the total moment from equation (3.78) and strain definitions of equation (3.64) equation of motion in terms of mid-plane displacement can be obtained,

$$
\begin{aligned}
&U^2\left(1-(ea)^2\nabla^2\right)M_f\frac{\partial^2 w}{\partial x^2}+2U\left(1-(ea)^2\nabla^2\right)M_f\frac{\partial^2 w}{\partial x\,\partial t}\\
&+EI\left(1-l^2\nabla^2\right)\frac{\partial^4 w}{\partial x^4}-C\left(1-(ea)^2\nabla^2\right)\frac{\partial^2 w}{\partial x^2}\\
&+(M_f+m)\left(1-(ea)^2\nabla^2\right)\frac{\partial^2 w}{\partial t^2}=q
\end{aligned}
\tag{3.95}
$$

Since the order of magnitudes of different variables normalizing is necessary for stable solutions. Using the following non-dimensional parameters,

$$
\begin{aligned}
&x^*=\frac{x}{L},\ w^*=\frac{w}{h},\ \alpha=\frac{ea}{L},\ \xi=\frac{l}{L},\ S=\frac{d_0^2A}{I},\ t^*=\frac{t}{L^2}\sqrt{\frac{EI}{(M_f+m)}}\\
&\bar{q}=\frac{qL^4}{EIh},\ U^*=\sqrt{\frac{M_fL^2}{EI}}U,\ \overline{M}=\frac{M_f}{M_f+m},\ \omega^*=\omega L^2\sqrt{\frac{(M_f+m)}{EI}}
\end{aligned}
\tag{3.96}
$$

and applying $\nabla^2=\frac{\partial^2}{\partial x^2}$, non-dimensional equation of motion can be written as,

$$
\begin{aligned}
&U^{*2}\left(\frac{\partial^2 w^*}{\partial x^{*2}}-\alpha^2\frac{\partial^4 w^*}{\partial x^{*4}}\right)+2\sqrt{\overline{M}}U^*\left(\frac{\partial^2 w^*}{\partial x^*\partial t^*}-\alpha^2\frac{\partial^4 w^*}{\partial x^{*3}\partial t^*}\right)\\
&+\frac{\partial^4 w^*}{\partial x^{*4}}-\xi^2\frac{\partial^6 w^*}{\partial x^{*6}}-C\left(\frac{\partial^2 w^*}{\partial x^{*2}}-\alpha^2\frac{\partial^4 w^*}{\partial x^{*4}}\right)+\frac{\partial^2 w^*}{\partial t^{*2}}-\alpha^2\frac{\partial^4 w^*}{\partial x^{*2}\partial t^{*2}}=\bar{q}
\end{aligned}
\tag{3.97}
$$

where the integration constant C is defined by the equation (3.87),

$$
C=\frac{1}{2}S\int_0^1\left(\frac{\partial w^*}{\partial x^*}\right)^2dx^*
\tag{3.98}
$$

3.4.3 Applying GtDQM

Using the GtDQM definitions of equation (3.49), equation (3.97) can be discretized in spatial domain as,

$$
\left[\boldsymbol{K}+\boldsymbol{K_f}+\boldsymbol{K_{NL}}(\boldsymbol{w})\right]\boldsymbol{w}+\left[\boldsymbol{C}+\boldsymbol{C_f}+\boldsymbol{C_{NL}}(\boldsymbol{w})\right]\dot{\boldsymbol{w}}+\boldsymbol{M}\ddot{\boldsymbol{w}}=\boldsymbol{f}
\tag{3.99}
$$

where $\boldsymbol{K}$, $\boldsymbol{K_f}$, $\boldsymbol{K_{NL}}(\boldsymbol{w})$, $\boldsymbol{C}$, $\boldsymbol{C_f}$, $\boldsymbol{C_{NL}}(\boldsymbol{w})$, and $\boldsymbol{M}$ are the stiffness, stiffness of fluid flow, response-dependent nonlinear stiffness, proportional viscous damping, damping of fluid flow, nonlinear viscous damping, and mass matrices, respectively and defined as,

$$\begin{aligned}
&\boldsymbol{K} = \boldsymbol{T}^T\boldsymbol{P}\left[\boldsymbol{A^{(4)}} - \xi^2\boldsymbol{A^{(6)}}\right]\boldsymbol{T} \qquad \boldsymbol{K_f} = U^{*2}\boldsymbol{T}^T\boldsymbol{P}\left[\boldsymbol{A^{(2)}} - \alpha^2\boldsymbol{A^{(4)}}\right]\boldsymbol{T}\\
&\boldsymbol{K_{NL}} = \frac{1}{2}S\left[\beta^{11}\right]\boldsymbol{T}^T\boldsymbol{P}\left[\boldsymbol{A^{(2)}} - \alpha^2\boldsymbol{A^{(4)}}\right]\boldsymbol{T}\\
&\boldsymbol{M} = \boldsymbol{T}^T\boldsymbol{P}\left[\boldsymbol{I} - \alpha^2\boldsymbol{A^{(2)}}\right]\boldsymbol{T} \quad \boldsymbol{f} = \boldsymbol{T}^T\boldsymbol{P}\bar{\boldsymbol{q}}\\
&\boldsymbol{C} = \eta\boldsymbol{K} \quad \boldsymbol{C_{NL}} = \eta\boldsymbol{K_{NL}} \quad \boldsymbol{C_f} = 2\sqrt{\overline{M}}U^*\boldsymbol{T}^T\boldsymbol{P}\left[\boldsymbol{A^{(1)}} - \alpha^2\boldsymbol{A^{(3)}}\right]\boldsymbol{T}
\end{aligned} \tag{3.100}$$

where β^{nm} is the scalar-valued integral of product between n^{th} and m^{th} component of w^* which can be written as,

$$\beta^{nm} = \frac{1}{2}S\left(\boldsymbol{A^{(1)}}\boldsymbol{T}\boldsymbol{w_{d_n}}\right)^T\boldsymbol{P}\left(\boldsymbol{A^{(1)}}\boldsymbol{T}\boldsymbol{w_{d_m}}\right) \tag{3.101}$$

For the time domain equation, n and m are not necessary however for the harmonic balance they can be attributed to the sine or cosine parts.

Note that, the proportional viscous damping matrix is defined by utilizing Kelvin-Voigt viscoelastic model, where Young's Modulus (E) can alternatively be written as [78],

$$E^* = E\left(1 + \eta\frac{\partial}{\partial t}\right) \to \eta^* = \frac{\eta}{E}\sqrt{\frac{EI}{(Mf+m)L^4}} \tag{3.102}$$

to introduce some damping to the system, where E^* is the viscoelastic modulus and η is the damping ratio and η^* is the normalized damping ratio.

Furthermore, for the clamped-clamped (CC) case, elements of the boundary condition matrix ($\boldsymbol{B}$) can be written as,

$$\begin{aligned}
&B_{1j} = I_{1j} &&\text{and} \quad B_{2j} = I_{Nj}\\
&B_{3j} = A^{(1)}_{1j} &&\text{and} \quad B_{4j} = A^{(1)}_{Nj}\\
&B_{5j} = EIl^2A^{(4)}_{1j} &&\text{and} \quad B_{6j} = EIl^2A^{(4)}_{Nj}\\
\text{or} \quad &B_{5j} = A^{(2)}_{1j} &&\text{and} \quad B_{6j} = A^{(2)}_{Nj}
\end{aligned} \tag{3.103}$$

where the first option for the higher order boundary condition can be obtained by substituting boundary condition equation (3.83) into the higher order moment definition of equation (3.78). Note that, since there is no physical interpretation of higher-order stress, both boundary conditions can be applied to the problem.

Moreover, for the hinged-hinged (HH) case, which is simply supported with immovable endpoints, elements of the boundary condition will mostly be the same with equation (3.103), the only difference being the third row changing to other boundary condition option as,

$$B_{3j} = A_{1j}^{(2)} - \xi^2 A_{1j}^{(4)} \quad \text{and} \quad B_{4j} = A_{Nj}^{(2)} - \xi^2 A_{Nj}^{(4)} \tag{3.104}$$

which again can be derived by substitution and the earlier higher-order natural boundary condition of equation (3.85).

3.4.4 Frequency Domain Solution Methods

Stability analysis can be done by utilizing a state space form without forcing by adding an identity equation to equation (3.99) as,

$$\begin{bmatrix} 0 & \boldsymbol{M} \\ \boldsymbol{M} & \boldsymbol{C} + \boldsymbol{C_f} + \boldsymbol{C_{NL}} \end{bmatrix} \dot{\boldsymbol{y}} + \begin{bmatrix} -\boldsymbol{M} & 0 \\ 0 & \boldsymbol{K} + \boldsymbol{K_f} + \boldsymbol{K_{NL}} \end{bmatrix} \boldsymbol{y} = 0 \tag{3.105}$$

where $\boldsymbol{y} = \left\{ \dot{\boldsymbol{w}}^T \quad \boldsymbol{w}^T \right\}^T$ and if assumed a harmonic solution of the form $\boldsymbol{y} = \tilde{\boldsymbol{y}} e^{\lambda t}$, non-trivial solution of this problem would produce complex eigenvectors $\tilde{\boldsymbol{y}_n}$ and complex eigenvalues λ_n of the state space eigenvalue problem. The imaginary part of the eigenvalue $Im\left[\lambda_n\right]$ is the damped natural frequency (i.e., free vibration oscillation frequency), and the real part of the eigenvalue $Re\left[\lambda_n\right]$ is the decay rate.

When the decay rate becomes zero or positive instead of exponential decay, the system responds with an exponential increase in which catastrophic failure may occur. At the point of zero decay rate, if the damped natural frequency is zero, instability is of the divergence type; and if the natural frequency is not zero but a positive value, then the instability is fluttering instability. Instability graphs can be obtained by the solution of the state space eigenvalue problem coming from equation (3.105) at different flow speeds with the lowest few modes such that point of instability and mode of instability can be seen clearly.

Noting that directly solving the nonlinear equation is not applicable since the resulting eigenvectors change the stiffness matrix they are created, hence an iterative algorithm is needed such as Newton's method that needs to iteratively solve the problem at each iteration step. Alongside long solution times, this solution method may also create convergence problems [104].

Alternatively, the nonlinear problem can be solved with time domain integration methods at which time domain simulation can be done step-by-step with lots of different initial conditions to obtain, phase-plane diagrams or bifurcation diagrams to capture the characteristics of nonlinearity [110]. These computationally very expensive methods not only lack in some problems but also may fail to capture the post-instability regions.

The newly proposed method by Kösterit and Cigeroglu [135] uses Newton's method with pseudo-arc-length continuation after applying the harmonic balance method (HBM) to predict the critical flutter speed and post-flutter characteristics, in which it will be expanded to be used in fluid conveying carbon nanotubes.

Assuming a forcing of the form $q = q_0 \sin \omega t$solution of the form $\boldsymbol{w_d} = \boldsymbol{w_{d_s}} \sin \omega t + \boldsymbol{w_{d_c}} \cos \omega t$ where, $\boldsymbol{w_{d_s}}$ and $\boldsymbol{w_{d_c}}$ are the sine and cosine coefficients of the harmonic solution and applying harmonic balance to the equation (3.99), the approximate periodic solution can be written as,

$$\begin{bmatrix} \boldsymbol{K} + \boldsymbol{K_f} - \omega^2 \boldsymbol{M} & -\omega \left(\boldsymbol{C} + \boldsymbol{C_f} \right) \\ \omega \left(\boldsymbol{C} + \boldsymbol{C_f} \right) & \boldsymbol{K} + \boldsymbol{K_f} - \omega^2 \boldsymbol{M} \end{bmatrix} \begin{Bmatrix} \boldsymbol{w_{d_s}} \\ \boldsymbol{w_{d_c}} \end{Bmatrix} + \boldsymbol{f_{NL}} + \boldsymbol{f'_{NL}} = \begin{Bmatrix} \boldsymbol{f_0} \\ \boldsymbol{0} \end{Bmatrix} \tag{3.106}$$

details of the derivation will be given in the Appendix B. In this form, a forced response of the system can be obtained and response-dependent FRFs can be drawn. In this form number of unknowns are in total $2N + 1$, since there are each N unknowns for cosine and sine parts and there is also the unknown frequency variable. If ω is taken to be a predetermined value, then the solution to the $2N$ nonlinear algebraic equations can be obtained by the use of Newton's method. Furthermore, introducing an equation for a $2N + 1$ dimensional hyper-sphere, then the solution to the $2N + 1$ nonlinear algebraic equations can be obtained by the use of Newton's method with pseudo-arc-length continuation. With this change of variables, ω becomes an unknown, and the arc length becomes the predetermined value or known variable value in the case of adaptive step size.

If instead the free vibration natural frequency of the system was wanted, ω becomes unknown without including the path following, so that number of unknowns becomes

$2N+1$ with $2N$ equations. Hence one extra equation is needed to be able to solve the system, which is generally taken to be the amplitude of vibration of a specific point. This makes it so that the eigenvectors become scaled to reach a specific amplitude at a specific point, where the specific point is taken to be the maximum deflection point which is the mid-point of the beam for clamped-clamped beams. If any other specific point wants to be utilized, a specific row of the coordinate up-scaling matrix $\mathcal{T}$ can be used where the up-scaled grid includes the specific point in need.

Now, the system can be solved non-trivially with $2N + 2$ unknowns and $2N + 1$ equations by defining the vibration amplitude to a predetermined value. Similarly, the pseudo-arc-length continuation can be utilized by adding a $2N + 2$ hyper sphere equation and making amplitude a variable. With this solution method backbone curve of the structure can be obtained where the natural frequency of the system is obtained for different vibration amplitudes.

With similar logic, if the flow speed U^* is not a prescribed value but taken to be an unknown value, the critical speed at which instability occurs U^*_{cr} can be found. The number of unknowns is $2N+4$, where $2N$ comes from the sine and cosine deflection values, 2 comes from the real and imaginary parts of the eigenvalue λ, 1 comes from the amplitude of vibration, and 1 comes from the critical flow speed U^*_{cr}. Similarly, the number of equations needs to be increased by two from the backbone method to accommodate the new unknowns. Knowing the mode shapes of damped structures are complex and should have phase differences between each point in the domain, by fixing the phase of a specific point to zero a new equation is found where 0 does not contribute to the number of unknowns. Furthermore, at the point of instability, the complex part of the eigenvalue becomes zero by definition of instability, hence a new equation can also be written or else the complex part of the frequency may not even be used since it will be zero. Using the latter method, the number of unknowns is $2N + 3$ and the total number of equations is $2N + 2$ hence the solution can be obtained by determining a vibration amplitude.

By utilizing the pseudo-arc-length continuation by adding a $2N + 3$ hyper sphere equation and making amplitude a variable, critical flow velocity can be obtained with variable amplitude. This would show the maximum deflection possible at a specific flow velocity even after experiencing instability. Such knowledge might be very important because large deflections that are comparable with the thickness of the beam but far from the failure may result in favorable properties such as quasi-zero stiffness[113].

Furthermore, this method can also be expanded to obtain the critical flow velocity for changing problem parameters, whether it be the nonlocal parameter, length-scale parameter, or any other geometric or material parameter. This can be achieved by taking the predetermined vibration amplitude to be fixed throughout the analysis but keeping the equation that equates the deflection of a point to the prescribed value. While the unknown number decreases by one since it is a user-defined parameter, the equation number stays the same; and if solved would produce a quasi-linear system with a prescribed deflection value. Instead, this extra equation can be used to path follow through the given parameter between some range and hence a graph for the solution can be obtained for changing variable that achieves the defined deflection value.

Different analysis methodologies given here are summarized in the table 3.1 to be able to keep easier track of added equations or variables. A mathematical manner of telling was not preferred since it would not add any new information but only complicate the articulation of ideas since most of the equations or unknowns are named with words.

Table 3.1: Summary for the number of unknowns and equations coming from an equation or a variable for different analysis

Analysis Type	Equation or variable	Number of unknown	Number of equation
Forced Response	Equation of motion	$2N$	$2N$
	Frequency (ω)	1	0
	Hyper-sphere equation	0	1
	Total	$2N+1$	$2N+1$
Free Vibration	Equation of motion	$2N$	$2N$
	Frequency (ω)	1	0
	Hyper-sphere equation	0	1
	Prescribed deflection	1	1
	Total	$2N+2$	$2N+2$
Critical Flow Speed	Equation of motion	$2N$	$2N$
	Frequency (ω)	1	0
	Hyper-sphere equation	0	1
	Prescribed deflection amplitude	1	1
	Flow Speed	1	0
	Prescribed deflection phase	0	1
	Total	$2N+3$	$2N+3$
Changing Parameter	Equation of motion	$2N$	$2N$
	Frequency (ω)	1	0
	Hyper-sphere equation	0	1
	Problem parameter	1	0
	Prescribed deflection amplitude	0	1
	Flow Speed	1	0
	Prescribed deflection phase	0	1
	Total	$2N+3$	$2N+3$

CHAPTER 4

VERIFICATION AND COMPARISON OF NUMERICAL METHODS

Finally, validation and comparison of our novel method to other common GDQM formulations are performed on the examples of Euler-Bernoulli beam and Timoshenko beam problems with different boundary conditions as well as a nonlinear beam example with cubic nonlinearity. In all cases, our method Galerkin transformed DQM (GtDQM) has better accuracy, convergence rate, and stability compared to commonly used GDQM formulations without any significant computational cost.

4.1 Verification of Symmetry

First, the up-scaling matrix for which the resolution of sampling can be increased is verified whit a trivial example. For an arbitrary 5^{th} order polynomial

$$f(x) = x - 4x^2 + 3x^3 - 2x^4 + x^5 \tag{4.1}$$

actual function value and up-scaled function value obtained from N number of discrete points are compared using integral square error defined by

$$\int_{x_a}^{x_b} f(x) - \mathcal{T} f(x_i) dx. \tag{4.2}$$

To approximate a continuous function, 10000-point sampled actual function values and 10000-point up-scaled function values are used in the numerical integral calculation in the domain of $[0, 0.5]$ and the resulting integral error for different number of discrete points N is given in figure 4.1a. Moreover, in the figure 4.1b the actual curve, the curve obtained by up-scaling the $N = 6$ representation, and the curve obtained by shifting the $N = 6$ representation to domain $[0.5, 1.5]$ can be seen. As expected, after reaching the number of sampling points of polynomial order, the error is numerically zero and the function can be represented exactly in the domain as well as outside of the domain (considering the function is defined and at the same order).

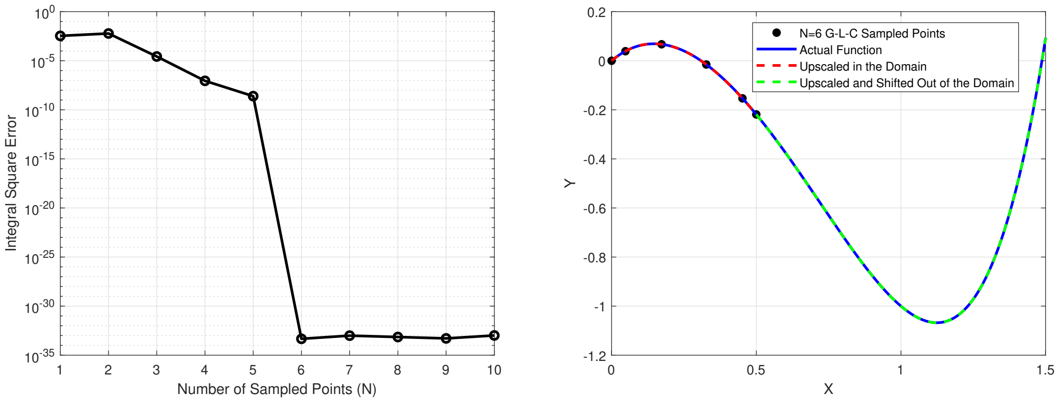

(a) Integral square error

(b) values of the function

Figure 4.1: Integral square error for different number of sampling points (a), values of the function with different methods (b)

Next, it will be shown that the stiffness matrices are symmetric for different boundary conditions of a uniform Euler-Bernoulli beam. For that, the stiffness operator/matrix can be written as

$$A[\ ] = \frac{\partial^4}{\partial x^4}, \qquad \boldsymbol{A} = \boldsymbol{A}^{(4)}, \qquad \boldsymbol{K} = \boldsymbol{T}^T \boldsymbol{P} \boldsymbol{A}^{(4)} \boldsymbol{T} \tag{4.3}$$

where transformation matrix $\boldsymbol{T}$ is obtained as explained in equation (3.25) from boundary condition matrix that can be constructed from the boundary condition information given as

$$\begin{aligned}
&\text{Clamped end (C)} && : \ w\left(X_b, t\right) = 0 && \text{and} \ \left.\frac{dw}{dx}\right|_{(x=X_b,t)} = 0 \\
&\text{Free end (F)} && : \ \left.\frac{d^2w}{dx^2}\right|_{(x=X_b,t)} = 0 && \text{and} \ \left.\frac{d^3w}{dx^3}\right|_{(x=X_b,t)} = 0 \\
&\text{Simply-Supported end (S)} && : \ w\left(X_b, t\right) = 0 && \text{and} \ \left.\frac{d^2w}{dx^2}\right|_{(x=X_b,t)} = 0
\end{aligned} \tag{4.4}$$

Here X_b refers to the boundary point, which is generally 0 or L and the naming convention will be to use capital letters for each end point's boundary for example 'CF' for a cantilevered (clamped free) beam.

To measure how symmetric a matrix is, numerically, the skew-symmetric part can be element-wise divided into symmetric part and the absolute maximum element of the division can be taken; shown mathematically as

$$S = \max\left(\left|\left(\boldsymbol{K} - \boldsymbol{K}^T\right) \oslash \left(\boldsymbol{K} + \boldsymbol{K}^T\right)\right|\right) \tag{4.5}$$

Symmetry ratio calculated from equation (4.5) is shown in figure 4.2 for different number of Gauss-Lobatto-Chebyshev sampled points for different boundary conditions and different methods of application explained in the earlier section. This shows that the stiffness matrix obtained by using GtDQM can be safely considered symmetric for numerical applications. Even though just using the transformation method is still better than the traditional elimination method, it cannot be considered symmetric. Similar results can also be obtained for a uniform grid which produces a steeper increase with the increasing number of sampled points and can be considered symmetric may be up to 50 sampled points

To verify the method further and assess its ability to obtain correct numerical results, different types of boundary condition applications with different case studies will be concentrated on.

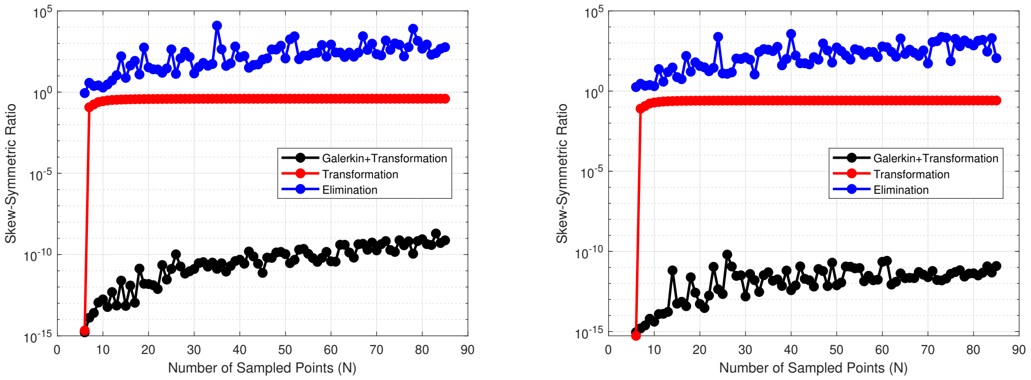

(a) SS

(b) CC

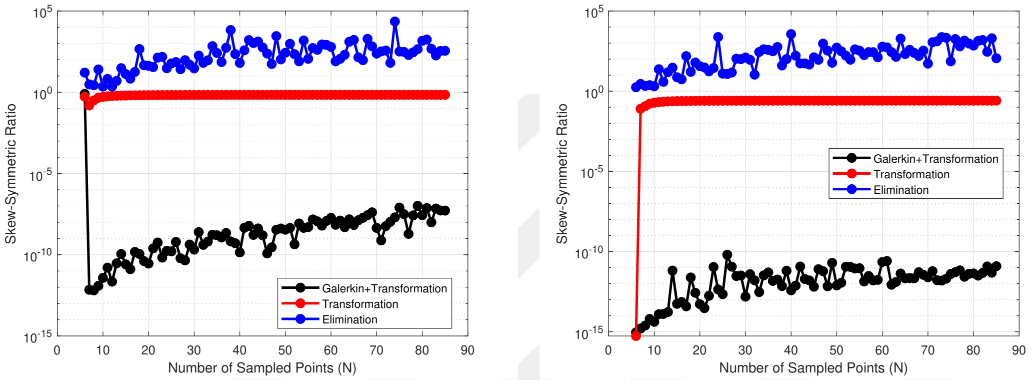

(c) FF

(d) CS

Figure 4.2: Skew-Symmetric to Symmetric ratio for different number of sampled points for a uniform Euler-Bernoulli beam subject to (a) SS, (b) CC, (c) FF, (d) CS boundary conditions

4.2 Case Study 1: Free Vibration of Uniform Euler-Bernoulli Beams

A uniform beam theory with Euler-Bernoulli assumptions can be written as

$$EI\frac{\partial^4 w}{\partial x^4} + \rho A\frac{\partial^2 w}{\partial t^2} = f(x,t) \tag{4.6}$$

where E is the Young's modulus, I is the moment of inertia about the bending axis, ρ is the density and A is the cross-sectional area of the beam. Which can be subject to different boundary conditions from each end. Different boundary conditions that are used are expressed in equation (4.4) and can also be used directly for this case as well.

In free vibration analysis, by assuming deflections are harmonic in time (i.e., $w\left(x,t\right) = W\left(x\right)\sin\omega t$) and forcing is zero, the equation is converted into an eigenvalue problem.

$$EI\frac{d^4 W}{dx^4} - \omega^2 \rho A W(x) = 0 \tag{4.7}$$

where ω is the natural frequency and can be found from the zeroes of characteristic equations shown in table 4.1 for different boundary conditions [128], with the definition of

$$\omega = \beta_n^2\sqrt{\frac{EI}{\rho A}} \tag{4.8}$$

Then, the equations can be written in the matrix form for any boundary condition using the GtDQM as,

$$\boldsymbol{K} = EI\boldsymbol{T}^T\boldsymbol{P}\boldsymbol{A}^{(4)}\boldsymbol{T}, \qquad \boldsymbol{M} = \rho A\boldsymbol{T}^T\boldsymbol{P}\boldsymbol{I}\boldsymbol{T} \tag{4.9}$$

and natural frequencies are obtained by the eigenvalue solver of MATLAB's eig() [133] command.

After obtaining the natural frequencies, they are compared with the exact natural frequencies obtained by solving the transcendental equations given in the table using an absolute relative error given as

$$\varepsilon_{relative,absolute} = \left|\frac{\omega_n^{approximate} - \omega_n^{exact}}{\omega_n^{exact}}\right| \tag{4.10}$$

Table 4.1: Characteristic equation and mathematical expressions for different boundary conditions of uniform Euler-Bernoulli beam theory

Boundary Condition Name	Boundary Condition	Characteristic Equation
Both ends simply supported (SS)	$W\left(0\right)=0,\ \left.\frac{d^2W}{dx^2}\right\|_{x=0}=0$ $W\left(L\right)=0,\ \left.\frac{d^2W}{dx^2}\right\|_{x=L}=0$	$\sinh\beta_n L * \sin\beta_n L=0$
Both ends clamped (CC)	$W\left(0\right)=0,\ \left.\frac{dW}{dx}\right\|_{x=0}=0,$ $W\left(L\right)=0,\ \left.\frac{dW}{dx}\right\|_{x=L}=0$	$\cosh\beta_n L * \cos\beta_n L-1=0$
Both ends free (FF)	$\left.\frac{d^2W}{dx^2}\right\|_{x=0}=0,\ \left.\frac{d^3W}{dx^3}\right\|_{x=0}=0$ $\left.\frac{d^2W}{dx^2}\right\|_{x=0}=0,\ \left.\frac{d^3W}{dx^3}\right\|_{x=0}=0$	$\cosh\beta_n L * \cos\beta_n L-1=0$
One end clamped and the other end simply supported (CS)	$W\left(0\right)=0,\ \left.\frac{dW}{dx}\right\|_{x=0}=0,$ $W\left(L\right)=0,\ \left.\frac{d^2W}{dx^2}\right\|_{x=L}=0$	$\tanh\beta_n L-\tan\beta_n L=0$

In figure 4.3 absolute relative error of the first natural frequency is shown as a convergence analysis for the material and geometric parameters of $E=70\ GPa$, $\rho=2700\ kg/m^3$, $L=1\ m$, $h=0.1\ m$, $b=0.2\ m$; where L, h, b refers to length, height, depth of the beam. Looking at the figure 4.3 GtDQM, GtDQM without applying the Galerkin method (Transformation method), and indirect replacement method have much smaller lowest error value compared to methods that utilize δ technique. Even though the convergence rate is about the same for all methods, GtDQM has a much lower starting point which makes it desirable for faster convergence.

Moreover, the ratio of real eigenvalues to all eigenvalues is given in the figure 4.4, where zero natural frequency that should be obtained from rigid body modes for the FF beam is not considered since they are usually found as complex numbers that are very close to zero. It can be clearly seen that not using the δ technique to implement boundary conditions increases the stability the of eigenvalue problem, either by using our transformation method or by using matrix manipulations. However, for general boundary conditions matrix manipulation may not be applicable, for example, the cantilevered (CF) beam solution could not be reliably achieved by using matrix manipulations by the author.

Finally, the convergence rate for the first four natural frequencies as the absolute relative error is given using GtDQM in figure 4.5. Choosing 0.1% (10^{-3}) absolute relative error as our desired error value, it can be observed that each natural frequency obtains desired error value rather fast. Considering the four boundary condition equation reduces the size of the system matrices by 4, the actual size of the system matrix needed to obtain the desired error is around twice the number of the natural frequency, somewhat, is in line with the rule of thumb that states only around half of the obtained total eigenvalues are satisfactory.

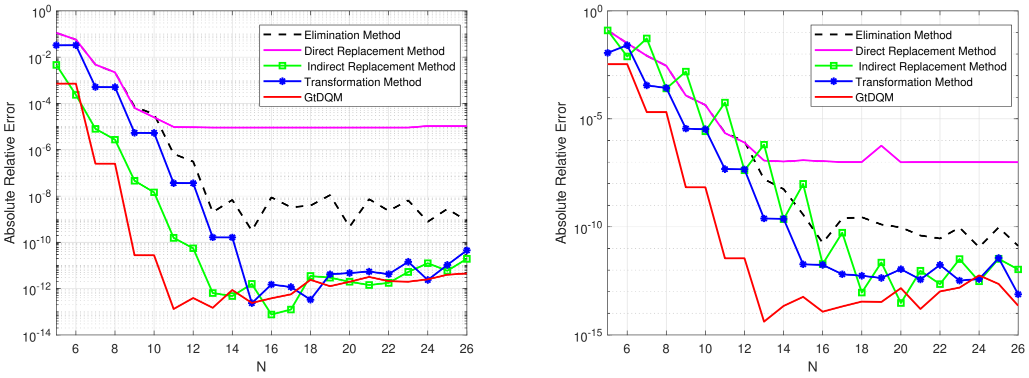

(a) SS (b) CC

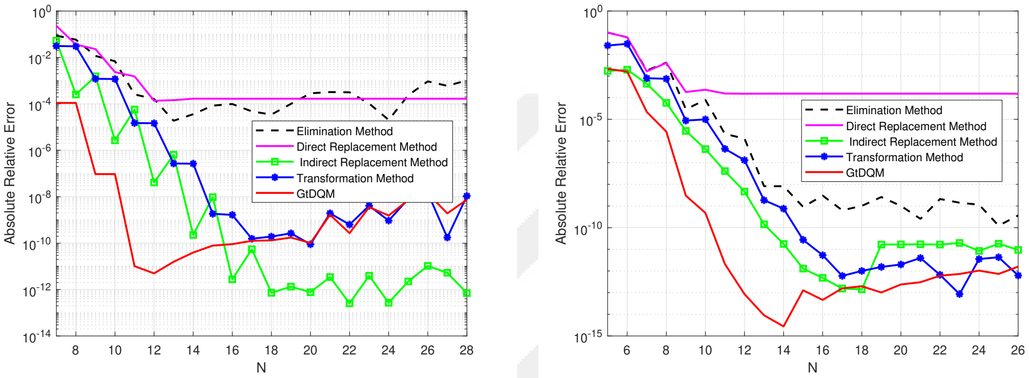

(c) FF (d) CS

Figure 4.3: Absolute relative error of the first natural frequency for a uniform Euler-Bernoulli beam subject to (a) SS, (b) CC, (c) FF, (d) CS boundary conditions using different boundary condition implementations

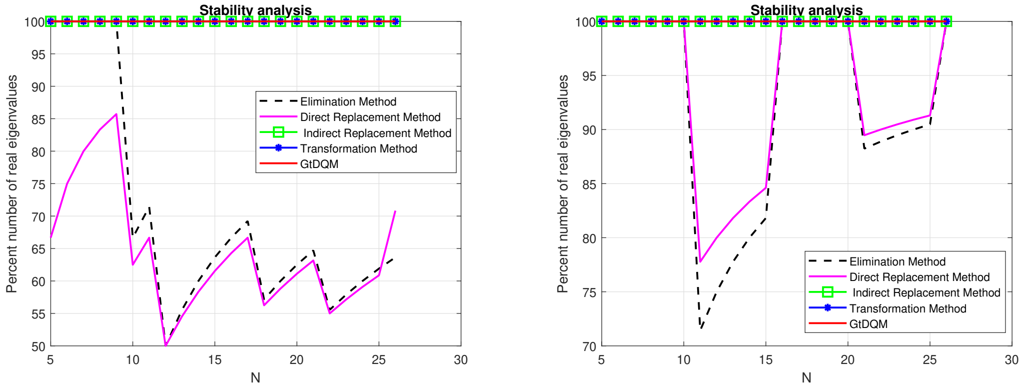

(a) SS (b) CC

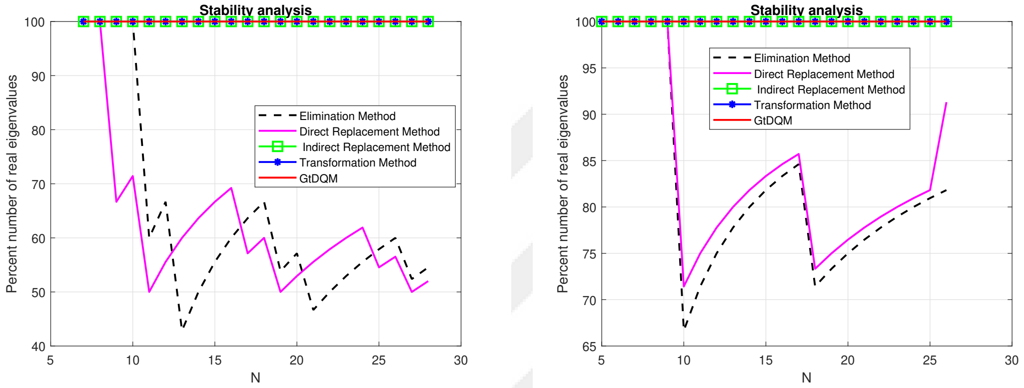

(c) FF (d) CS

Figure 4.4: Percent ratio of real eigenvalues to total eigenvalues for a uniform Euler-Bernoulli beam subject to (a) SS, (b) CC, (c) FF, (d) CS boundary conditions

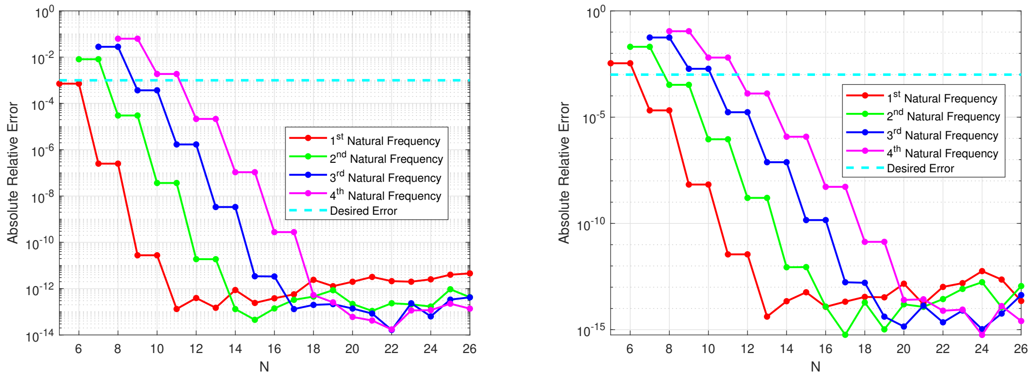

(a) SS (b) CC

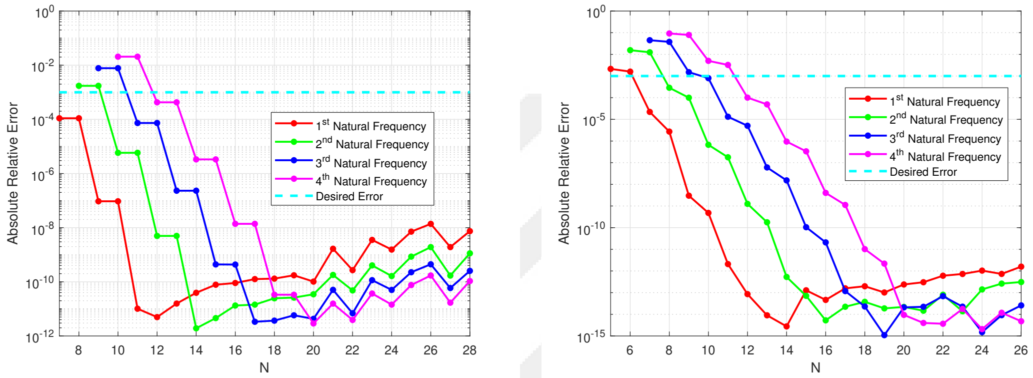

(c) FF (d) CS

Figure 4.5: Absolute relative error of the first four natural frequency for a uniform Euler-Bernoulli beam subject to (a) SS, (b) CC, (c) FF, (d) CS boundary conditions using GtDQM

4.3 Case Study 2: Free Vibration of Uniform Timoshenko Beams

The equation of motion of a uniform beam can be written using Timoshenko beam theory [136] as

$$\begin{aligned} \kappa AG\left(\frac{\partial^2 w}{\partial x^2}-\frac{\partial \phi}{\partial x}\right) &= \rho A\frac{\partial^2 w}{\partial t^2}-f(x,t) \\ EI\frac{\partial^2 \phi}{\partial x^2}+\kappa AG\left(\frac{\partial w}{\partial x}-\phi\right) &= \rho I\frac{\partial^2 \phi}{\partial t^2} \end{aligned} \tag{4.11}$$

which κ and G refers to shear correction factor and shear modulus respectively while ϕ refers to mid-plane rotation coordinate. In this form effects of rotatory inertia and shear forces are also included in the equation of motion. Similarly, by assuming harmonic time response natural frequencies ω can be obtained as the zeroes of characteristic equations shown in table 4.2 for different boundary conditions which need to be solved numerically since equations are implicit [137]. The equations can be written in the matrix form for any boundary condition using GtDQM as

$$\begin{aligned} \boldsymbol{K} &= \boldsymbol{T}^T \begin{bmatrix} \boldsymbol{P} & 0 \\ 0 & \boldsymbol{P} \end{bmatrix} \begin{bmatrix} \kappa AG\boldsymbol{A}^{(2)} & -\kappa AG\boldsymbol{A}^{(1)} \\ \kappa AG\boldsymbol{A}^{(1)} & EI\boldsymbol{A}^{(2)}-\kappa AG\boldsymbol{I} \end{bmatrix} \boldsymbol{T} \\ \boldsymbol{M} &= \boldsymbol{T}^T \begin{bmatrix} \boldsymbol{P} & 0 \\ 0 & \boldsymbol{P} \end{bmatrix} \begin{bmatrix} \rho A\boldsymbol{I} & 0 \\ 0 & \rho I\boldsymbol{I} \end{bmatrix} \boldsymbol{T} \end{aligned} \tag{4.12}$$

The displacement vector is constructed as $\begin{Bmatrix} w^T & \phi^T \end{Bmatrix}^T$ and natural frequencies are obtained by the MATLAB's eig() eigenvalue solver.

As the case study, the Timoshenko beam model reduces the fourth-order differential equation into a system of second-order differential equations in which δ technique is not needed while implementing boundary conditions. Therefore, the only difference between δ technique and the transformation method becomes solving the equation of motion at the boundary nodes which creates a minuscule difference between the two methods. This is observable in the figure 4.6 where natural frequencies are compared with analytical ones using absolute relative error defined in equation (4.10) for the parameters of $E = 70\ GPa$, $G = 26\ GPa$, $\rho = 2700\ kg/m^3$, $L = 1\ m$, $h = 0.1\ m$, $b = 0.2\ m$, and $\kappa = \frac{5}{6}$.

Table 4.2: Characteristic equation and mathematical expressions for different boundary conditions of uniform Timoshenko beam theory

Boundary Condition Name	Boundary Condition	Characteristic Equation
Both ends simply supported (SS)	$WW\left(0\right)=0,\ \left.\frac{d\phi}{dx}\right\rvert_{x=0}=0$ $WW\left(L\right)=0,\ \left.\frac{d\phi}{dx}\right\rvert_{x=L}=0$	$\sin s_2=0$
Both ends clamped (CC)	$WW\left(0\right)=0,\quad \phi(0)=0$ $WW\left(L\right)=0,\quad \phi(L)=0$	$0=c_1\left(\cosh s_1-\cos s_2\right)^2-$ $\left(c_1\sinh s_1-c_2\sin s_2\right)\left(\sinh s_1+\frac{c_1}{c_2}\sin s_2\right)$
Both ends free (FF)	$\left.\frac{d\phi}{dx}\right\rvert_{x=0}=0,\ \frac{1}{L}\left.\frac{dW}{dx}\right\rvert_{x=0}-\phi(0)=0$ $\left.\frac{d\phi}{dx}\right\rvert_{x=L}=0,\ \frac{1}{L}\left.\frac{dW}{dx}\right\rvert_{x=L}-\phi(L)=0$	$0=c_1s_1\left(\frac{s_1}{L}-c_1\right)\left(\cosh s_1-\cos s_2\right)^2$ $-\left(c_1s_1\sinh s_1-\frac{\frac{s_1}{L}-c_1}{\frac{s_2}{L}+c_2}c_2s_2\sin s_2\right)\times$ $\left(\left(\frac{s_1}{L}-c_1\right)\sinh s_1+\frac{c_1s_1}{c_2s_2}\left(\frac{s_2}{L}+c_2\right)\sin s_2\right)$
One end clamped and the other end simply supported (CS)	$W\left(0\right)=0,\quad \phi(0)=0$ $W\left(L\right)=0,\ \left.\frac{d\phi}{dx}\right\rvert_{x=L}=0$	$c_1\left(\cosh s_1-\cos s_2\right)\left(s_1\sinh s_1+s_2\sin s_2\right)-$ $\left(\sinh s_1+\frac{c_1}{c_2}\sin s_2\right)\times\left(c_1s_1\cosh s_1-\right.$ $\left.s_2c_2\cos s_2\right)=0$

*where $a=\frac{EI}{\rho AL^4},\quad b=\frac{I}{AL^2}\left(1+\frac{E}{\kappa G}\right)\omega_n^2,\quad c=\frac{\rho I}{\kappa AG}\omega_n^4-\omega_n^2$

Only the case for $\sqrt{b^2-4ac}>b$ is given since the other case corresponds to high-frequency excitation those frequencies are not reached.

$s_1=\sqrt{\frac{-b+\sqrt{b^2-4ac}}{2a}},\quad s_2=\sqrt{\frac{b+\sqrt{b^2-4ac}}{2a}},\quad c_1=\frac{1}{s_1}\left(\frac{\rho L}{\kappa G}\omega_n^2+\frac{1}{L}s_1^2\right),\quad c_2=\frac{1}{s_2}\left(\frac{\rho L}{\kappa G}\omega_n^2-\frac{1}{L}s_2^2\right),$

In this case study, it can be seen that applying the Galerkin method slightly increases the convergence rate, in which a smaller number of internal nodes are needed to achieve the same convergence if the Galerkin method is implemented on top of the transformation method. This increase in convergence rate could not be solely attributed to the Galerkin method for Euler- Bernoulli beam since not using the δ technique also contributes to the convergence rate.

Note that direct or indirect replacement methods were not shown for this case since direct replacement was unstable and indirect replacement was not trivial to implement, which in turn shows the disadvantages of the methods. Furthermore, stability analysis is not shown here for brevity since there were not many stability problems except for one or two values for the number of internal nodes, and GtDQM was not affected by instabilities at all.

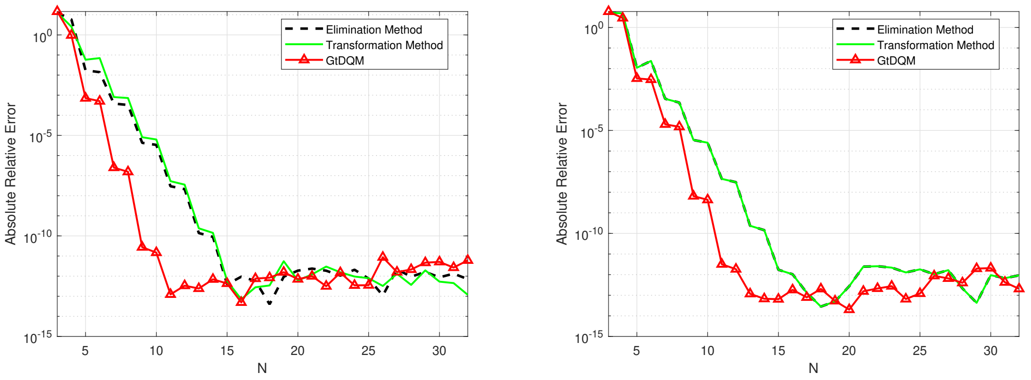

(a) SS

(b) CC

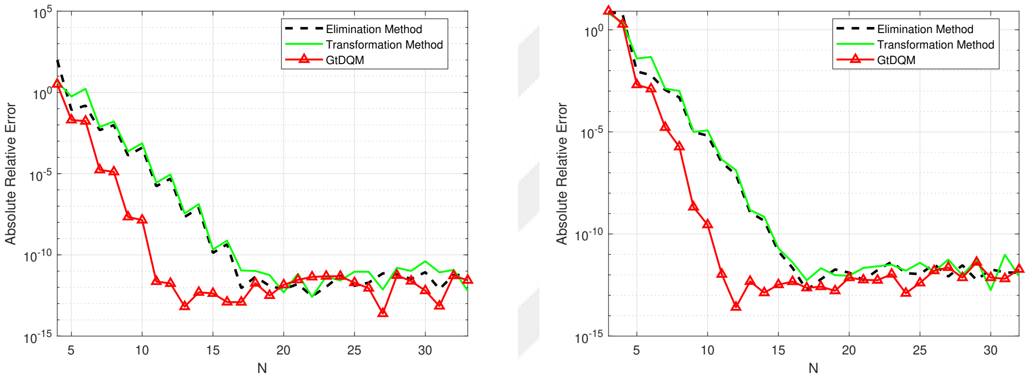

(c) FF

(d) CS

Figure 4.6: Absolute relative error of the first natural frequency for a uniform Timoshenko beam subject to (a) SS, (b) CC, (c) FF, (d) CS boundary conditions using different boundary condition implementations

4.4 Case Study 3: Forced Vibration of Uniform Euler-Bernoulli Beams with large deflection nonlinearity

To show the GtDQM nonlinear capabilities, an Euler-Bernoulli beam with large deflection nonlinearity will be solved. This case is chosen because in the literature there are two articles that formulate the same problem by using GDQM [16] and by using Galerkin method [138], moreover the equation of motion can be reduced to our case so that further explanations about derivation or methods can be obtained from those articles.

The equation of motion of an Euler-Bernoulli beam with large deflection nonlinearity with structural damping can be written as

$$EI\,(1+\boldsymbol{i}\gamma)\,\frac{\partial^4 w}{\partial x^4} + \rho A\frac{\partial^2 w}{\partial t^2} = \frac{EA}{L}\int_0^L \frac{1}{2}\left(\frac{\partial w}{\partial x}\right)^2 dx \; + f(x,t) \tag{4.13}$$

where $\boldsymbol{i} = \sqrt{-1}$ is the imaginary number. Structural damping is assigned so that forced response can be achieved without divergence problems. By assuming harmonic deflection and forcing in complex form ($w\,(x,t) = \widetilde{W}\,(x)\,e^{\boldsymbol{i}\omega t}$ and $f\,(x,t) = Re\left[q\,(x)\,e^{\boldsymbol{i}\omega t}\right]$) in line with Harmonic Balance Method (HBM), $2 \times N$ set of equations can be derived that will be solved to obtain the forced response of the beam. For the GtDQM framework, this set of residual equations (R) can be written as

$$R = \left[EI\boldsymbol{K_L^*} - \omega^2\rho A\boldsymbol{M} + \frac{EA}{2L}\boldsymbol{K_{NL}}\right]\begin{Bmatrix}\boldsymbol{w_{d_R}}\\ \boldsymbol{w_{d_I}}\end{Bmatrix} - \boldsymbol{T}^T\boldsymbol{P}\begin{Bmatrix}\boldsymbol{q}_R\\ 0\end{Bmatrix} = \boldsymbol{0} \tag{4.14}$$

Where subscripts R and I refer to real and imaginary parts of the complex deflection; $\boldsymbol{K_L}$ and $\boldsymbol{K_{NL}}$ are linear and nonlinear stiffness matrices which can be written as

$$\begin{gathered}\boldsymbol{K_L^*} = \begin{bmatrix}\boldsymbol{T}^T\boldsymbol{P}\boldsymbol{A}^{(4)}\boldsymbol{T} & -\gamma\boldsymbol{T}^T\boldsymbol{P}\boldsymbol{A}^{(4)}\boldsymbol{T}\\ \gamma\boldsymbol{T}^T\boldsymbol{P}\boldsymbol{A}^{(4)}\boldsymbol{T} & \boldsymbol{T}^T\boldsymbol{P}\boldsymbol{A}^{(4)}\boldsymbol{T}\end{bmatrix},\\ \boldsymbol{M} = \begin{bmatrix}\boldsymbol{T}^T\boldsymbol{P}\boldsymbol{I}\boldsymbol{T} & 0\\ 0 & \boldsymbol{T}^T\boldsymbol{P}\boldsymbol{I}\boldsymbol{T}\end{bmatrix}, \boldsymbol{K_{NL}} = \begin{bmatrix}\frac{3}{4}\beta_{RR}+\frac{1}{4}\beta_{II} & \frac{1}{2}\beta_{RI}\\ \frac{1}{2}\beta_{RI} & \frac{1}{4}\beta_{RR}+\frac{3}{4}\beta_{II}\end{bmatrix}\\ \text{where } \beta^{jk} = -\left(\boldsymbol{A}^{(1)}\boldsymbol{T}\boldsymbol{w_{d_j}}\right)^T\boldsymbol{P}\left(\boldsymbol{A}^{(1)}\boldsymbol{T}\boldsymbol{w_{d_k}}\right)\boldsymbol{T}^T\boldsymbol{P}\boldsymbol{A}^{(2)}\boldsymbol{T}\end{gathered} \tag{4.15}$$

Here β^{jk} is used to denote real and imaginary parts of the displacement vector, where changing indices j and k to R and I can be used to denote real and imaginary parts respectively. While taking the integral, the integral of products method shown earlier is used. More detailed derivation can be found in Appendix B. Moreover, transformation matrix $\boldsymbol{T}$ is constructed considering simply supported boundary conditions at both ends.

Using the Galerkin method with trial functions from the linear system with simply supported boundary conditions at both ends as

$$\varphi_r(x) = \sin\left(\frac{r\pi x}{L}\right), \quad r = 1, 2, \ldots, n \tag{4.16}$$

Then, the residual vector can be obtained for a uniform excitation with magnitude F as

$$R = \left[\begin{bmatrix} \boldsymbol{K_L} & -\gamma\boldsymbol{K_L} \\ \gamma\boldsymbol{K_L} & \boldsymbol{K_L} \end{bmatrix} - \omega^2\rho A\boldsymbol{I} + \begin{bmatrix} \boldsymbol{K_{NL}} & \boldsymbol{0} \\ \boldsymbol{0} & \boldsymbol{K_{NL}} \end{bmatrix}\right] \begin{Bmatrix} \boldsymbol{w_R} \\ \boldsymbol{w_I} \end{Bmatrix} - F\boldsymbol{q} \tag{4.17}$$

where system matrices are

$$\begin{gathered} \boldsymbol{K_L} = \begin{bmatrix} \frac{EI\pi^4}{L^4}1^4 & & 0 \\ & \ddots & \\ 0 & & \frac{EI\pi^4}{L^4}n^4 \end{bmatrix}, \quad \boldsymbol{q} = \left\{\begin{matrix} \begin{Bmatrix} \frac{2L}{1\pi}(1-\cos 1\pi) \\ \vdots \\ \frac{2L}{n\pi}(1-\cos n\pi) \end{Bmatrix} \\ \boldsymbol{0} \end{matrix}\right\} \\ \boldsymbol{K_{NL}} = \frac{3EA\pi^4}{16L^4}\sum_{s=1}^{n} \begin{bmatrix} s^2 1^4\sqrt{w_{R_s}^2 + w_{I_s}^2} & & 0 \\ & \ddots & \\ 0 & & s^2 n^4\sqrt{w_{R_s}^2 + w_{I_s}^2} \end{bmatrix} \end{gathered} \tag{4.18}$$

The residual vectors obtained need to be solved numerically for each solution step, the solver uses Newton's method with arc-length continuation as explained earlier.

In the figure 4.7 the response-dependent frequency response functions (FRF) of the nonlinear system to a harmonic uniform forcing for the parameters of $E = 70\ GPa$, $\rho = 2700\ kg/m^3$, $L = 1\ m$, $h = 0.1\ m$, $b = 0.2\ m$, $\gamma = 0.1$ and $F = 400\ kN/m$, with simply supported at both end boundary conditions, using Galerkin method, Gt-DQM, transformation method and elimination method. Frequency is normalized according to $\omega_{normalized} = \omega\sqrt{\frac{\rho AL^4}{\pi^4 EI}}$, however, displacement is plotted without normalization at the final figures using a linear axis.

Note that for this figure N is used to denote the final matrix size after applying the boundary conditions since the real size used for computation is lower due to this boundary condition application.

The effect of an increased convergence rate is obvious since more points are needed to obtain very similar FRF curves as methods with slower convergence rates are used. If our method of choosing N is to stop when change does not produce any noticeable difference for the scale used in the zoom in the figure 4.7, it can be chosen $N = 3$, $N = 5$, $N = 7$, $N = 9$ for Galerkin method, GtDQM, transformation method, and elimination method, respectively. However, the $N = 1$ solution is also usable for the Galerkin method and GtDQM by looking at the original figure.

Moreover, the computational cost of extra matrix multiplications for transformation and the inner product does not produce a significant increase in run time on a single-threaded CPU usage for the increasing number of nodes N shown in the figure 4.8. This would indicate, at least for this particular case, GtDQM halves the needed time compared to the traditional elimination method to achieve similar or better convergence. Considering adaptive step-size is not used to achieve a similar number of solution points per method for each N any possible increase in speed coming from symmetric system matrices of GtDQM may not be represented here.

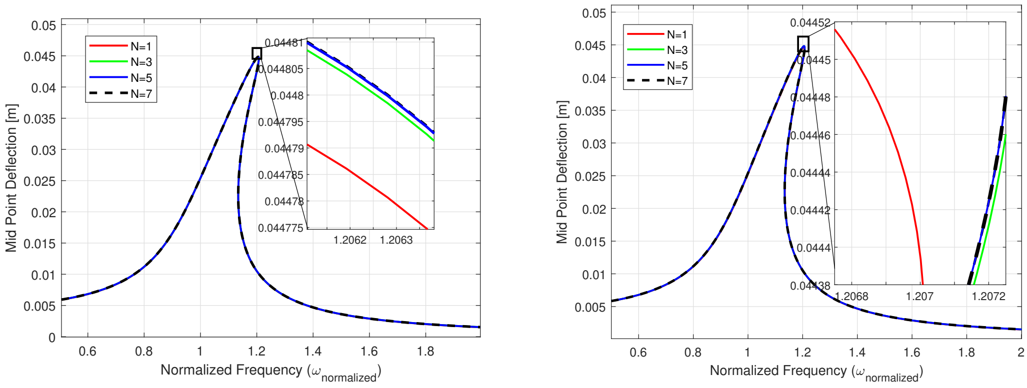

(a) Galerkin method

(b) GtDQM

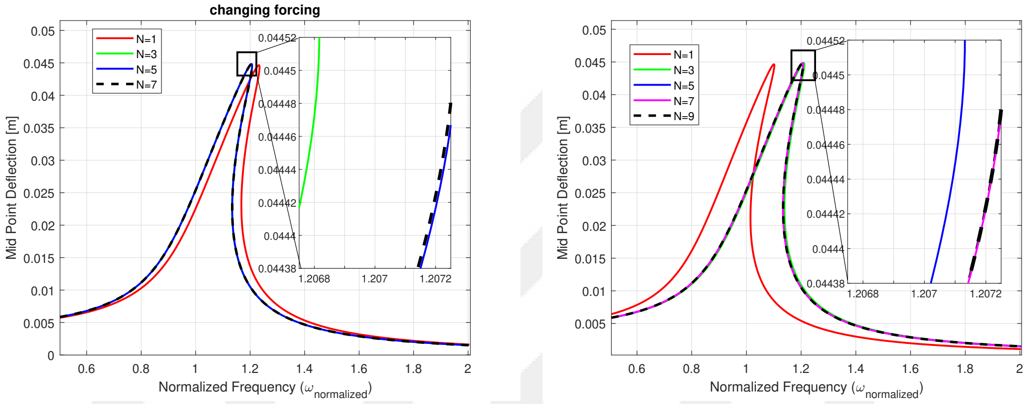

(c) Transformation method

(d) Elimination method

Figure 4.7: Frequency response functions obtained using (a) Galerkin method, (b) GtDQM, (c) Transformation method, and (d) Elimination method for different problem sizes

Another obvious take about both of these graphs is that the Galerkin method is much more efficient since trial functions are exact solutions to the linear system and orthogonal to each other, the nonlinear matrix becomes orthogonal which increases convergence rate and lowers the run-time immensely. However, this is only applicable to simple boundary conditions where the trial function can be obtained analytically, which limits its usage significantly.

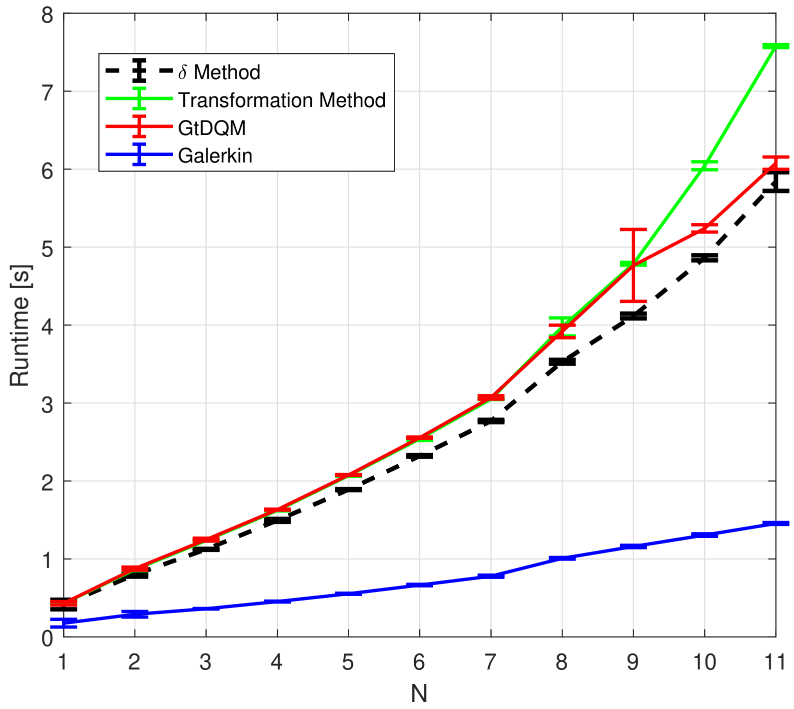

Figure 4.8: Total run-time of the solver averaged from 10 runs for each method

CHAPTER 5

FLUID CONVEYING CARBON NANOTUBES

In this section, results obtained for nonlinear fluid conveying carbon nanotubes using small-scale theories will be shown and commented upon.

Firstly, verification and convergence will be done and after being sure the method is capable of solving the problem at hand, new results will be shared that handle the nonlinearity at the frequency domain. Time domain verification will be given if applicable.

5.1 Verification

Since convergence for flow-free natural frequencies for classical elasticity theory (CET) is conducted in the earlier section in the figure 4.5 only the convergence analysis with the flow will be conducted. Since flow speed produces lots of eigenvalues and nearly no analytical data to compare, the comparison is done at the first instability speed given analytically by Païdoussis [89] as $U^*_{cr} = 2\pi$ for the non-dimensional mass ratio ($\overline{M}$) of 0.5. At that speed expected analytical eigenvalue is $0 + 0\boldsymbol{i}$ such that the comparison can directly be done with the eigenvalue itself. Table 5.1 shows the real and imaginary parts as well as the amplitude of the eigenvalue and it can clearly be seen that $N = 15$ has the lowest absolute value which also has an exact zero decay rate, furthermore absolute value slightly increases as the N increase after that point on.

Table 5.1: Real, imaginary, and absolute value of eigenvalue for different domain sizes at the $U^* = 2\pi$ for $\overline{M} = 0.5$

Total Domain Size (N)	Real part of λ	Imaginary part of λ	Absolute value of λ
5	5.501	-5.039×10^{-15}	5.501
6	4.658	-2.57×10^{-14}	4.658
7	0.4572	-2.637×10^{-15}	0.4572
8	0.4505	3.019×10^{-13}	0.4505
9	0.02213	-2.637×10^{-13}	0.02213
10	0.02212	1.103×10^{-12}	0.02212
11	0.0006461	3.769×10^{-13}	0.0006461
15	0	-6.263×10^{-6}	6.263×10^{-6}
17	0	-3.171×10^{-6}	3.171×10^{-6}
21	1.208×10^{-5}	9.294×10^{-10}	1.208×10^{-5}
25	2.302×10^{-5}	9.093×10^{-10}	2.302×10^{-5}

Similar convergence analysis can be conducted with nonlocal strain gradient theory (NSGT) with non-dimensional parameters of $\overline{M} = 05$, length scale parameter (ξ) and nonlocal parameter (α) are taken as 0.1. Since no exact data for a particular speed is missing, self-convergence will be done and further comparisons will be conducted for verification. At that speed of $U^* = 5$ each part of the eigenvalue is compared with the absolute percent relative error of the earlier domain size as given by the equation (4.10).

Table 5.2 shows the absolute percent relative change of real and imaginary parts as well as the amplitude of the eigenvalue and it can be seen that $N = 15$ still changing considerably and may not be taken as converged convincingly. $N = 17$ has much lower relative change and is better suited to be taken as converged, which is the logical continuation of the table 5.1 since NSGT has two more boundary points (due to two more boundary conditions) compared to CET, such that $N = 15$ of CET has the same system matrix size as $N = 17$ of NSGT. Henceforth, $N = 17$ will be used unless otherwise stated.

Table 5.2: Percent relative changes of real, imaginary, and absolute value of eigenvalue for different domain sizes at the $U^* = 2\pi$ for $\overline{M} = 0.5$, $\alpha = \xi = 0.1$

Total Domain Size (N)	Real part of λ	Imaginary part of λ	Absolute value of λ
8	0.1257	0.1758	0.1257
9	0.1648	0.06774	0.1648
10	0.008392	0.007286	0.008392
11	0.004202	0.003356	0.004202
15	0.001407	0.0002897	0.001407
17	4.708×10^{-6}	3.702×10^{-6}	4.708×10^{-6}
21	1.535×10^{-7}	1.942×10^{-6}	1.535×10^{-7}
25	7.553×10^{-10}	4.413×10^{-6}	7.553×10^{-10}

The first verification is to obtain the stability diagram for the first three modes with CET using clamped-clamped (CC) boundary conditions. Since only one non-dimensional parameter appears in CET which is $\overline{M}$, a stability diagram can be obtained with a single unknown. Using the data by Ni et. al. [95] where $\overline{M} = 0.5$ results can be compared and verified for CET in the figure 5.1. As expected, the first instability which is divergence (buckling) instability can be seen at around 2π, second instability which is seen around ~ 9.3 is flutter instability where the first two modes become one with the same natural frequency and same motion.

Note that, there are normally two eigenvalues for each mode with positive and negative imaginary parts, with the same real part, where only the positive imaginary part is shown. Moreover, while the system is unstable two eigenvalues appear for each imaginary value, where divergence has one imaginary part hence two real values, while flutter has two imaginary values (one positive and one negative) with accompanying four real parts, where each real part is bifurcated from the same line. Since no special solver is used such as path-following, mode numbers are ordered by, in the order of importance, looking at the closest imaginary part, looking at the closest real part, and then smallest to largest instead of the motion they are exhibiting, instead, the motion will be examined in detail in the following section.

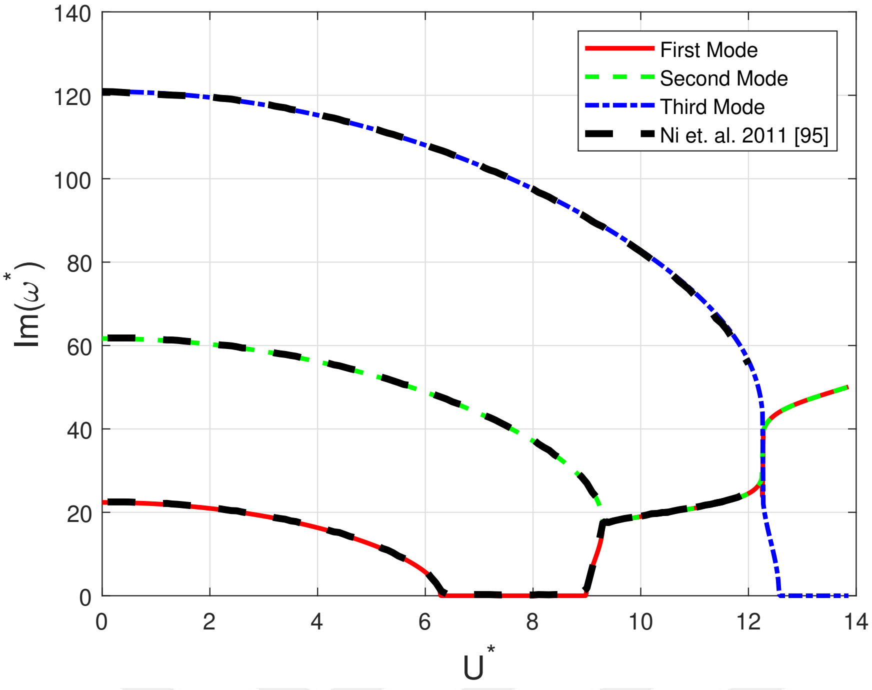

(a) Imaginary part of eigenvalue (Damped Natural Frequency)

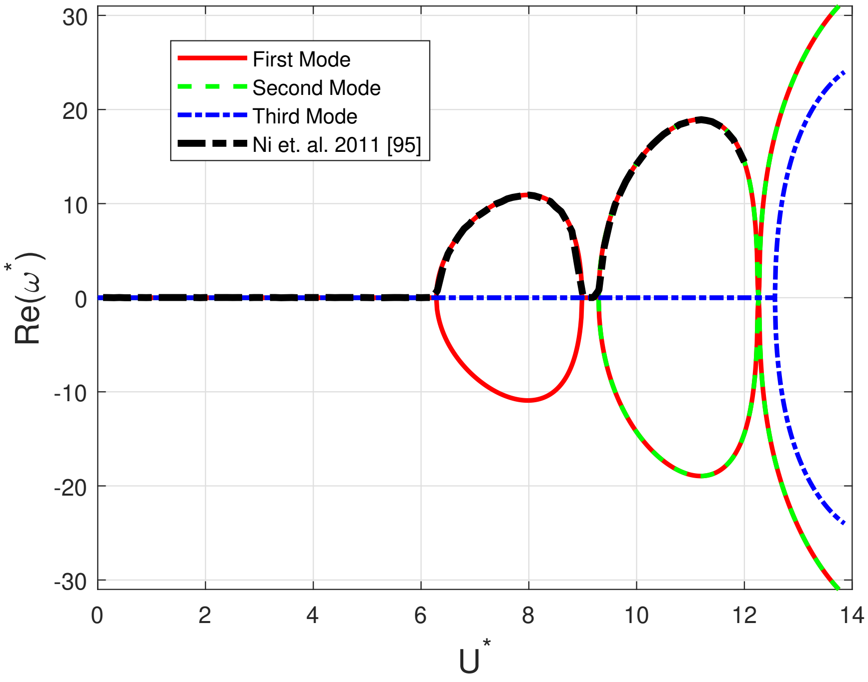

(b) Real part of the eigenvalue (Decay Rate)

Figure 5.1: Imaginary (a) and real (b) parts of eigenvalue for changing flow speed for $\overline{M} = 0.5$ using CET compared to [95]

The second method to verify is the small-scale theories, hence stability diagram of the first mode is verified only using the data produced by Atashafrooz et. al. [112] due to lack of clamped-clamped beam solution for small-scale theories. For nonlocal elasticity theory (NET) ξ is taken as zero and α is taken as 0.1, for strain gradient theory (SGT) $\xi = 0.1$ and $\alpha = 0$ is used, and for NSGT $\xi = 0.1$ and $\alpha = 0.1$ is used for comparison, in all cases classical boundary condition is CC while higher-order boundary condition is Natural boundary condition. Comparison is given in figure 5.2 again for the mass ratio of $\overline{M} = 0.5$.

As expected, there is a close match in trend especially visible for NET, however, SGT and NSGT results divert slightly from the verified solution. This can be attributed to Atashafrooz et. al. [112] using the Galerkin method to discretize the domain, even though they do not express the exact trial functions it might be assumed they are using classical Euler-Bernoulli beam mode shapes in which case fourth order boundary condition introduced by choosing natural higher-order boundary condition is not satisfied exactly but only approximately since the equation of motion has the fourth order derivative in it. It might also be due to the low quality of the given image as the figure, or misrepresentation in figures (since real and imaginary part instability points do not match when measured with a plot digitizer). In any case, results are close enough to assume correctly solved with generally used methods. Note modes are directly ordered from smallest to largest to match with the reference.

Next, the nonlinear model needs to be verified for NSGT such that after the nonlinear equation of motion and solution method is verified, it can be used to obtain new results, and those results can be somewhat verified with a time domain solution. Hence, Şimşek's [83] is used for different non-dimensional nonlocal and length-scale parameters without flow, normalized natural frequencies for different response levels are given in table 5.3 for simply-supported classical conditions for a rectangular cross-section beam (both higher-order conditions produce the same result with our assumptions). Note that the normalization is used as is used in the reference [83]. Nearly all values agree up to the five significant figures presented, considering linear interpolation is used to obtain values in between each solution point of arc-length solver, it might be considered exact. Which verifies our nonlinear method with very high precision.

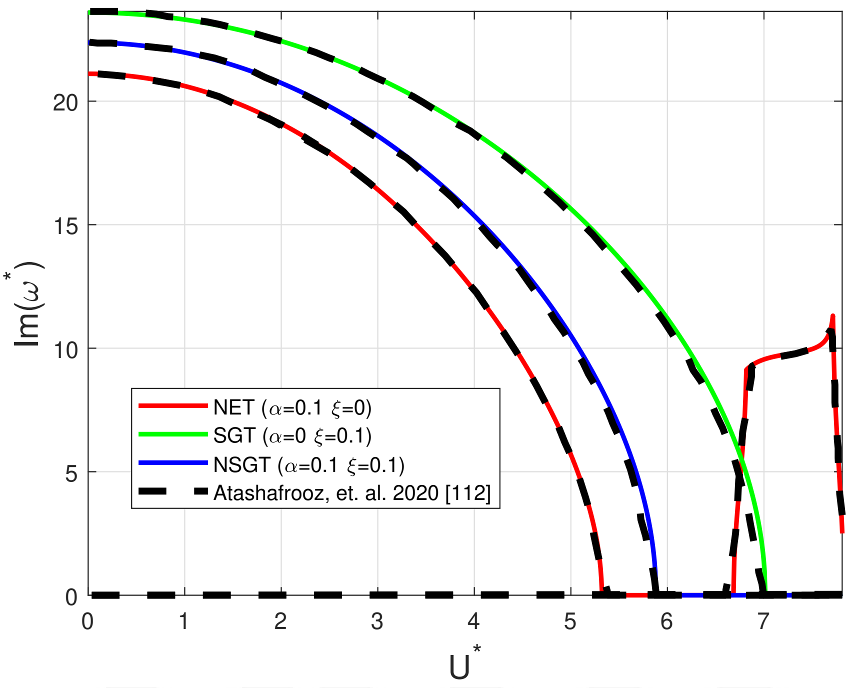

(a) Imaginary part of eigenvalue (Damped Natural Frequency)

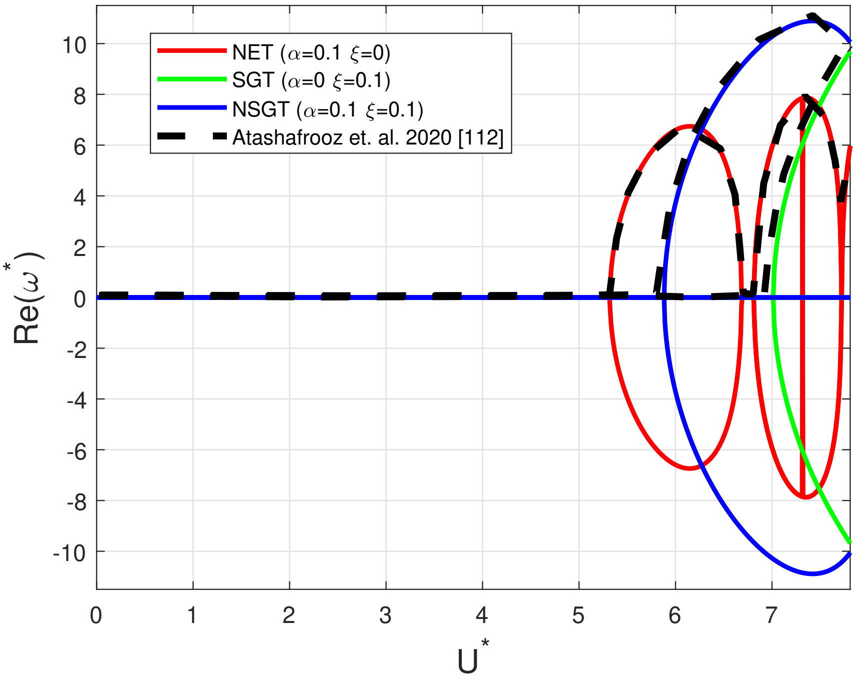

(b) Real part of the eigenvalue (Decay Rate)

Figure 5.2: Imaginary (a) and real (b) parts of eigenvalue for changing flow speed for $\overline{M} = 0.5$ using different small-scale theories compared to [112]

Table 5.3: Nonlinear normalized natural frequency ($\frac{\omega^* \sqrt{2}}{\pi^2}$) for different ξ values at $\alpha = 0.5$

Vibration Amplitude ($a = w^* \sqrt{S}$)	Arc-length results			Results from [83]		
	$\xi = 0.25$	$\xi = 0.5$	$\xi = 1$	$\xi = 0.25$	$\xi = 0.5$	$\xi = 1$
1	1.1435	1.5411	2.5777	1.1435	1.5411	2.5777
2	1.5597	1.8708	2.7874	1.5596	1.8708	2.7873
3	2.0755	2.3184	3.1056	2.0754	2.3184	3.1055
4	2.6330	2.8284	3.5028	2.6329	2.8284	3.5027
5	3.2105	3.3727	3.9553	3.2105	3.3726	3.9553

5.2 Response Dependent Stability and Natural Frequency

There are a lot of parameters to be able to be used for CNTs and there seems to be a disagreement depending on the molecular dynamics simulation method used or the production method used. For this subsection, parameters reported in [87] for single-walled CNT of armchair (5,5) configuration and given in table 5.4 will be used unless otherwise stated. Moreover, non-dimensional length scale parameters will be taken unrealistically large compared to optimization studies [78] as $\alpha = 0.4$ and $\xi = 0.2$ to be able to show the effects clearly.

Parameter	Value
Inner diameter (d_{in})	0.34 nm
Outer diameter (d_{out} or h)	1.02 nm
Thickness (t)	0.34 nm
Young's Modulus (E)	0.39 TPa
Length (L)	13.6 nm (20 d_{out})
Tube density (ρ_t)	2237 kg/m^3
Fluid density (ρ_f)	1000 kg/m^3

Table 5.4: Material and geometric properties of CNT from [87]

Firstly, the mode shapes of the CNT and modal assurance criteria (MAC) numbers will be examined to make sense of the motion of the body while vibrating or going through instability. MAC number is defined as,

$$MAC = \frac{|\boldsymbol{\psi}_1^T \boldsymbol{\psi}_2|^2}{|\boldsymbol{\psi}_1^T \boldsymbol{\psi}_1||\boldsymbol{\psi}_2^T \boldsymbol{\psi}_2|} \tag{5.1}$$

which measures the correlation between two vectors where the MAC number of 1 means exactly the same and 0 means they are orthogonal. Examining the MAC number change over the flow speed range can give insightful results.

For CC beams linear mode shapes that are normalized to have a maximum point at 1 are shown in figure 5.3 for CET, for NSGT with different high-order boundary conditions. As can be seen, the natural higher-order boundary condition produces mode shapes much closer to CET which is due to CET equation of motion approximately satisfying the natural higher-order boundary condition by equating it to mass. However, closeness does not signify physicality, on the other hand in GtDQM sixth order derivative does not become symmetric under the natural boundary condition but only for the geometric one, again physicality is questionable but it is significant to mention here.

(a) First mode shape

(b) Second mode shape

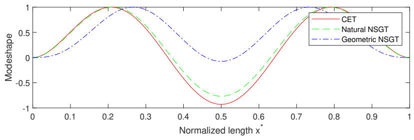

(c) Third mode shape

Figure 5.3: First three (a-c) mode shapes of clamped-clamped beam for CET, natural NSGT, geometric NSGT

For HH beams linear mode shapes that are normalized to have a maximum point at 1 are shown in figure 5.4 for CET, for NSGT with different high-order boundary conditions. As can be seen, all higher-order boundary condition produces the same mode shapes with CET, which is due to the fact that all order derivatives appearing in higher-order boundary conditions are satisfied with classical boundary conditions or equation of motion. On the contrary to CC boundary condition, all derivative matrices produced by all boundary conditions become symmetric under the GtDQM framework.

(a) First mode shape

(b) Second mode shape

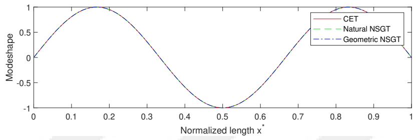

(c) Third mode shape

Figure 5.4: First three (a-c) mode shapes of hinged-hinged beam for CET, natural NSGT, geometric NSGT

Now, the motion exhibited by the tube as the tube gets more unstable as the flow speed increases can be visualized by looking at the MAC number change for each mode in the instability diagram. First, without considering the motion, real and imaginary parts of the eigenvalue can be shown in figure 5.5 for geometric higher-order boundary condition, and then the imaginary part of the accurately colored instability diagram can be shown in figure 5.6. Note that the characteristics of the diagram are very different compared to figure 5.1 since the mass ratio is more realistic which is around $\overline{M} \sim 0.05$. Such as a combination of the first two modes while the buckling is still happening and then combined motion is experiencing flutter instability.

Moreover, by looking at the figure 5.6 motion turns to the first mode shape, even in the flutter instability after a small section at the start of the flutter motion. Even after reaching and passing the third mode's frequency first vibration motion continues to dominate the flutter effect until much later, as well as the third mode turns into the first mode shape motion before experiencing its own instability of buckling. Which indicates the beam is weakest in the first mode shape.

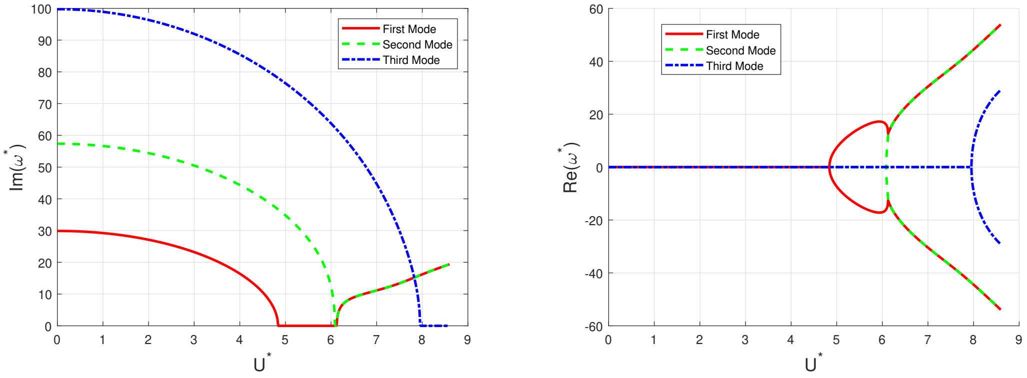

(a) First mode shape

(b) Second mode shape

Figure 5.5: Imaginary (a) and real (b) parts of eigenvalue for changing flow speed using NSGT for CC beam with geometric higher-order boundary condition

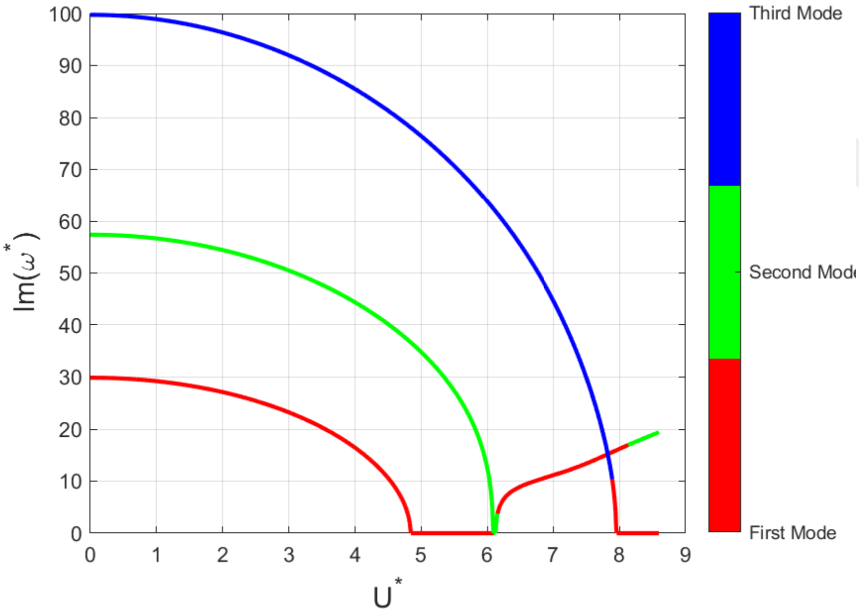

Figure 5.6: Motion characterized eigenvalues for changing flow speed using NSGT for CC beam with geometric higher-order boundary condition

Behavior can be better understood if individual MAC vectors are examined for each operating mode shape as given in the figure 5.7. The most important realization is that the first and the third mode shapes are substantially mixed with each other which might have a physical meaning concerning the higher-order boundary condition used, but could not be explained here.

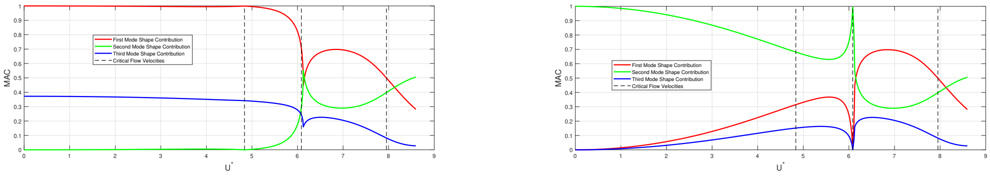

(a) First mode shape

(b) Second mode shape

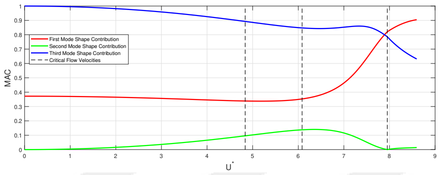

(c) Third mode shape

Figure 5.7: MAC number for the first three (a-c) for CC beam with geometric higher-order boundary condition mode shapes with flow compared to no flow mode shapes

Changing the higher-order boundary condition from geometric to natural changes the whole characteristics of instabilities which is seen in the figure 5.8. Where instead of experiencing flutter instability shortly after the second mode divergence, it occurs after the divergence of the third mode and even then coupling is between the second and the third modes. This indicates that the choice of higher-order boundary condition is a vital part of an instability analysis which increases the importance of the topic.

By further looking at the MAC vectors in figure 5.9 change of motion with changing flow speed can be seen, as the first two modes are getting closer starting after the first divergence instability third mode also changes so much so that both second and third modes couple and go through flutter in the first mode while the divergence configuration is also in the first mode shape. This again shows the importance of examining the motion characteristics instead of mode numbers. Another observation is that for this case linear mode shapes are much more orthogonal to each other compared to the geometric high-order boundary condition case.

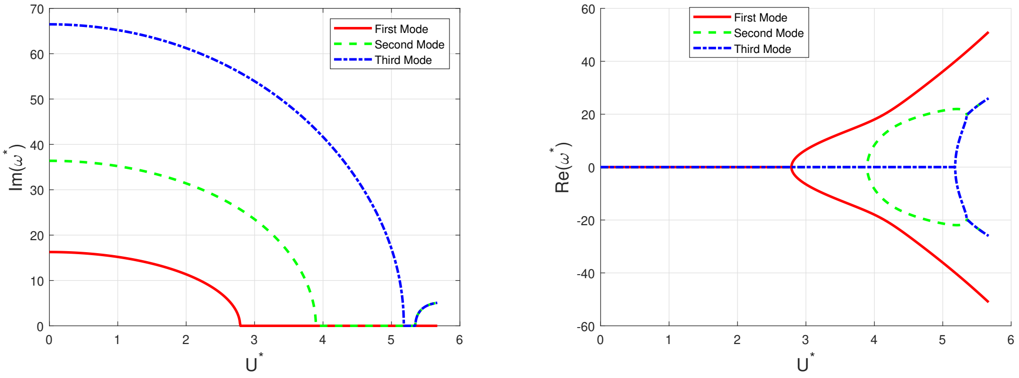

(a) First mode shape

(b) Second mode shape

Figure 5.8: Imaginary (a) and real (b) parts of eigenvalue for changing flow speed using NSGT for CC beam with natural higher-order boundary condition

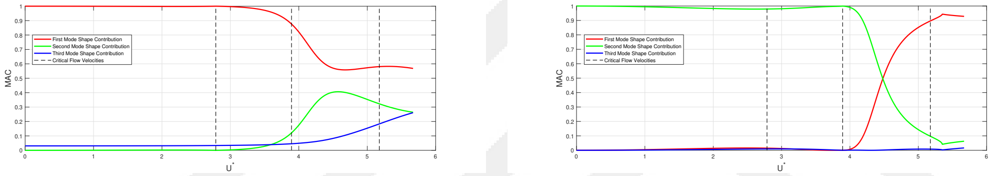

(a) First mode shape

(b) Second mode shape

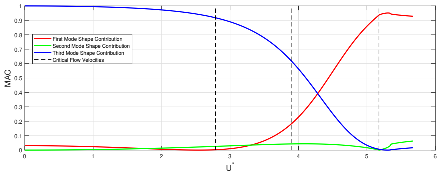

(c) Third mode shape

Figure 5.9: MAC number for the first three (a-c) mode shapes for CC beam with natural higher-order boundary condition with flow compared to no flow mode shapes

Similar results can also be shown for HH beam with either of the higher-order boundary condition since they produce the same result, however, it would not add any new observation; hence it is omitted. Instead, the effect of damping on the instabilities is shown on the HH beam with the damping ratio of $\eta = 0.01$ (or $\eta^* = 4.8 * 10^{-4}$). Real and imaginary parts of the eigenvalue are shown in figure 5.10 and motion characteristics are shown in the figure 5.11. Motion characteristics are very similar to CC beam with geometric boundary conditions which might be attributed to the fact that second-order derivative boundary conditions are the same for both.

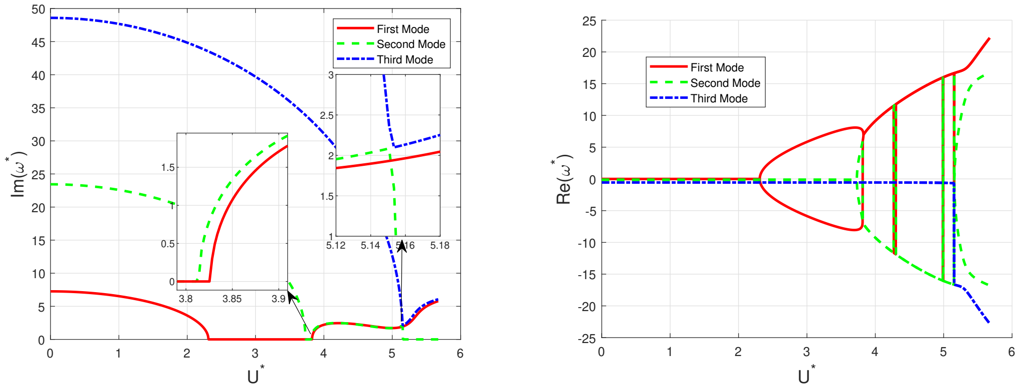

(a) First mode shape

(b) Second mode shape

Figure 5.10: Imaginary (a) and real (b) parts of eigenvalue for changing flow speed using NSGT for HH beam

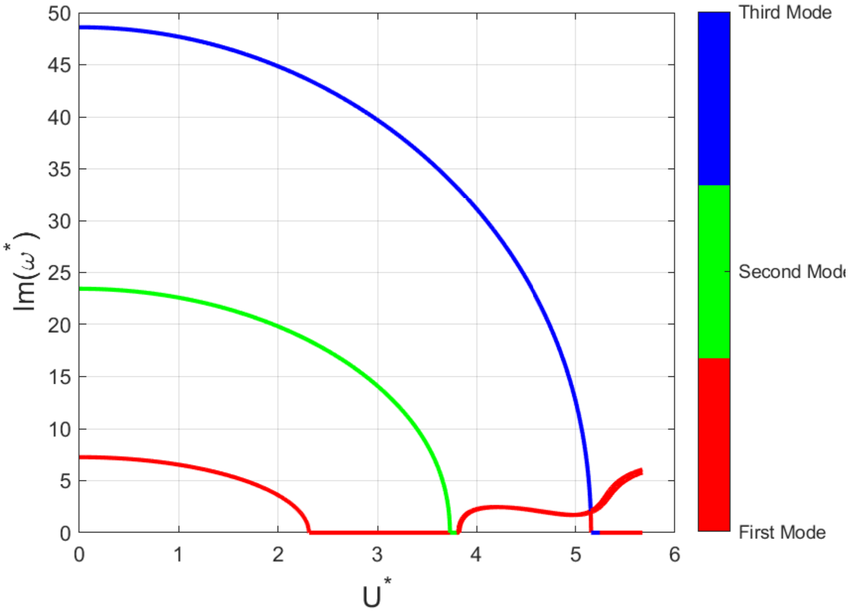

Figure 5.11: Motion characterized eigenvalues for changing flow speed using NSGT for HH beam

More importantly, the effect of damping mixes the arrangement of modes to a tangled state, it is nearly indistinguishable even by manually looking at the mode shapes and eigenvalues. For example, at the point where mode coupling occurs real parts become coupled and follow the same curves on the other hand imaginary parts are separated from each other. Or at the point where the third mode crosses coupled first and second modes, the third mode never follows the obvious trajectory downwards. These results show that a manual eigenvalue solver which follows the path of a given initial mode shape is needed for the analysis of a damped system for a better understanding of physicality.

5.3 Nonlinear results

While linear analysis is a good starting point for an instability analysis, considering instabilities are important sources of large deflections, analysis cannot be made whole without examining the nonlinear behavior. Time domain analysis is generally preferred in the literature due to ease of application, however, time constraints make it near impossible to conduct on realistic structures, hence it is very important to use a frequency domain solution.

To clearly show the effect of increasing amplitude on the system characteristics, a backbone curve can be constructed such that a change of natural frequency can be observed. Figure 5.12 shows the change of natural frequency per midpoint vibration amplitude for CC beam with both boundary conditions, which clearly shows hardening behavior for both higher-order boundary conditions. Compared to the geometric boundary condition, the increase of natural frequency is almost double for the natural boundary condition which again shows the importance of the higher-order boundary condition choice. Moreover, curves represent another important fact that even a moderate vibration of the amplitude of one height noticeably affects the vibration characteristics and must be taken into account in any stability analysis. Similarly for the HH beam, the backbone curve is shown in figure 5.13 which again shows the clear hardening behavior with higher change than both options of CC beams.

Note that, even though frequency response can easily be constructed for the natural boundary conditions, any of the ode() alternatives of Matlab could not find a solution even for relatively small time spans. Hence alternatively size of the matrices is made smaller by lowering the number of total points to $N = 11$ which only then solution achieved convergence and time domain simulation can be conducted. The exact cause of this is unknown, but likely result is that the problem with the natural boundary condition is not a self-adjoint problem even without applying GtDQM, which can be shown simply following from the equation (3.50). This might reveal insight into either higher-order boundary condition choice.

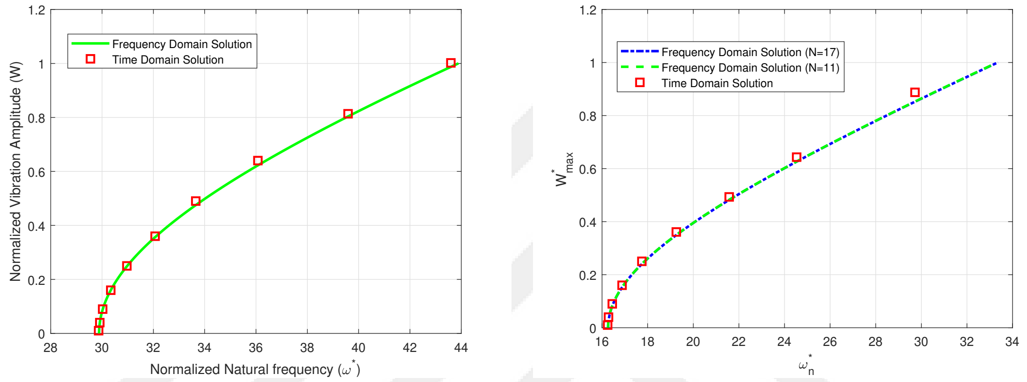

(a) Geometric higher-order boundary condition

(b) Natural higher-order boundary condition

Figure 5.12: Variation of natural frequency with changing vibration amplitude for CC beam with geometric (a) and natural (b) boundary conditions

To further analyze the nonlinear characteristics of the system time domain solution data for the last point in the figure 5.13 is used to obtain a frequency response diagram using FFT which can be seen in the figure 5.14 around the first resonance point where points at which integer multiples of the first resonance frequency are marked on the graph. This clearly shows that the even number of harmonics has no contribution, which is expected from a cubic nonlinearity introduced by the von Karman large deflection nonlinearity. Moreover, the odd harmonics die out after the third harmonic, and the third harmonic is around $1/20$ of the first, such that, it is not really a concern around the amplitude region the graph is obtained which supports the single harmonic assumption.

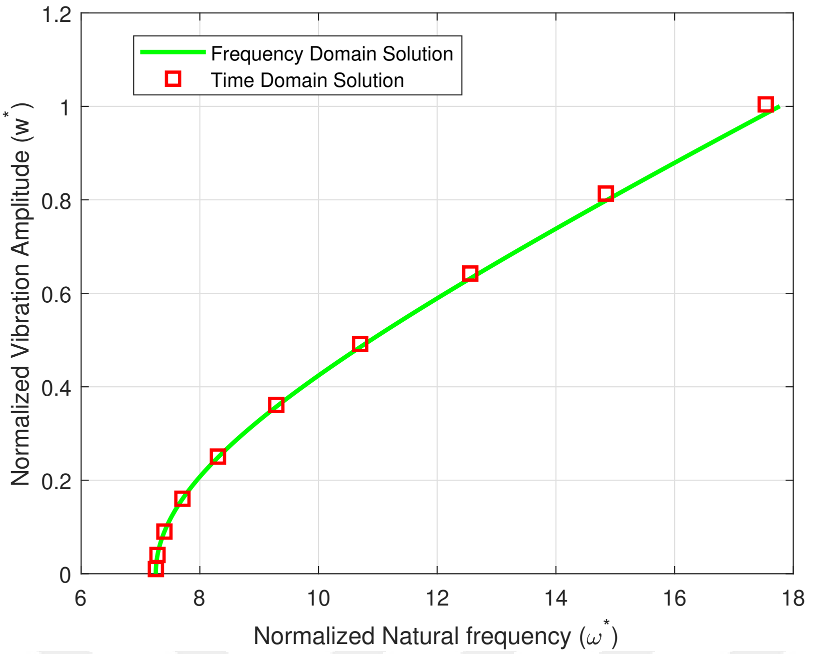

Figure 5.13: Variation of natural frequency with changing vibration amplitude for HH beam

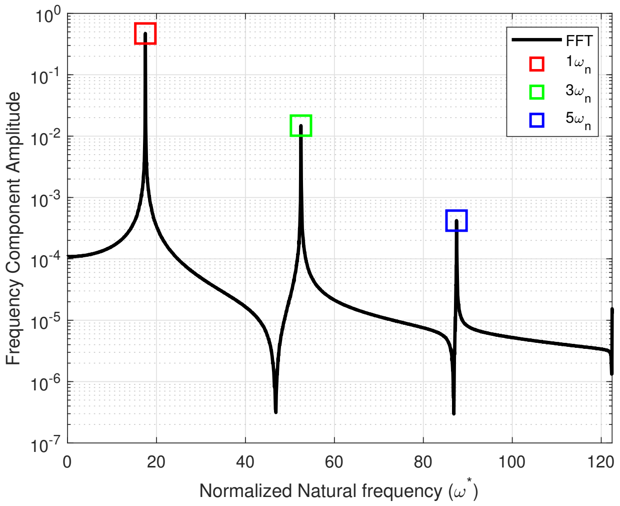

Figure 5.14: Fast Fourier Transform of the time domain data around the first resonance showing higher harmonic contributions

Hardening behavior means that even for an ideal undamped system, vibration amplitude does not reach catastrophic failure level and stays bounded on a limit at around resonance frequency. This limiting behavior can also be called limit cycle oscillation (LCO), where different starting conditions on the phase plane may converge on the same LCO line and the line determines the LCO amplitude and frequency. For fluid conveying instabilities natural consequence of the instability is to obtain a much higher vibration response which forces the system to obtain a LCO behavior and makes the instability response bounded.

To be able to obtain or approximate LCO information without using long, and expensive time domain simulations, the method explained that incorporates the pseudo-arc length continuation algorithm can be used to directly measure the critical instability speed with changing vibration amplitude. LCO amplitude variation for flow speed is shown in figure 5.15a for CC beam with geometric higher-order boundary condition obtained by the pseudo-arc-length continuation and time domain verification. For the time domain simulation, speed is increased linearly up to the specified value, and steady-state amplitude is taken afterward, and on the figure 5.15b while the curve is the same time domain simulation is done by directly using specified flow speed value from the start. Flow profiles and time domain response is examined in more detail in Appendix A.2.

Comparing the two, one can easily see that linearly increasing the speed causes divergence (buckling) type instability since the mean amplitude is similar to the maximum; while constant flow speed creates flutter instability since the mean amplitude is much smaller than the maximum amplitude, even though expected instability was divergence from looking at the figure 5.5. Such a drastic motion change can be attributed to the system experiencing instability without even getting closer to the steady-state, and sudden changes most likely creating a marginally stable orbit around the flutter instability, however, this comment needs to be taken with a grain of salt since needed elaborate time domain analysis is not conducted some amount of elaboration can be found in Appendix A.2.

Interestingly, for both cases expected LCO amplitude can be somewhat approximated by the curve obtained by the arc-length continuation. Considering the time domain verification curve for 15 points took around ~ 20 minutes while the semi-continuous curve took around ~ 5 seconds, the improvement is massive. On the other hand, an exact comparison is avoided since a much more capable and optimized time domain simulation can reduce the time substantially.

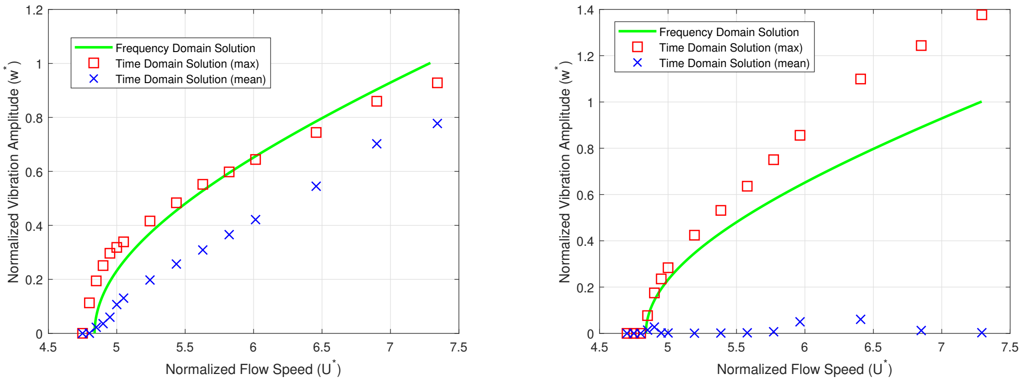

(a) Increasing Flow Speed (b) Constant Flow Speed

Figure 5.15: Variation of LCO amplitude with flow speeds for CC beam with geometric higher-order boundary condition with (a) linearly increasing and constant (b) flow speed simulations

Results for CC beam with geometric higher-order boundary condition is omitted since time domain analysis is unstable and much longer to obtain while it is not adding any new information. Instead same graphs can be seen in the figure 5.16 for the HH beam, where all observations are the same. It should be noted at this point that all of these graphs use very a small amount of damping on the order of $\eta^* \sim 10^{-5}$ such that numerical derivatives can be calculated with more accuracy and stability.

Similarly, other instability points and their motion can be analyzed by choosing the correct initial guesses for the path-following method, however, since they are not the first instability they can only be utilized just to check if they could create marginally stable solutions earlier than the first instability. Considering the hardening effects of the nonlinearity, they pose no problem and are not given here for brevity.

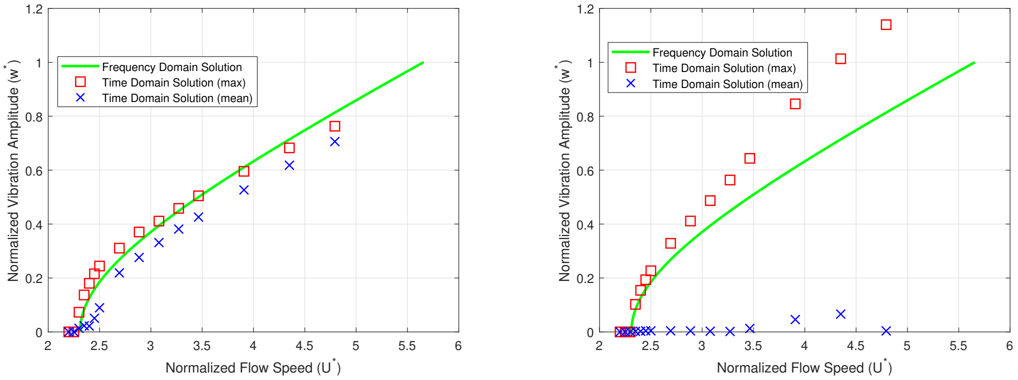

(a) Increasing Flow Speed

(b) Constant Flow Speed

Figure 5.16: Variation of LCO amplitude with flow speeds for HH beam with (a) linearly increasing and constant (b) flow speed simulations

Finally, response-dependent FRFs under harmonic uniform forcing with low damping of $\eta^* = 0.001$ ($\eta = 0.0209$) can be examined. In figure 5.17 receptance for the mid-point is shown for different levels of non-dimensional uniform forcing for CC beam with geometric higher-order boundary conditions without flow. This is verified for two forcing values in figure 5.18 using time domain simulations with initial conditions taken from the earlier solution point's mode shape. Even though, all time simulation points lie on the curve, since points are well separated on the solution curve, the solution experienced jump phenomena earlier than expected, and if a better initial deflection shape were given higher points of the FRF could be reached.

Note that, for time simulation amplitude is taken as the difference between the max and the mean after reaching steady-state, unlike earlier, since when the flow FRF is depicted buckling may occur and vibrations characteristics are captured more correctly by using the difference.

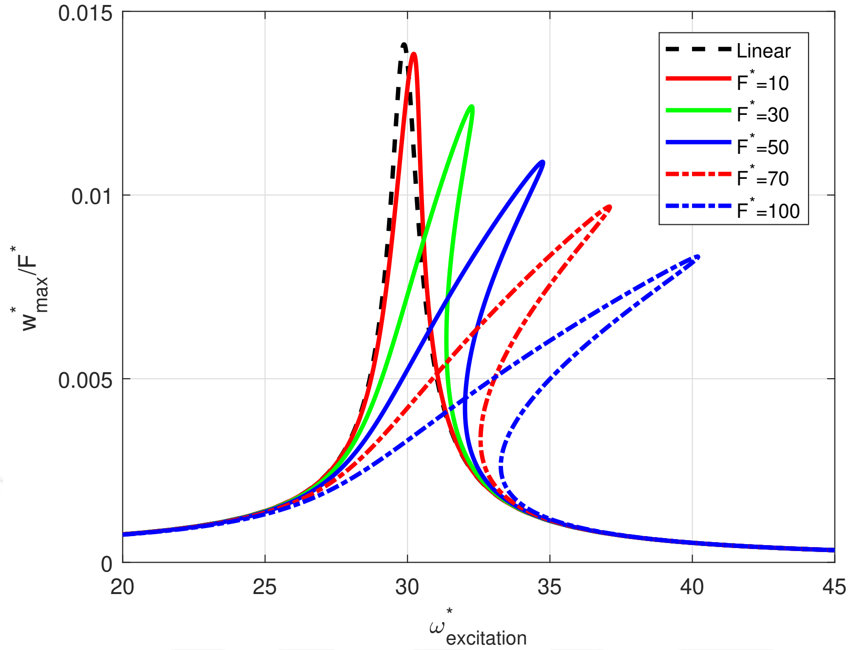

Figure 5.17: Variation of vibration amplitude for different uniform forcing for CC beam with geometric higher-order boundary condition without flow

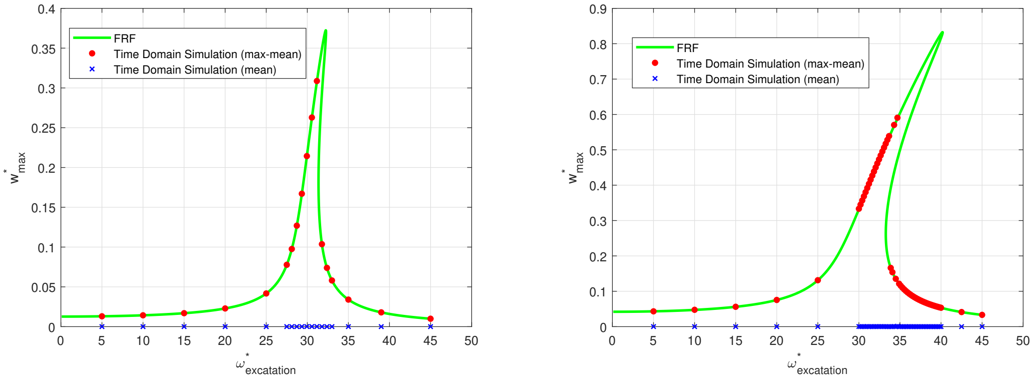

(a) $F^* = 30$

(b) $F^* = 100$

Figure 5.18: Variation of vibration amplitude for CC beam with geometric higher-order boundary condition without flow for $F^* = 30$ (a) and $F^* = 100$ (b) uniform force

Now, FRFs for CNTs conveying fluids can be examined at $F^* = 70$ for different flow speeds as given in the figure 5.19. The right-sided bend is there due to the hardening effect and as the flow speed increases the natural frequency decreases as expected while that is happening bending to the right increases substantially especially if compared with the linear frequency for that flow speed. On the other hand, peak response amplitude does not change much considering the solution gets closer to instability (even experiences it) which is interesting.

Time domain verification is given in the figure (5.20) for two different flow speeds where low flow speed verification is almost the same, higher speed starts to deviate especially for the lower frequencies. Moreover, higher peaks only fit onto the solution line after using the difference between the mean and the maximum deflection, where the mean deflection is caused by the buckling. Taking this difference does not change the results obtained earlier but corrects these results to have a good agreement with the curve, hence is used for the whole FRF analysis.

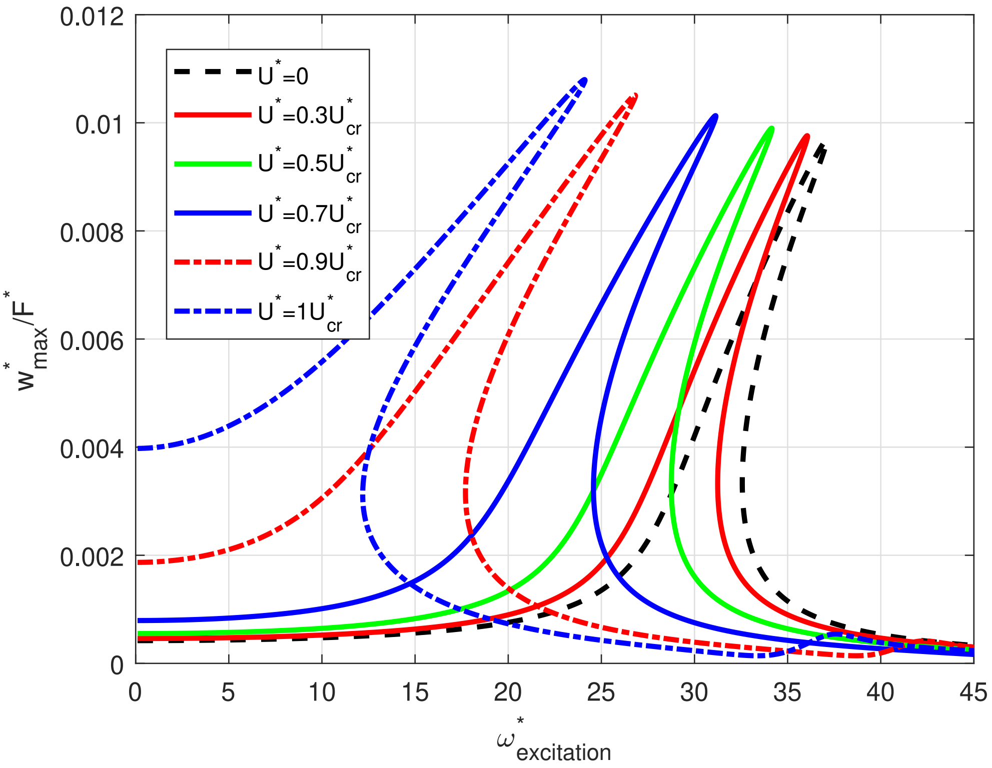

Figure 5.19: Variation of vibration amplitude for different flow speeds for CC beam with geometric higher-order boundary condition for $F^* = 70$

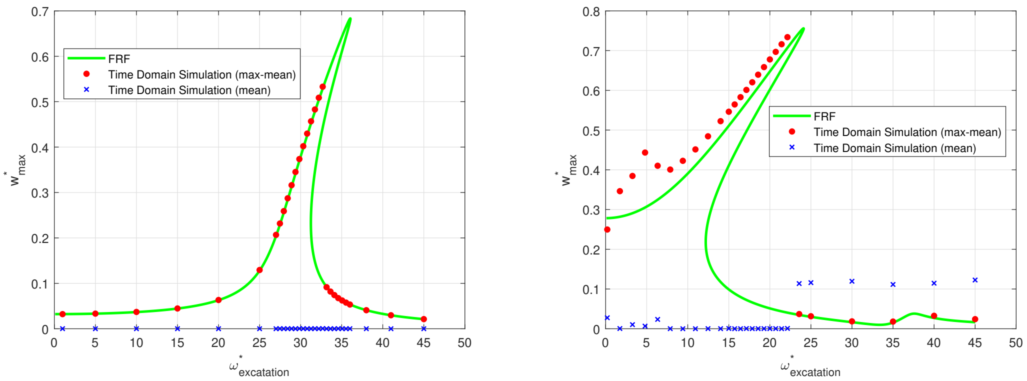

(a) $U^* = 0.3U^*_{cr}$

(b) $U^* = U^*_{cr}$

Figure 5.20: Variation of vibration amplitude for CC beam with geometric higher-order boundary condition without flow for $U^* = 0.3U^*_{cr}$ (a) and $U^* = U^*_{cr}$ (b)

To explain earlier frequencies, considering there is an obvious earlier peak before the first resonance, it points to the effect of higher harmonic contributions which can be inspected near the first peak of the time simulation using Fourier analysis. FRF of a time solution point near the first resonance obtained by FFT is given in the figure 5.21 which shows contributions of odd higher harmonics that are around $\sim 1/5$ of the first harmonic. Expected decay as the harmonic index increase is not seen much and requires the usage of many harmonics to correctly capture the motion in the time domain which is not touched upon in this thesis and the result is left as it is, considering it is satisfactory to some degree.

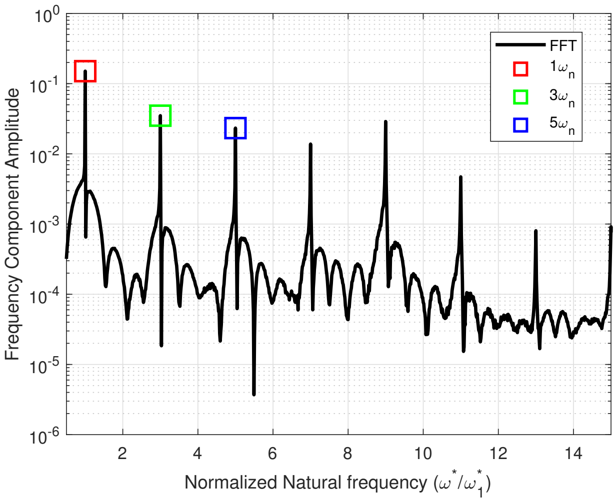

Figure 5.21: Fast Fourier Transform of the time domain data around the first resonance showing higher harmonic contributions normalized to first natural frequency of the FFT

5.4 Effect of Extra Material Parameters

In this section, results for different nonlocal and length-scale parameters are shown for completeness, since time domain verification was done earlier it is not done here. Moreover, since there were no other interesting results, only CC beam with geometric higher-order boundary conditions is used. First, the change of natural frequency with vibration amplitude (backbone curve) is shown in figure 5.22 for different nonlocal parameters with a constant length-scale parameter ($\xi = 0.2$). Softening behavior where natural frequency decreases as the nonlocal parameter increases can be clearly seen, moreover for the same deflection amplitude nonlinearity bends the backbone curve farther for the higher nonlocal parameter.

On the other hand, increasing the length-scale parameter while the nonlocal parameter is kept constant ($\alpha = 0.4$) has the opposite (hardening) effect on the natural frequency as shown in the figure (5.23), additionally lowering of the bending is not as apparent as in the nonlocal parameter. This indicates that the nonlocal parameter is more effective while examining the nonlinear effects, and can be used to better differentiate between the effect of the nonlocal parameter and length-scale parameter.

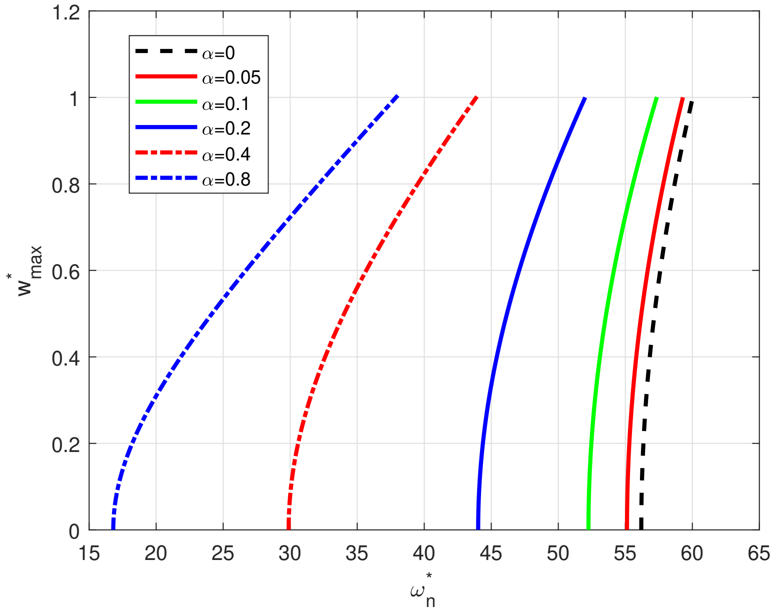

Figure 5.22: Variation of natural frequency of CC beam with geometric higher-order boundary condition for different nonlocal parameters with constant $\xi = 0.2$

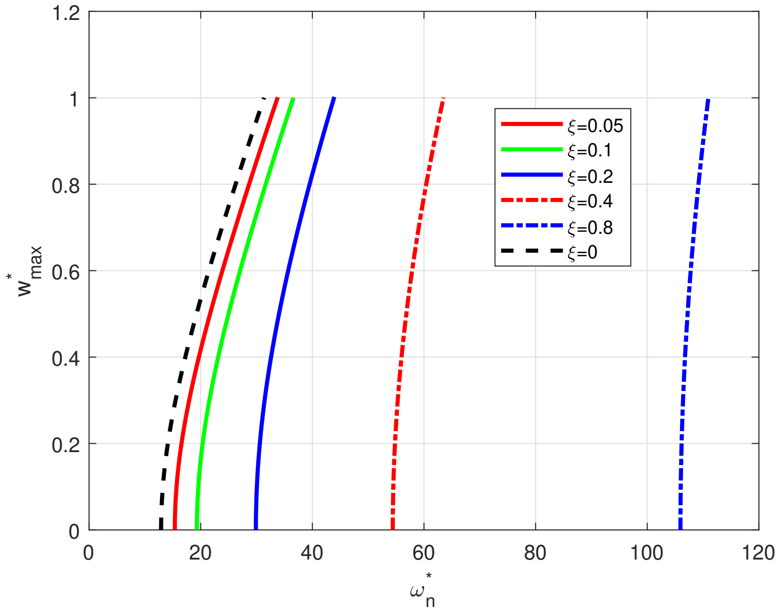

Figure 5.23: Variation of natural frequency of CC beam with geometric higher-order boundary condition for different length-scale parameters with constant $\alpha = 0.4$

The analogous effect can also be seen in the critical flow speed at different LCO amplitudes by examining the changing nonlocal parameter ($\xi = 0.2$) in the figure 5.24 where softening can be deduced from the decrease of the critical flow speed. Unlike the natural frequency changes, the change of bending is more moderate for the critical flow speed. This can be explained by regular stiffness terms of the equation of motion not being affected by the nonlocal parameter but only the mass terms, on the other hand for the critical flow speed computation stiffness terms coming from the fluid flow have a considerable effect on the total stiffness of the system, which is affected by the nonlocal parameter, hence somewhat balancing out the effects.

The same graph for different length-scale parameters with a constant nonlocal parameter ($\alpha = 0.4$) is given in the figure (5.25) where hardening behavior is almost identical to the natural frequency results. Which can again be explained by the effect of the length-scale parameter only being on the regular stiffness terms which contribute somewhat equally to the natural frequency of critical flow speed.

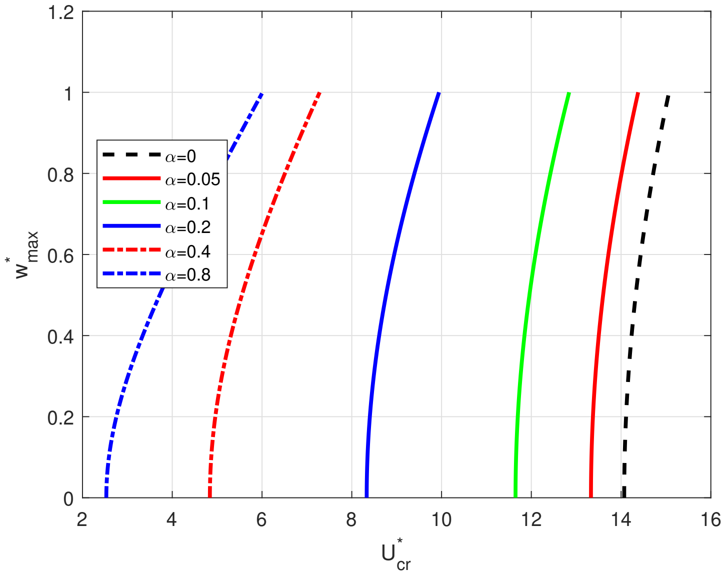

Figure 5.24: Variation of LCO amplitude with flow speeds of CC beam with geometric higher-order boundary condition for different nonlocal parameters with constant $\xi = 0.2$

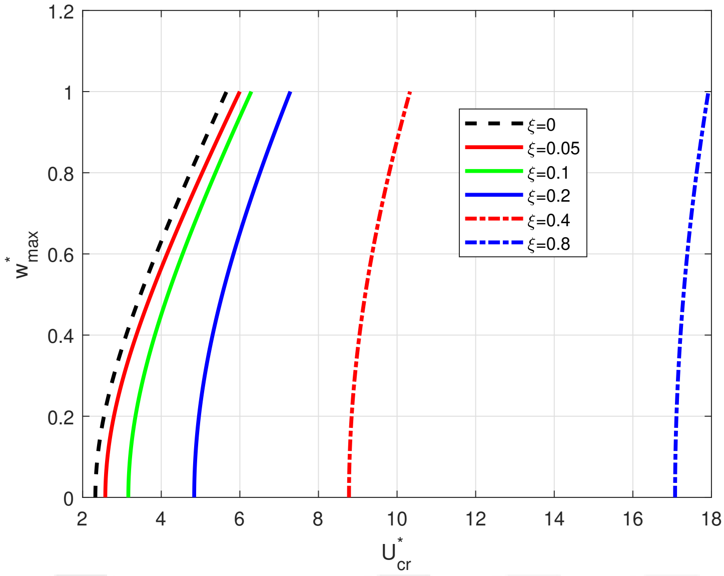

Figure 5.25: Variation of LCO amplitude with flow speeds of CC beam with geometric higher-order boundary condition for different length-scale parameters with constant $\alpha = 0.4$

Considering the path-following of the pseudo-arc-length continuation method can be used to follow the critical flow velocity for different vibration amplitudes, a similar method can be employed to follow a defined parameter (such as the nonlocal parameter) between two values. This can be achieved by predetermining the parameter such as vibration amplitude as if it is a constant force amplitude for the case of FRFs, and an extra equation can be used to fix the small-length parameter. Which increases the speed at which the critical speed against changing material parameters considerably.

The approximate procedure for such a graph is to solve the state space eigenvalue problem with increasing flow speeds until the real part becomes positive, this is repeated for each discrete point of the parameter and stored to be plotted later. However, with this method only the state space eigenvalue is solved for the initial guess, and then the length-scale parameter is automatically changed with the explained procedure such that it obtains a curve that solves the problem at hand for different values. The first procedure has not been tried due to low accuracy and long computation time but only the second procedure is done.

The figure 5.26a shows the linear critical flow velocity change for changing the nonlocal parameter for multiple length-scale parameters, while the figure 5.26b shows the linear critical flow velocity change for changing length-scale parameters for multiple nonlocal parameters. Effects of both parameters can somewhat be seen simultaneously as if it is a projection of the surface composed of two length scale parameters and critical flow velocity.

This can also be expanded by changing the prescribed deflection as if changing the forcing while constructing the FRF such that not only the linear case can be handled but the nonlinear result for a vibration amplitude can also be obtained. Which can be used to determine the actual critical flow speed if the prescribed deflection is the maximum allowable deflection of the design.

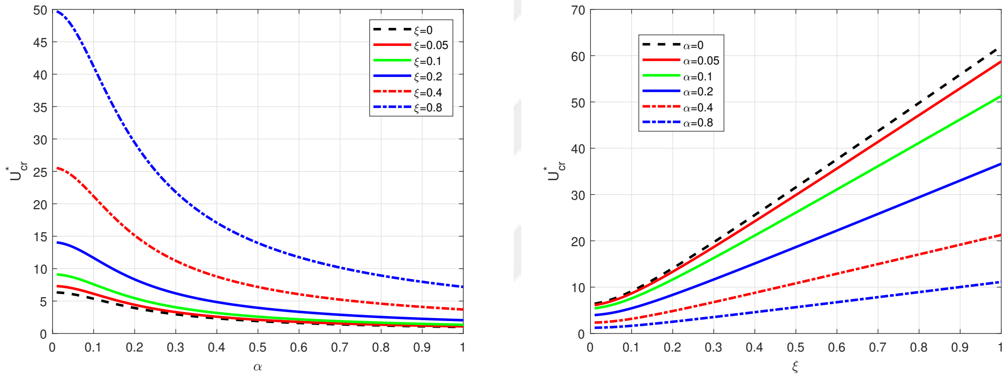

(a) Changing α with different constant ξ

(b) Changing ξ with different constant α

Figure 5.26: Variation of linear critical flow speed of CC beam with geometric higher-order boundary condition for changing nonlocal parameters with different constant ξ (a) and changing length-scale parameters with different constant α (b)

The figure 5.27a show the effect of nonlocal parameter change for constant $\xi = 0.2$ value for different vibration amplitudes and similarly the figure 5.27b shows the effect of length-scale parameter change for constant $\alpha = 0.4$ value for different vibration amplitudes.

Note that, this method can be used to create an approximate surface to better determine the initial conditions for an optimization algorithm. Or even can be used to include geometric parameters and can be used as a reference figure for faster design.

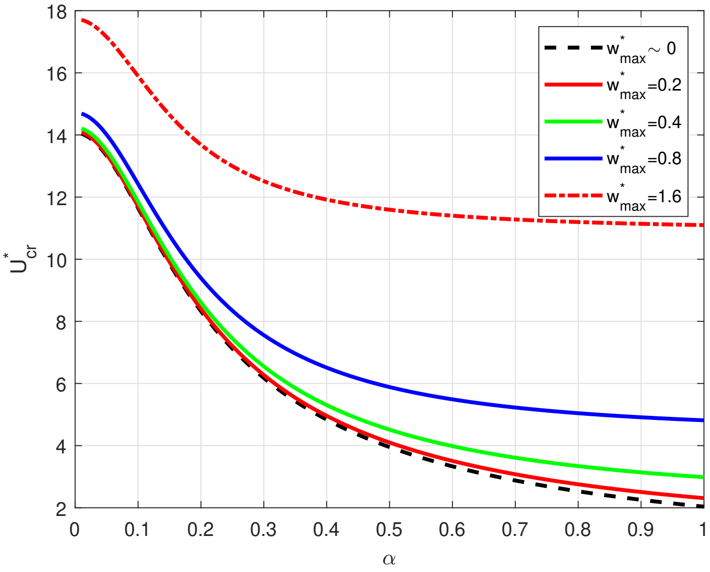

(a) Changing α with constant $\xi = 0.2$

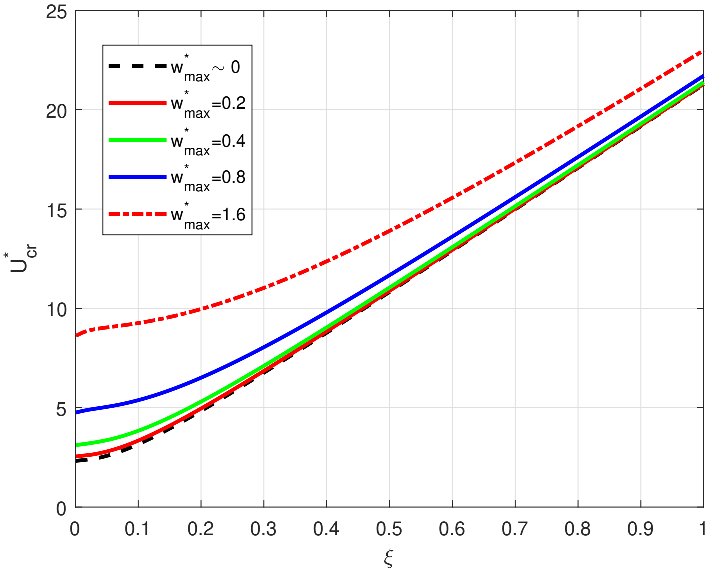

(b) Changing ξ with constant $\alpha = 0.4$

Figure 5.27: Variation of critical flow speed of CC beam with geometric higher-order boundary condition for changing nonlocal parameters with constant $\xi = 0.2$ (a) and changing length-scale parameters with constant $\alpha = 0.4$ (b) for different LCO amplitudes

CHAPTER 6

CONCLUSIONS

6.1 Summary and Discussion

In this thesis, nonlinear vibrations of the fluid conveying carbon nanotubes are examined including the small-scale effects. The equation of motion of the tube is obtained as an equivalent beam model with Euler-Bernoulli kinematic assumptions, and large deflection effects are taken into account by using Green-Lagrange strain tensor with von-Karman assumptions. Fluid-structure interaction is modeled as an equivalent uniform flow with the same mass flow rate, even though several corrections to the model are mentioned, non is applied since they do not change the main characteristics of the interaction.

The novel method of Galerkin transformed DQM (GtDQM) is used for spatial discretization of the equation of motion. Unlike Generalized DQM, GtDQM uses coordinate transformation with the information coming from the boundary condition equations to incorporate general boundary conditions into the equation of motion. The method is then further enhanced by applying the Galerkin procedure which makes the resulting system matrices symmetric, which substantially increases the stability and convergence rate of the method. Claims of higher convergence rate, more stable solutions, and faster results are shown with different types of boundary conditions and kinematic beam assumptions.

After spatial discretization, instabilities are examined in the linear regime using the state space eigenvalue problem. Motion of the tube before, during, and after instabilities are determined with modal assurance criteria comparison, hence motion during the instability is presented. Further nonlinear instability analysis is conducted using the harmonic balance method for temporal discretization. Resulting nonlinear algebraic equations are solved with pseudo-arc-length continuation with Newton's method by adding different additional equations to incorporate other unknowns like critical flow speed, or material parameters. These frequency domain solutions are somewhat verified with time domain simulations.

Using frequency domain analysis response amplitude-dependent nonlinear natural frequencies, nonlinear critical speeds, and frequency response functions are obtained for different boundary conditions or small-scale parameters. Those results suggest that nonlinear analysis is essential while examining the instabilities of the fluid conveying carbon nanotube which can theoretically be extended to other type of instabilities. Due to speed, accuracy, and much lower computational cost frequency domain analysis is also strongly suggested.

Finally, the effect of changing small-scale parameters on the vibration and/or instability characteristics is examined. As expected, the obvious softening effect of the nonlocal parameter and hardening effect of the length-scale parameter is observed and the relative importance of the nonlocal parameter compared to the length-scale parameter on nonlinear analysis is noted.

6.2 Future Work

Possible future work is abundant since the numerical discretization method and the nonlinear solution methodology is new. Even the small-scale elasticity theories can be considered relatively new since classical elasticity theory has existed for centuries. Hence, future work will be mentioned for different methods or theories one by one.

First, future work for elasticity theories is examined starting from strain gradient theory:

- The mass terms are corrected by the effects of micro velocity (velocity gradient) as given by Mindlin [38], however, the same correction is missing from the modified strain gradient theory since Lam et. al. [32] derived it for static analysis and the kinetic energy is written as the classical kinetic energy afterward. The origin of the classical kinetic energy usage is not found, however, the most likely scenario is that it is used since it is easier without much thought. The importance of this missing correction can be better understood if the wave dispersion equation of motion can be directly written from [38] as,

$$(1 - l_1\nabla^2)\nabla^2\boldsymbol{\nabla}\cdot\boldsymbol{u} = (1 - h_1\nabla^2)\boldsymbol{\nabla}\ddot{\boldsymbol{u}} \tag{6.1}$$

where u is the displacement, and $\boldsymbol{\nabla}$ is the divergence operator. This equation is of the same form as the NSGT which can be obtained without considering nonlocal effects and a more rigorous mathematical background. It may be that this mass correction is not being used because it might have been disproved, however, it still is an important improvement to the current theories.

- In the strain gradient theory, one of the most important unsolved problem is which higher-order boundary condition to be used, and as shown in this thesis it does change the answer substantially. Hence it can be studied in different ways, such as by mathematical proof (as encountered in the thesis some higher-order boundary conditions do not make the derivative matrix symmetric even though they should), or by taking the choice of boundary condition as an extra parameter while fitting the results of molecular dynamic simulations or experimental measurements to the elasticity theory to determine small-scale parameters as is done in [77].

- Another direction that can be researched is the viability of negative small-scale parameter and their physical meaning. Even though, those parameters are taken to be positive to ensure positive definiteness of the strain energy in [32, 40], Mindlin's original work [36, 38, 39] clearly shows only a combination of parameters needs to be positive to ensure the positive definiteness of the strain energy.

For the nonlocal elasticity theory, the main problem is that the kernel and the linear differential operator forms produce different solutions, which is not surprising considering the given linear differential operator is only Green's function for specific two-dimensional kernel as given by Eringen [63]. Hence extension of the kernel to the one or three-dimensional problems would naturally produce results not conferring to each other. However, since integral formulation needs iterative solutions and lacks explicit formulation it is not preferred. This problem can in possibility be mended either by iteratively using the found analytical solution in the integral calculation and finding an analytical form that approximates integral starting from the easier differential form or by using an approximate assumed displacement form that can be directly used to obtain approximate constitutive relation. Considering if the correction for strain gradient theory is realized, nonlocal effects are not needed to explain behavior, this future work direction may not be optional.

If the given strain gradient correction cannot be realized, currently only choice of combining the effects of strain gradients and nonlocal constitutive relations is the nonlocal strain gradient theory (NSGT). If NSGT must be used, then there must be some strengthening of the mathematical foundation is needed as listed below,

- Considering only some parts of the second-order deformation tensor with a single length scale parameter is a gross simplification since at least three independent parameters are needed mathematically. At the very least, modified couple stress theory can be used to capture strain derivative effects with a single length scale parameter that is more mathematically sound.
- A better method would be to include all three extra parameters of SGT and by using the similar assumptions of the same kernel and the same nonlocal parameter for all stress components similar derivation can be followed. Which formulates a total of 4 extra small-scale parameters that can account for different results from experiments or simulations.
- Even if the kernel function and nonlocal parameter can be assumed to be the same, still NSGT uses a one-dimensional formulation that is yet to be extended to higher dimensions and the used kernel is not applicable as explained earlier, hence the convolution integral needs to be better accounted for.

Secondly, improvements can be made to the assumptions, which are:

- Axial inertia is neglected completely to reduce two displacement unknowns to one, however, this assumption that is generally made for large deflection beams may not be applicable since axial inertia also includes much more dominant fluid flow. By using two displacement unknowns differences can be better seen and if needed can be preferred.

- As noted in the last FRF result, even if the critical flow speed change can be captured with a single harmonic solution, to determine the forcing response more accurately near the critical flow regime the multi-harmonic balance needs to be used. This is necessary if the unstable region needs to be utilized in the design process such as quasi-zero stiffness.
- Similarly, kinematic assumptions might fail for the large rotations encountered for the buckled configuration, as well as the general shape needs to be accounted for if the buckled configuration will be used as a design point.
- If the flow speed is not normalized and critical flow speed is obtained in SI units it roughly corresponds to be around $\sim 7km/s$ (for $U^*_{cr} = 2\pi$), which compared with the speed of sound of the water (density chosen) that is around $\sim 1.5km/s$ either critical flow speed cannot be reached without going supercritical or much more sophisticated transonic flow theories needs to be used. This is not considered in the literature as far as the author can conclude which is an important oversight.
- Since the method developed already requires iterative solutions, a simplified Navier-Stokes equation can also be incorporated to have a much more representative fluid-structure interaction. These methods are somewhat tried in [93,94], however, nonlinearity is not handled correctly.

Finally, improvements and research directions for the novel method of GtDQM and examined,

- Extension of the given method to two dimensions is not straightforward and needs to be handled as a special case even though it is not very complicated. Hence two or three dimension extension of the given method is needed for general use in those areas.
- Even though it is used to solve a mostly structural problem it can also be used

to obtain possible better results for the original usage case of fluid dynamics problems and such can be used in those areas as well.

- A generalized boundary matching algorithm can be devised to include concentrated forces and more complicated domains. With the algorithm at hand, it can also be extended as a finite element analysis procedure either on its own or to be used to obtain a beam or a brick elements.
- Not directly the GtDQM, but the up-scaling matrix and integral matrix if computed once at the initialization phase can easily be used to compute integrals of multi harmonic balance method much faster. Similarly can be used as the predictor it can be used as the predictor that approximates the Jacobian prediction without high computational costs.
- Extension of the one-dimensional method can also be used as a time domain integration procedure.

Some of those improvements and future work are currently being researched by the author, due to the wide range of topics from theoretical to numerical methods, or structural to fluid dynamic fields it is impossible to cover all the areas mentioned. Hence, collaborative work needs to be done to touch upon all the mentioned possible future work.

REFERENCES

[1] S. Iijima, "Helical microtubules of graphitic carbon," *Nature*, vol. 354, pp. 56–58, 1991.

[2] T. Ebbesen, *Carbon Nanotubes: Preperation and Properties*. Taylor & Francis, 1996.

[3] R. S. Ruoff, D. Qian, and W. K. Liu, "Mechanical properties of carbon nanotubes: theoretical predictions and experimental measurements," *Comptes Rendus Physique*, vol. 4, no. 9, pp. 993–1008, 2003.

[4] S. Erkoç and O. B. Malcıoğlu, "Structural properties of carbon nanorods: Molecular-dynamics simulations," *International Journal of Modern Physics C*, vol. 13, no. 03, pp. 367–373, 2002.

[5] S. Govindjee and J. L. Sackman, "On the use of continuum mechanics to estimate the properties of nanotubes," *Solid State Communications*, vol. 110, no. 4, pp. 227–230, 1999.

[6] H. Cho, M.-F. Yu, A. F. Vakakis, L. A. Bergman, and D. M. McFarland, "Tunable, broadband nonlinear nanomechanical resonator," *Nano Letters*, vol. 10, no. 5, pp. 1793–1798, 2010.

[7] X. Cai and L. Xu, "Control of vibration nonlinearity and quality factor for a carbon nanotube mass sensor," *Nonlinear Dyn*, vol. 111, p. 6179–6197, 2023.

[8] V. Naresh and N. Lee, "A review on biosensors and recent development of nanostructured materials-enabled biosensors," *Sensors*, vol. 21, no. 4, 2021.

[9] C. Shu and B. E. Richards, "Application of generalized differential quadrature to solve two-dimensional incompressible navier-stokes equations," *International Journal for Numerical Methods in Fluids*, vol. 15, no. 7, pp. 791–798, 1992.

[10] R. Bellman and J. Casti, “Differential quadrature and long-term integration,” *Journal of Mathematical Analysis and Applications*, vol. 34, no. 2, pp. 235–238, 1971.

[11] H. Du, M. K. Lim, and R. M. Lin, “Application of generalized differential quadrature method to structural problems,” *International Journal for Numerical Methods in Engineering*, vol. 37, no. 11, pp. 1881–1896, 1994.

[12] C. Shu, *Generalized differential-integral quadrature and application to the simulation of incompressible viscous flows including parallel computation*. PhD thesis, University of Glasgow, 1991.

[13] R. Aghazadeh, E. Cigeroglu, and S. Dag, “Static and free vibration analyses of small-scale functionally graded beams possessing a variable length scale parameter using different beam theories,” *European Journal of Mechanics - A/Solids*, vol. 46, pp. 1–11, 2014.

[14] L.-L. Ke, Y.-S. Wang, J. Yang, and S. Kitipornchai, “Nonlinear free vibration of size-dependent functionally graded microbeams,” *International Journal of Engineering Science*, vol. 50, no. 1, pp. 256–267, 2012.

[15] Z. A. Siddiqi and A. R. Kukreti, “Analysis of eccentrically stiffened plates with mixed boundary conditions using differential quadrature method,” *Applied Mathematical Modelling*, vol. 22, no. 4, pp. 251–275, 1998.

[16] E. Cigeroglu and H. Samandari, “Nonlinear free vibrations of curved double walled carbon nanotubes using differential quadrature method,” *Physica E: Low-dimensional Systems and Nanostructures*, vol. 64, pp. 95–105, 2014.

[17] M. Qasim, M. Afridi, A. Wakif, and S. Saleem, “Influence of variable transport properties on nonlinear radioactive jeffrey fluid flow over a disk: Utilization of generalized differential quadrature method,” *Arabian Journal for Science and Engineering*, vol. 44, pp. 5987–5996, 2019.

[18] C. Shu and K. Wee, “Numerical simulation of natural convection in a square cavity by simple-generalized differential quadrature method,” *Computers & Fluids*, vol. 31, pp. 209–226, 2002.

[19] A. Korkmaz and I. Dağ, “A differential quadrature algorithm for nonlinear schrödinger equation,” *Nonlinear Dyn*, vol. 56, p. 69–83, 2019.

[20] R. Mokhtari, A. S. Toodar, and N. G. Chegini, “Application of the generalized differential quadrature method in solving burgers’ equations,” *Communications in Theoretical Physics*, vol. 56, p. 1009, dec 2011.

[21] R. Mokhtari, A. S. Toodar, and N. G. Chegini, “Numerical simulation of coupled nonlinear schrödinger equations using the generalized differential quadrature method,” *Chinese Physics Letters*, vol. 28, p. 020202, feb 2011.

[22] M. Malik and C. W. Bert, “Implementing multiple boundary conditions in the dq solution of higher-order pdes: Application to free vibration of plates,” *International Journal for Numerical Methods in Engineering*, vol. 39, no. 7, pp. 1237–1258, 1996.

[23] X. Wang and C. W. Bert, “A new approach in applying differential quadrature to static and free vibrational analyses of beams and plates,” *Journal of Sound and Vibration*, vol. 162, pp. 566–572, 1993.

[24] X. Wang, C. Bert, and A. Striz, “Differential quadrature analysis of deflection, buckling, and free vibration of beams and rectangular plates,” *Computers & Structures*, vol. 48, no. 3, pp. 473–479, 1993.

[25] C. Shu and H. Du, “A generalized approach for implementing general boundary conditions in the gdq free vibration analysis of plates,” *International Journal of Solids and Structures*, vol. 34, no. 7, pp. 837–846, 1997.

[26] Y. X. C. W. NG, Y. Zhao and G. Wei, “On the accuracy and stability of a variety of differential quadrature formulations for thevibration analysis of beams,” *International Journal of Engineering and Applied Sciences*, vol. 1, 2009.

[27] A. G. Striz, C. Weilong, and C. W. Bert, “Static analysis of structures by the quadrature element method (qem),” *International Journal of Solids and Structures*, vol. 31, no. 20, pp. 2807–2818, 1994.

[28] X. Wang and H. Gu, “Static analysis of frame structures by the differential quadrature element method,” *International Journal for Numerical Methods in Engineering*, vol. 40, pp. 759–772, 1997.

[29] S. Eftekhari, "A simple and systematic approach for implementing boundary conditions in the differential quadrature free and forced vibration analysis of beams and rectangular plates," *Journal of Solid Mechanics*, vol. 7, no. 4, pp. 374–399, 2015.

[30] M. Keleshteri and J. Jelovica, "Beam theory reformulation to implement various boundary conditions for generalized differential quadrature method," *Engineering Structures*, vol. 252, p. 113666, 2022.

[31] B. A. Finlayson and L. E. Scriven, "The method of weighted residuals – a review," *Appl. Mech. Rev.*, vol. 19, no. 9, pp. 735–748, 1966.

[32] D. Lam, F. Yang, A. Chong, J. Wang, and P. Tong, "Experiments and theory in strain gradient elasticity," *Journal of the Mechanics and Physics of Solids*, vol. 51, no. 8, pp. 1477–1508, 2003.

[33] R. Ansari, H. Rouhi, and S. Sahmani, "Calibration of the analytical nonlocal shell model for vibrations of double-walled carbon nanotubes with arbitrary boundary conditions using molecular dynamics," *International Journal of Mechanical Sciences*, vol. 53, no. 9, pp. 786–792, 2011.

[34] R. Ansari, S. Ajori, and B. Arash, "Vibrations of single- and double-walled carbon nanotubes with layerwise boundary conditions: A molecular dynamics study," *Current Applied Physics*, vol. 12, no. 3, pp. 707–711, 2012.

[35] R. Ansari and S. Ajori, "A molecular dynamics study on the vibration of carbon and boron nitride double-walled hybrid nanotubes," *Appl. Phys. A*, vol. 120, no. 3, p. 1399–1406, 2015.

[36] R. Mindlin and H. Tiersten, "Effects of couple-stresses in linear elasticity.," *Arch. Rational Mech. Anal.*, vol. 11, p. 415–448, 1962.

[37] R. Toupin, "Elastic materials with couple-stresses," *Arch. Rational Mech. Anal.*, vol. 11, p. 385–414, 1964.

[38] R. Mindlin, "Micro-structure in linear elasticity," *Arch. Rational Mech. Anal.*, vol. 16, p. 51–78, 1964.

[39] R. Mindlin, “Second gradient of strain and surface-tension in linear elasticity,” *International Journal of Solids and Structures*, vol. 1, no. 4, pp. 417–438, 1965.

[40] N. A. Fleck and J. W. Hutchinson, “Strain gradient plasticity,” *Advances in Applied Mechanics*, vol. 33, pp. 295–361, 1997.

[41] N. Fleck and J. Hutchinson, “A reformulation of strain gradient plasticity,” *Journal of the Mechanics and Physics of Solids*, vol. 49, no. 10, pp. 2245–2271, 2001.

[42] F. Yang, A. Chong, D. Lam, and P. Tong, “Couple stress based strain gradient theory for elasticity,” *International Journal of Solids and Structures*, vol. 39, no. 10, pp. 2731–2743, 2002.

[43] S. Kong, S. Zhou, Z. Nie, and K. Wang, “The size-dependent natural frequency of bernoulli–euler micro-beams,” *International Journal of Engineering Science*, vol. 46, no. 5, pp. 427–437, 2008.

[44] M. Kahrobaiyan, M. Rahaeifard, S. Tajalli, and M. Ahmadian, “A strain gradient functionally graded euler–bernoulli beam formulation,” *International Journal of Engineering Science*, vol. 52, pp. 65–76, 2012.

[45] M. Kahrobaiyan, M. Asghari, M. Rahaeifard, and M. Ahmadian, “A nonlinear strain gradient beam formulation,” *International Journal of Engineering Science*, vol. 49, no. 11, pp. 1256–1267, 2011.

[46] J. Zhao, S. Zhou, B. Wang, and X. Wang, “Nonlinear microbeam model based on strain gradient theory,” *Applied Mathematical Modelling*, vol. 36, no. 6, pp. 2674–2686, 2012.

[47] R. Ansari, R. Gholami, and S. Sahmani, “Free vibration analysis of size-dependent functionally graded microbeams based on the strain gradient timoshenko beam theory,” *Composite Structures*, vol. 94, no. 1, pp. 221–228, 2011.

[48] B. Wang, J. Zhao, and S. Zhou, “A micro scale timoshenko beam model based on strain gradient elasticity theory,” *European Journal of Mechanics - A/Solids*, vol. 29, no. 4, pp. 591–599, 2010.

[49] B. Wang, M. Liu, and J. e. a. Zhao, “A size-dependent reddy–levinson beam model based on a strain gradient elasticity theory,” *Meccanica*, vol. 49, pp. 1427–1441, 2014.

[50] A. Karamanli and T. P. Vo, “Size-dependent behaviour of functionally graded sandwich microbeams based on the modified strain gradient theory,” *Composite Structures*, vol. 246, p. 112401, 2020.

[51] B. Akgöz and Ömer Civalek, “Bending analysis of embedded carbon nanotubes resting on an elastic foundation using strain gradient theory,” *Acta Astronautica*, vol. 119, pp. 1–12, 2016.

[52] R. Ansari, R. Gholami, and M. A. Darabi, “A nonlinear timoshenko beam formulation based on strain gradient theory,” *Journal of Mechanics of Materials and Structures*, vol. 7, no. 2, pp. 195–211, 2012.

[53] R. Aghazadeh, S. Dag, and E. Cigeroglu, “Thermal effect on bending, buckling and free vibration of functionally graded rectangular micro-plates possessing a variable length scale parameter,” *Microsyst Technol*, vol. 24, p. 3549–3572, 2018.

[54] K. Lazopoulos, “On bending of strain gradient elastic micro-plates,” *Mechanics Research Communications*, vol. 36, no. 7, pp. 777–783, 2009.

[55] S. Ramezani, “Nonlinear vibration analysis of micro-plates based on strain gradient elasticity theory,” *Nonlinear Dyn*, vol. 73, p. 1399–1421, 2013.

[56] X. Ji, A. Li, and S. Zhou, “A comparison of strain gradient theories with applications to the functionally graded circular micro-plate,” *Applied Mathematical Modelling*, vol. 49, pp. 124–143, 2017.

[57] M. A. Roudbari, T. D. Jorshari, C. Lü, R. Ansari, A. Z. Kouzani, and M. Amabili, “A review of size-dependent continuum mechanics models for micro- and nano-structures,” *Thin-Walled Structures*, vol. 170, p. 108562, 2022.

[58] H.-T. Thai, T. P. Vo, T.-K. Nguyen, and S.-E. Kim, “A review of continuum mechanics models for size-dependent analysis of beams and plates,” *Composite Structures*, vol. 177, pp. 196–219, 2017.

[59] B. WenXing, Z. ChangChun, and C. WanZhao, “Simulation of young’s modulus of single-walled carbon nanotubes by molecular dynamics,” *Physica B: Condensed Matter*, vol. 352, no. 1, pp. 156–163, 2004.

[60] S. Silling, “Reformulation of elasticity theory for discontinuities and long-range forces,” *Journal of the Mechanics and Physics of Solids*, vol. 48, no. 1, pp. 175–209, 2000.

[61] S. Silling and E. Askari, “A meshfree method based on the peridynamic model of solid mechanics,” *Computers & Structures*, vol. 83, no. 17, pp. 1526–1535, 2005.

[62] A. C. Eringen, “Linear theory of nonlocal elasticity and dispersion of plane waves,” *International Journal of Engineering Science*, vol. 10, p. 425 – 435, 1972.

[63] A. C. Eringen, “On differential equations of nonlocal elasticity and solutions of screw dislocation and surface waves,” *Journal of Applied Physics*, vol. 54, no. 9, p. 4703 – 4710, 1983.

[64] J. Peddieson, G. R. Buchanan, and R. P. McNitt, “Application of nonlocal continuum models to nanotechnology,” *International Journal of Engineering Science*, vol. 41, no. 3, pp. 305–312, 2003.

[65] J. Reddy, “Nonlocal theories for bending, buckling and vibration of beams,” *International Journal of Engineering Science*, vol. 45, no. 2, pp. 288–307, 2007.

[66] J. N. Reddy and S. D. Pang, “Nonlocal continuum theories of beams for the analysis of carbon nanotubes,” *Journal of Applied Physics*, vol. 103, p. 023511, 01 2008.

[67] J. Reddy, “Nonlocal nonlinear formulations for bending of classical and shear deformation theories of beams and plates,” *International Journal of Engineering Science*, vol. 48, no. 11, pp. 1507–1518, 2010. Special Issue in Honor of K.R. Rajagopal.

[68] W. H. Duan, C. M. Wang, and Y. Y. Zhang, "Calibration of nonlocal scaling effect parameter for free vibration of carbon nanotubes by molecular dynamics," *Journal of Applied Physics*, vol. 101, no. 2, p. 024305, 2007.

[69] J. Yang, L. Ke, and S. Kitipornchai, "Nonlinear free vibration of single-walled carbon nanotubes using nonlocal timoshenko beam theory," *Physica E: Low-dimensional Systems and Nanostructures*, vol. 42, no. 5, pp. 1727–1735, 2010.

[70] H.-T. Thai, "A nonlocal beam theory for bending, buckling, and vibration of nanobeams," *International Journal of Engineering Science*, vol. 52, pp. 56–64, 2012.

[71] A. A. Ghassabı, S. Dağ, and E. Ciğeroğlu, "Free vibration analysis of functionally graded rectangular nanoplates considering spatial variation of the nonlocal parameter," *Archieves OF Mechanics*, p. 105–130, 2017.

[72] I. Belkorissat, M. S. A. Houari, A. Tounsi, E. A. A. Bedia, and S. R. Mahmoud, "On vibration properties of functionally graded nano-plate using a new nonlocal refined four variable model," *Steel and Composite Structures*, vol. 18, pp. 1063–1081, 2015.

[73] N. Challamel and C. M. Wang, "The small length scale effect for a non-local cantilever beam: a paradox solved," *Nanotechnology*, vol. 19, p. 345703, jul 2008.

[74] A. Norouzzadeh and R. Ansari, "Finite element analysis of nano-scale timoshenko beams using the integral model of nonlocal elasticity," *Physica E: Low-dimensional Systems and Nanostructures*, vol. 88, pp. 194–200, 2017.

[75] J. Fernández-Sáez, R. Zaera, J. Loya, and J. Reddy, "Bending of euler–bernoulli beams using eringen's integral formulation: A paradox resolved," *International Journal of Engineering Science*, vol. 99, pp. 107–116, 2016.

[76] C. Lim, G. Zhang, and J. Reddy, "A higher-order nonlocal elasticity and strain gradient theory and its applications in wave propagation," *Journal of the Mechanics and Physics of Solids*, vol. 78, pp. 298–313, 2015.

[77] M. Mohammadian, "Application of the modified fourier series method and the genetic algorithm for calibration of small-scale parameters in the nonlocal

strain gradient nanobeams," *Mathematical Methods in the Applied Sciences*, vol. 45, no. 10, pp. 6325–6345, 2022.

[78] L. Li and Y. Hu, "Wave propagation in fluid-conveying viscoelastic carbon nanotubes based on nonlocal strain gradient theory," *Computational Materials Science*, vol. 112, pp. 282–288, 2016.

[79] K. Ghorbani, A. Rajabpour, and M. Ghadiri, "Determination of carbon nanotubes size-dependent parameters: molecular dynamics simulation and nonlocal strain gradient continuum shell model," *Mechanics Based Design of Structures and Machines*, vol. 49, no. 1, pp. 103–120, 2021.

[80] P. Jankowski, K. K. Żur, and A. Farajpour, "Analytical and meshless dqm approaches to free vibration analysis of symmetric fgm porous nanobeams with piezoelectric effect," *Engineering Analysis with Boundary Elements*, vol. 136, pp. 266–289, 2022.

[81] X. Li, L. Li, Y. Hu, Z. Ding, and W. Deng, "Bending, buckling and vibration of axially functionally graded beams based on nonlocal strain gradient theory," *Composite Structures*, vol. 165, pp. 250–265, 2017.

[82] A. M. Fattahi, S. Sahmani, and N. A. Ahmed, "Nonlocal strain gradient beam model for nonlinear secondary resonance analysis of functionally graded porous micro/nano-beams under periodic hard excitations," *Mechanics Based Design of Structures and Machines*, vol. 48, no. 4, pp. 403–432, 2020.

[83] M. Şimşek, "Nonlinear free vibration of a functionally graded nanobeam using nonlocal strain gradient theory and a novel hamiltonian approach," *International Journal of Engineering Science*, vol. 105, pp. 12–27, 2016.

[84] L. Li and Y. Hu, "Buckling analysis of size-dependent nonlinear beams based on a nonlocal strain gradient theory," *International Journal of Engineering Science*, vol. 97, pp. 84–94, 2015.

[85] B. Karami, D. Shahsavari, and L. Li, "Hygrothermal wave propagation in viscoelastic graphene under in-plane magnetic field based on nonlocal strain gradient theory," *Physica E: Low-dimensional Systems and Nanostructures*, vol. 97, pp. 317–327, 2018.

[86] D. Shahsavari, B. Karami, and L. Li, “Damped vibration of a graphene sheet using a higher-order nonlocal strain-gradient kirchhoff plate model,” *Comptes Rendus Mécanique*, vol. 346, no. 12, pp. 1216–1232, 2018.

[87] L. Wang and H. Hu, “Flexural wave propagation in single-walled carbon nanotubes,” *Phys. Rev. B*, vol. 71, p. 195412, May 2005.

[88] J. Yoon, C. Ru, and A. Mioduchowski, “Vibration and instability of carbon nanotubes conveying fluid,” *Composites Science and Technology*, vol. 65, no. 9, pp. 1326–1336, 2005. MM2003.

[89] M. P. Païdoussis, *Fluid–Structure Interactions: Slender Structures and Axial Flow*, vol. 1. Academic Press, 1998.

[90] C. Guo, C. Zhang, and M. Païdoussis, “Modification of equation of motion of fluid-conveying pipe for laminar and turbulent flow profiles,” *Journal of Fluids and Structures*, vol. 26, no. 5, pp. 793–803, 2010.

[91] G. E. K. Ali Beskok, “Report: A model for flows in channels, pipes, and ducts at micro and nano scales,” *Microscale Thermophysical Engineering*, vol. 3, no. 1, pp. 43–77, 1999.

[92] V. Rashidi, H. R. Mirdamadi, and E. Shirani, “A novel model for vibrations of nanotubes conveying nanoflow,” *Computational Materials Science*, vol. 51, no. 1, pp. 347–352, 2012.

[93] M. Mahinzare, K. Mohammadi, M. Ghadiri, and A. Rajabpour, “Size-dependent effects on critical flow velocity of a swcnt conveying viscous fluid based on nonlocal strain gradient cylindrical shell model,” *Microfluidics and Nanofluidics*, vol. 21, 2017.

[94] M. R. Bidgoli, M. S. Karimi, and A. G. Arani, “Nonlinear vibration and instability analysis of functionally graded cnt-reinforced cylindrical shells conveying viscous fluid resting on orthotropic pasternak medium,” *Mechanics of Advanced Materials and Structures*, vol. 23, no. 7, pp. 819–831, 2016.

[95] Q. Ni, Z. Zhang, and L. Wang, “Application of the differential transformation method to vibration analysis of pipes conveying fluid,” *Applied Mathematics and Computation*, vol. 217, no. 16, pp. 7028–7038, 2011.

[96] L. Wang, Q. Ni, M. Li, and Q. Qian, “The thermal effect on vibration and instability of carbon nanotubes conveying fluid,” *Physica E: Low-dimensional Systems and Nanostructures*, vol. 40, no. 10, pp. 3179–3182, 2008.

[97] E. Ghavanloo, F. Daneshmand, and M. Rafiei, “Vibration and instability analysis of carbon nanotubes conveying fluid and resting on a linear viscoelastic winkler foundation,” *Physica E: Low-dimensional Systems and Nanostructures*, vol. 42, no. 9, pp. 2218–2224, 2010.

[98] H.-L. Lee and W.-J. Chang, “Free transverse vibration of the fluid-conveying single-walled carbon nanotube using nonlocal elastic theory,” *Journal of Applied Physics*, vol. 103, p. 024302, 01 2008.

[99] H. Dai, L. Wang, A. Abdelkefi, and Q. Ni, “On nonlinear behavior and buckling of fluid-transporting nanotubes,” *International Journal of Engineering Science*, vol. 87, pp. 13–22, 2015.

[100] H. Askari and E. Esmailzadeh, “Forced vibration of fluid conveying carbon nanotubes considering thermal effect and nonlinear foundations,” *Composites Part B: Engineering*, vol. 113, pp. 31–43, 2017.

[101] A. H. Nayfeh and D. T. Mook, *Nonlinear Oscillations*. John Wiley & Sons, Ltd, 1995.

[102] L. Wang, “Size-dependent vibration characteristics of fluid-conveying microtubes,” *Journal of Fluids and Structures*, vol. 26, no. 4, pp. 675–684, 2010.

[103] R. Aghazadeh, “Stability analysis of fluid conveying axially functionally graded micro-pipes using a refined tube model,” *Arab J Sci Eng*, vol. 47, p. 8739–8750, 2022.

[104] R. Ansari, A. Norouzzadeh, R. Gholami, M. Faghih Shojaei, and M. Hosseinzadeh, “Size-dependent nonlinear vibration and instability of embedded fluid-conveying swbnnts in thermal environment,” *Physica E: Low-dimensional Systems and Nanostructures*, vol. 61, pp. 148–157, 2014.

[105] K. Mohammadi, A. Rajabpour, and M. Ghadiri, “Calibration of nonlocal strain gradient shell model for vibration analysis of a cnt conveying viscous

fluid using molecular dynamics simulation," *Computational Materials Science*, vol. 148, pp. 104–115, 2018.

[106] L. Li, Y. Hu, X. Li, and L. Ling, "Size-dependent effects on critical flow velocity of fluid-conveying microtubes via nonlocal strain gradient theory," *Microfluid Nanofluid*, 2016.

[107] Y. Zhen and L. Zhou, "Wave propagation in fluid-conveying viscoelastic carbon nanotubes under longitudinal magnetic field with thermal and surface effect via nonlocal strain gradient theory," *Modern Physics Letters B*, vol. 31, no. 08, p. 1750069, 2017.

[108] A. Farajpour, H. Farokhi, M. H. Ghayesh, and S. Hussain, "Nonlinear mechanics of nanotubes conveying fluid," *International Journal of Engineering Science*, vol. 133, pp. 132–143, 2018.

[109] R. Bahaadini, A. R. Saidi, and M. Hosseini, "Flow-induced vibration and stability analysis of carbon nanotubes based on the nonlocal strain gradient timoshenko beam theory," *Journal of Vibration and Control*, vol. 25, no. 1, pp. 203–218, 2019.

[110] A. Farajpour, H. Farokhi, and M. H. Ghayesh, "Chaotic motion analysis of fluid-conveying viscoelastic nanotubes," *European Journal of Mechanics - A/Solids*, vol. 74, pp. 281–296, 2019.

[111] M. Ghane, A. R. Saidi, and R. Bahaadini, "Vibration of fluid-conveying nanotubes subjected to magnetic field based on the thin-walled timoshenko beam theory," *Applied Mathematical Modelling*, vol. 80, pp. 65–83, 2020.

[112] M. Atashafrooz, R. Bahaadini, and H. R. Sheibani, "Nonlocal, strain gradient and surface effects on vibration and instability of nanotubes conveying nanoflow," *Mechanics of Advanced Materials and Structures*, vol. 27, no. 7, pp. 586–598, 2020.

[113] Q. Jin and Y. Ren, "Nonlinear size-dependent bending and forced vibration of internal flow-inducing pre- and post-buckled fg nanotubes," *Communications in Nonlinear Science and Numerical Simulation*, vol. 104, p. 106044, 2022.

[114] S. Chen and Y. K. Cheung, “A modified lindstedt–poincaré method for a strongly nonlinear system with quadratic and cubic nonlinearities,” *Shock and Vibration*, 1996.

[115] G. Karniadakis, A. Beskok, and N. Aluru, *Microflows and Nanoflows Fundamentals and Simulation*, vol. 29. Springer, 2005.

[116] J. N. Israelachvili, “Adhesion forces between surfaces in liquids and condensable vapours,” *Surface Science Reports*, vol. 14, pp. 109–159, 1992.

[117] J. A. Thomas and A. J. McGaughey, “Water flow in carbon nanotubes: Transition to subcontinuum transport,” *Physical Review Letters*, vol. 102, 5 2009.

[118] G. Hummer, J. C. Rasaiah, and J. P. Noworyta, “Water conduction through the hydrophobic channel of a carbon nanotube,” *Letters to Nature*, 2001.

[119] M. Majumder, N. Chopra, R. Andrews, and B. J. Hinds, “Enhanced flow in carbon nanotube,” *Nature*, vol. 438, 2005.

[120] “Fast mass transport through sub-2-nanometer carbon nanotubes,” *Science*, vol. 312, pp. 1034–1037, 5 2006.

[121] J. A. Thomas, A. J. McGaughey, and O. Kuter-Arnebeck, “Pressure-driven water flow through carbon nanotubes: Insights from molecular dynamics simulation,” *International Journal of Thermal Sciences*, vol. 49, pp. 281–289, 2 2010.

[122] “How fast does water flow in carbon nanotubes?,” *Journal of Chemical Physics*, vol. 138, 3 2013.

[123] K. Falk, F. Sedlmeier, L. Joly, R. R. Netz, and L. Bocquet, “Molecular origin of fast water transport in carbon nanotube membranes: Superlubricity versus curvature dependent friction,” *Nano Letters*, vol. 10, no. 10, pp. 4067–4073, 2010.

[124] J. L. Rivera and F. W. Starr, “Rapid transport of water via a carbon nanotube syringe,” *The Journal of Physical Chemistry C*, vol. 114, no. 9, pp. 3737–3742, 2010.

[125] V. Neklyudov and V. Freger, “Water and ion transfer to narrow carbon nanotubes: Roles of exterior and interior,” *The Journal of Physical Chemistry Letters*, vol. 12, no. 1, pp. 185–190, 2021.

[126] C. W. Bert and M. Malik, “Differential quadrature method in computational mechanics: A review,” *Applied Mechanics Reviews*, vol. 49, pp. 1–28, 1996.

[127] C. Shu, *Differential Quadrature and Its Application in Engineering*. Springer London, 2000.

[128] S. S. Rao, *Vibration of Continuous Systems*. John Wiley & Sons, 2007.

[129] B. Yagci, S. Filiz, L. L. Romero, and O. B. Ozdoganlar, “A spectral-tchebychev technique for solving linear and nonlinear beam equations,” *Journal of Sound and Vibration*, vol. 321, no. 1, pp. 375–404, 2009.

[130] R. Horn, *Topics in Matrix Analysis*, pp. 304–307. Cambridge University Press, 1994.

[131] O. Tanrikulu, B. Kuran, H. N. Ozguven, and M. Imregun, “Forced harmonic response analysis of nonlinear structures using describing functions,” *AIAA journal*, vol. 31, no. 7, pp. 1313–1320, 1993.

[132] S. C. Chapra and R. P. Canale, *Numerical Methods for Engineers*. McGraw-Hill Education, 7 ed., 2015.

[133] T. M. Inc., “Matlab version: 9.13.0.2105380 (r2022b) update 2,” 2022.

[134] E. C. Aifantis, “On the role of gradients in the localization of deformation and fracture,” *International Journal of Engineering Science*, vol. 30, no. 10, pp. 1279–1299, 1992.

[135] G. Kösterit and E. Cigeroglu, “Determination of flutter speed of 2d nonlinear wing by using describing function method and state-space formulation,” in *Nonlinear Structures & Systems, Volume 1: Proceedings of the 40th IMAC, A Conference and Exposition on Structural Dynamics 2022*, pp. 101–107, Springer, 2022.

[136] S. Timoshenko, “Lxvi. on the correction for shear of the differential equation for transverse vibrations of prismatic bars,” *The London, Edinburgh, and*

Dublin Philosophical Magazine and Journal of Science, vol. 41, no. 245, pp. 744–746, 1921.

[137] J. W.-Z. Zu and R. P. S. Han, “Natural Frequencies and Normal Modes of a Spinning Timoshenko Beam With General Boundary Conditions,” *Journal of Applied Mechanics*, vol. 59, pp. S197–S204, 06 1992.

[138] E. Cigeroglu and H. Samandari, “Nonlinear free vibration of double walled carbon nanotubes by using describing function method with multiple trial functions,” *Physica E: Low-dimensional Systems and Nanostructures*, vol. 46, pp. 160–173, 2012.

APPENDIX A

TIME DOMAIN RESPONSE INVESTIGATION

A.1 Natural Frequency Estimation Method

Assuming response can be simplify modeled to includes two harmonic functions with two different frequencies where one is more dominant in amplitude as,

$$x(t) = \sin 10.8t + 0.2 \sin 40t, \qquad \dot{x}(t) = 10.8 \cos 10.8t + 8 \cos 40t \tag{A.1}$$

where $10.8\ rad/s$ is chosen such that it does not coincide with the FFT sampling frequency since that would be a more general case. Velocity response and smoothed version as well as the zoomed in view can be seen for 20 seconds of measurement with 10000 sampling points to ensure smoothness in the figure A.1.

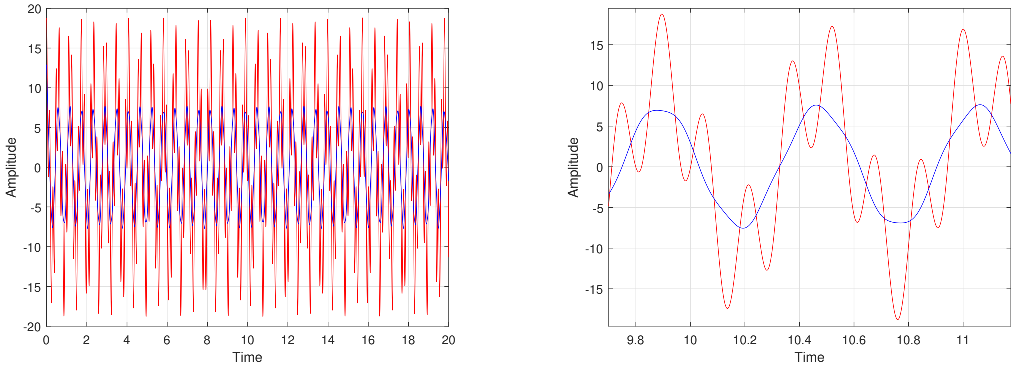

(a) Full Size

(b) Zoomed

Figure A.1: Total (a) and a zoomed portion (b) of the velocity

By comparing the points that crosses zero with linear interpolation between two closest points, peak to peak period and hence peak to peak frequency of the response can be found. If each frequency point is plotted for the corresponding peak points, change of frequency can be seen through the time as in the figure A.2.

Even though, obvious harmonic spread can be seen, if instead it is assumed as to be distributed normally, a mean and a standard deviation to the estimate can be found and for the given smoothing it is found as $10.82 \pm 0.02\ rad/s$. If instead frequency component analysis using FFT is conducted, point of the first peak corresponds to $10.67\ rad/s$ while the next closest frequency data is $10.98\ rad/s$, if instead a Nyquist fit is performed and peak frequency is calculated that way it would improve the guess. However, similar improvement can be done by repeating the estimation analysis for several smoothing ranges and increasing the data size with still taking less time then FFT. As it is important for the accuracy, different smoothing ranges might produce different estimates with better or worse uncertainties attached with it.

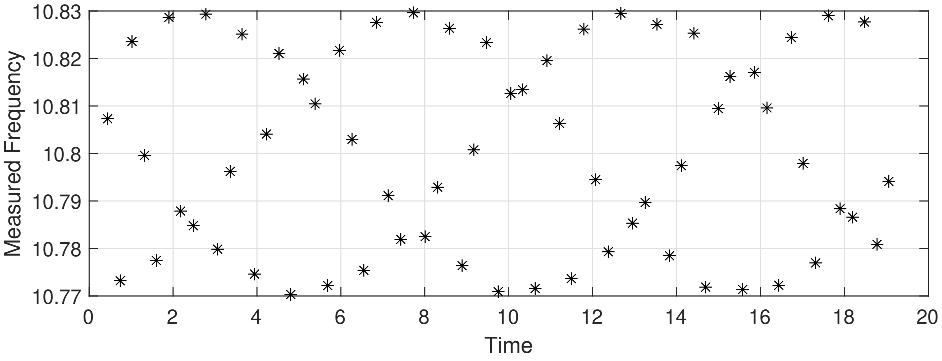

Figure A.2: Frequency estimation in time

Even though not used for the analysis at hand to capture the correct values at all times, proposed method can also be used to capture the change of frequency over time. If the response frequency is modified to increase linearly until $13.4\ rad/s$, frequency estimation change in time can be seen in the figure A.3. Increase in time is obvious however, due to smoothing, there is an overshoot until the increase of the frequency stops, which could not be fixed and occurs irrespective of the type of smoothing used. In any case, it can capture moving natural frequencies and can differentiate the final frequency while FFT has no such capabilities but only smears the peak.

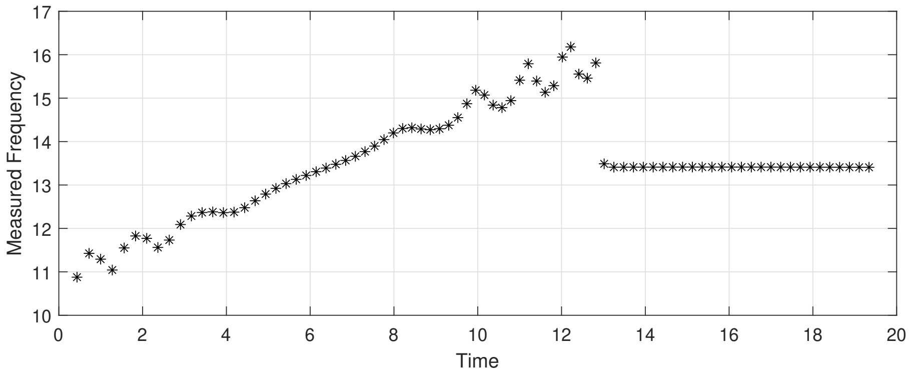

Figure A.3: Frequency estimation in time while the vibration frequency is changing

A.2 Different Flow Profiles and the Response

There are two flow profiles that are used to obtain time domain verification and one flow profile to be used in this appendix to be used to approximate a real-life case. Linear increase and constant speed profiles refers to a linear increase and a direct jump to the higher velocity which can be shown for a representative speed as in the figure A.4. Time domain response to both of these flow profiles is shown in the figure A.5. By looking at each response, it is apparent that one vibrates around the buckled state while the other is chaotically vibrating, where even the motion characteristic itself is changing from flutter to buckling on its own.

Motion of the two profile can better be shown if some sample of the total beam motion can be taken and plotted for some time values as given in the figure A.6. Traveling wave like solution is apparent by looking at the consecutive time slices, while on the other hand, vibration around the buckled configuration that assumes the first mode shape is clear.

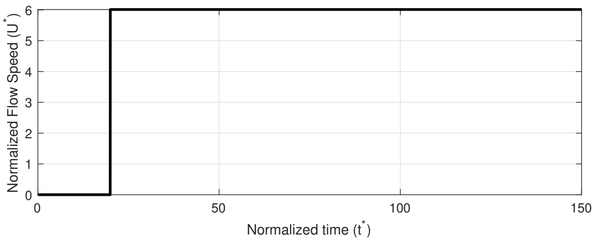

(a) Constant Speed Profile

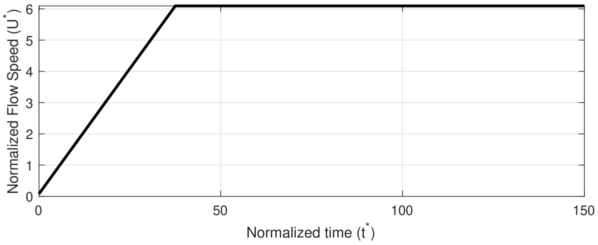

(b) Linear Speed Profile

Figure A.4: Change of speed for constant discontinuous (a) and linearly increasing (b) speed profiles

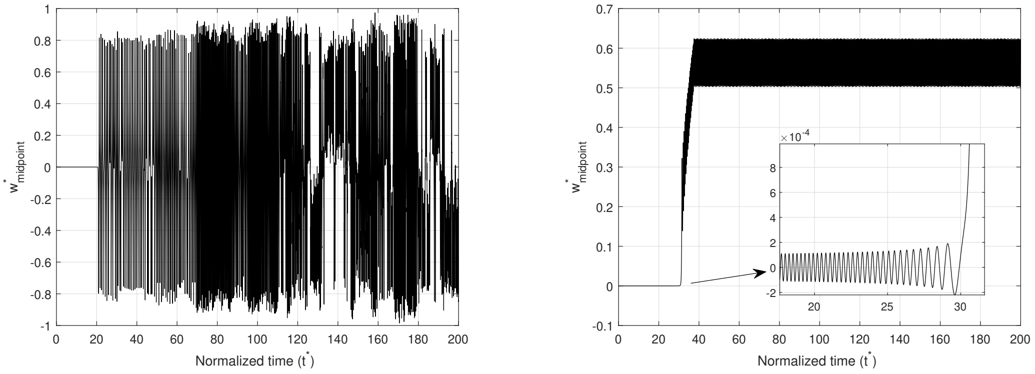

(a) Constant Speed Profile

(b) Linear Speed Profile

Figure A.5: Response of the midpoint for constant discontinuous (a) and linearly increasing (b) speed profiles

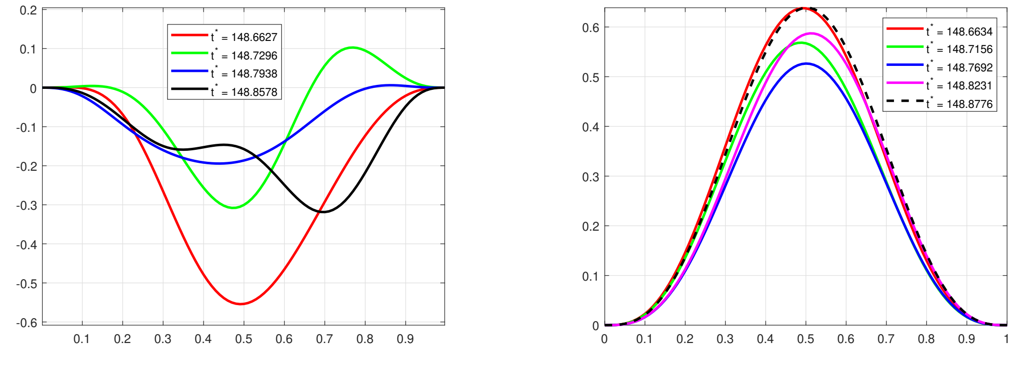

(a) Constant Speed Profile (b) Linear Speed Profile

Figure A.6: Total motion of the beam for constant discontinuous (a) and linearly increasing (b) speed profiles

Moreover phase plane portrait of the two motion is shown in the figure A.7 for the total simulation time and over shooting of the constant profile to a semi-stable fluttering orbit can be seen while the linear profile buckles with lower vibration amplitude.

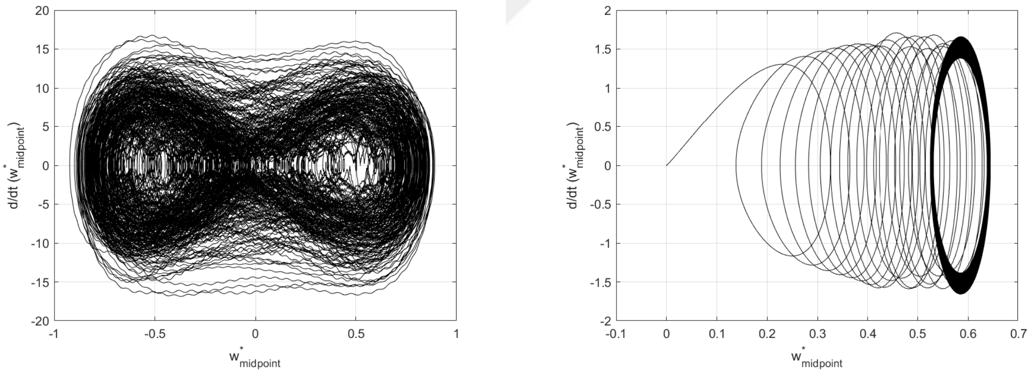

(a) Constant Speed Profile (b) Linear Speed Profile

Figure A.7: Phase plane portrait for constant discontinuous (a) and linearly increasing (b) speed profiles

Finally, characteristics of motion can be better understood if the operating MAC number is plotted against time as in figure A.8, with heavy smoothing, since amplitude of oscillation determines the strength of each MAC number in a cycle. Even with heavy smoothing after experiencing flutter, MAC number wildly changes even getting closer to buckled MAC number distribution at some points. Most importantly it contains the effects of the second mode while the buckled state nearly have none.

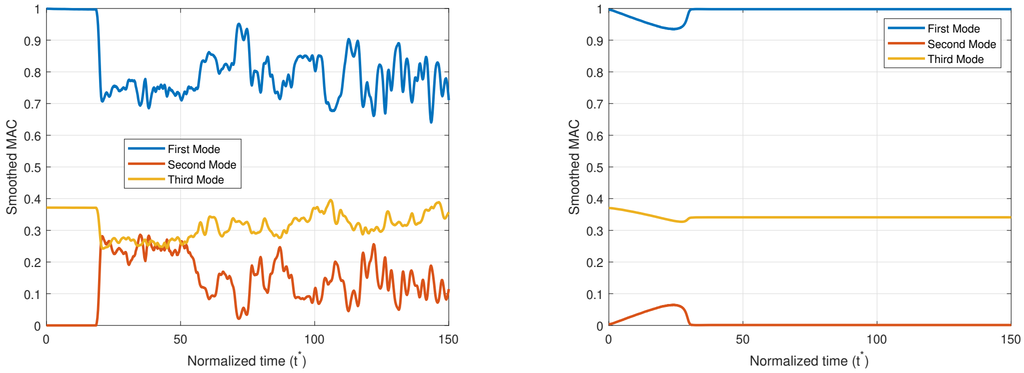

(a) Constant Speed Profile

(b) Linear Speed Profile

Figure A.8: MAC number for constant discontinuous (a) and linearly increasing (b) speed profiles

More realistic of the situation can be found by examining a more realistic flow profile where a sudden increase with the approximate shape of a normal distribution reaches the same speed and returns to normal as given in the figure A.9. With this profile, tendency to flutter or buckle is better understood since critical motion is not kept and transient part can give enough information.

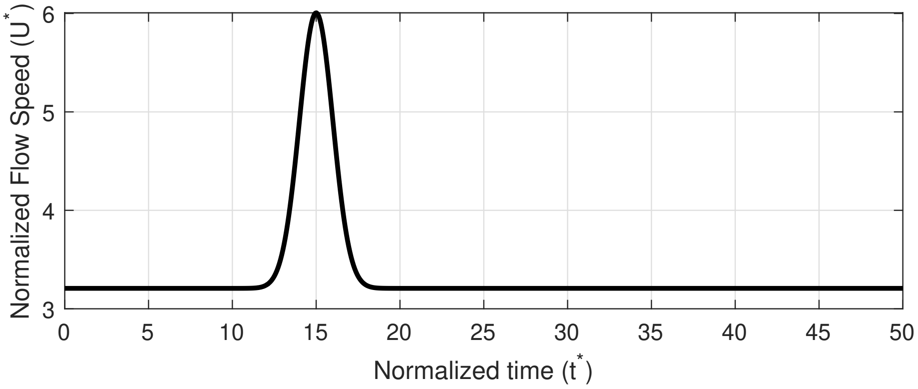

Figure A.9: Change of speed for a normally distributed peak

Response is as given in the figure A.10, and clear buckling behaviour is visible before returning to normal but with bigger vibration amplitude. Since buckling is favored more realistic test profile is deemed as linearly increasing one not only due to the more realistic velocity change but also having a higher tendency to buckle.

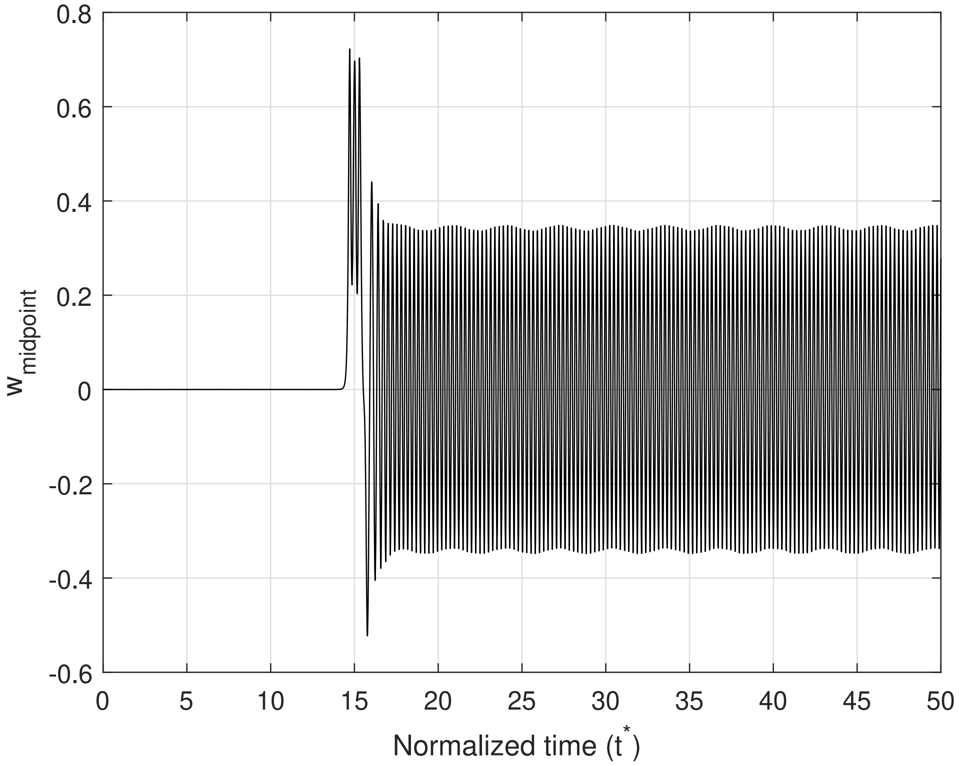

Figure A.10: Response of the midpoint of the beam for a normally distributed peak

Change of speed needed to change the regime from buckling to flutter needs to be examined, for that assume an accelerating velocity profile capping at a prescribed speed as,

$$U(t) = \begin{cases} at & \text{if } at < U_{max} \\ U_{max} & \text{if } at \geq U_{max} \end{cases} \tag{A.2}$$

where a is the acceleration and U_{max} is the maximum reached speed. In the figure A.11 maximum and mean values of the time simulation results are given where for $a = 2$ response changes from buckling to flutter. Considering non normalized acceleration would be around $a \sim 4 * 10^{13} m/s^2$, taking the normal linearly increasing case to be the realistic result is again verified.

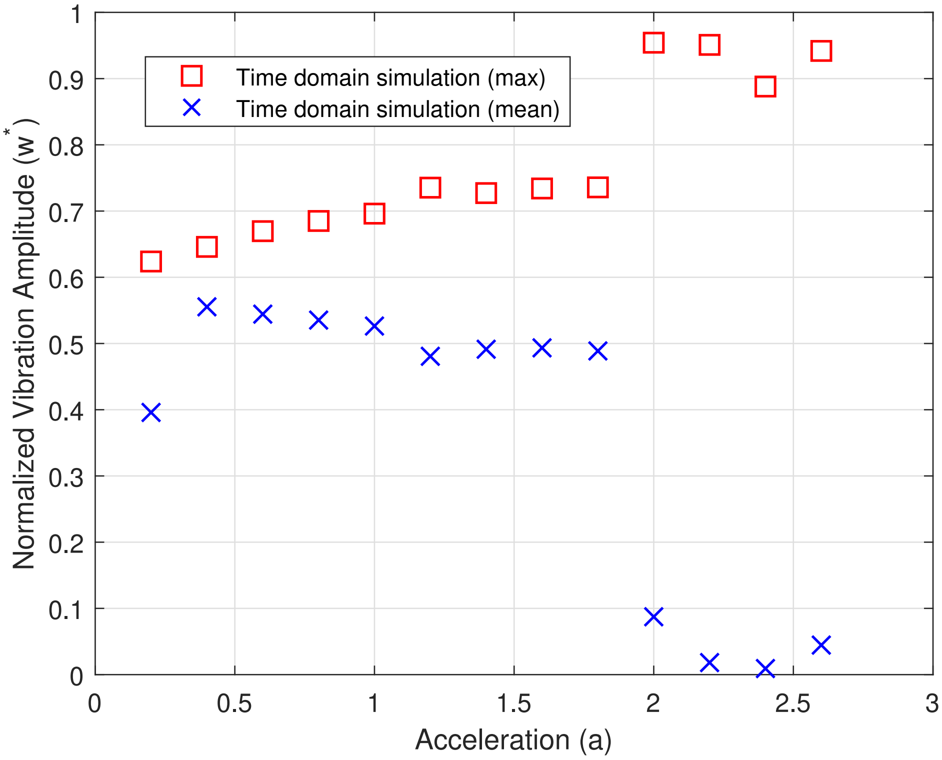

Figure A.11: Response of the midpoint of the beam for different acceleration values of the linearly increasing speed profile

APPENDIX B

DERIVATION OF HARMONIC BALANCE METHOD

Starting with the form of the response dependent constant integral as,

$$C = \frac{1}{2} S \int_0^1 \left(\frac{\partial w^*}{\partial x^*}\right)^2 dx^* = \frac{1}{2} S \int_0^1 \left(\frac{\partial w^*}{\partial x^*}\right)\left(\frac{\partial w^*}{\partial x^*}\right) dx^* \tag{B.1}$$

Using GtDQM framework and employing integral of products rule of equation (3.43), equation (B.1) can be written as,

$$C = \frac{1}{2} S \int_0^1 \left(\frac{\partial w^*}{\partial x^*}\right)\left(\frac{\partial w^*}{\partial x^*}\right) dx^* = \left(\boldsymbol{A}^{(1)}\boldsymbol{w}\right)^T \boldsymbol{P}\left(\boldsymbol{A}^{(1)}\boldsymbol{w}\right) \tag{B.2}$$

Where the deflection w can be spatially discretized and utilizing separation of variables it can be written as,

$$w(x,t) \quad \rightarrow \quad \boldsymbol{w} = \boldsymbol{w_s}\sin\omega t + \boldsymbol{w_c}\cos\omega t = \boldsymbol{T}\boldsymbol{w_{d_s}}\sin\omega t + \boldsymbol{T}\boldsymbol{w_{d_c}}\cos\omega t \tag{B.3}$$

Substituting equation (B.3) in to the equation (B.2) it can be written as

$$\left(\boldsymbol{A}^{(1)}\boldsymbol{T}\boldsymbol{w_{d_s}}\sin\omega t + \boldsymbol{T}\boldsymbol{w_{d_c}}\cos\omega t\right)^T \boldsymbol{P}\left(\boldsymbol{A}^{(1)}\boldsymbol{T}\boldsymbol{w_{d_s}}\sin\omega t + \boldsymbol{T}\boldsymbol{w_{d_c}}\cos\omega t\right) \tag{B.4}$$

which multiplication can be expended as,

$$\begin{aligned} C =& \boldsymbol{w}^T_{\boldsymbol{d_s}}\boldsymbol{T}^T\boldsymbol{A}^{(1)^{\boldsymbol{T}}}P\boldsymbol{A}^{(1)}\boldsymbol{T}\boldsymbol{w_{d_s}}\sin^2\omega t + \\ & \boldsymbol{w}^T_{\boldsymbol{d_s}}\boldsymbol{T}^T\boldsymbol{A}^{(1)^{\boldsymbol{T}}}P\boldsymbol{A}^{(1)}\boldsymbol{T}\boldsymbol{w_{d_c}}\sin\omega t\cos\omega t + \\ & \boldsymbol{w}^T_{\boldsymbol{d_c}}\boldsymbol{T}^T\boldsymbol{A}^{(1)^{\boldsymbol{T}}}P\boldsymbol{A}^{(1)}\boldsymbol{T}\boldsymbol{w_{d_c}}\cos^2\omega t + \\ & \boldsymbol{w}^T_{\boldsymbol{d_c}}\boldsymbol{T}^T\boldsymbol{A}^{(1)^{\boldsymbol{T}}}P\boldsymbol{A}^{(1)}\boldsymbol{T}\boldsymbol{w_{d_s}}\cos\omega t\sin\omega t \end{aligned} \tag{B.5}$$

This equation can be simplified by defining a β^{ij} as,

$$\beta^{ij} = \frac{1}{2} S\left(\boldsymbol{A}^{(1)}\boldsymbol{T}\boldsymbol{w_{d_i}}\right)^T \boldsymbol{P}\left(\boldsymbol{A}^{(1)}\boldsymbol{T}\boldsymbol{w_{d_j}}\right) \tag{B.6}$$

where i, j refers to sine, or cosine coefficients and can also be used as n^th sine or cosine coefficient if multi HBM is used. Substituting the definition in to the equation (B.5),

$$C = \beta^{ss}\sin^2\omega t + (\beta^{sc} + \beta^{cs})\sin\omega t\cos\omega t + \beta^{cc}\cos^2\omega t \tag{B.7}$$

Substituting this result into the normalized equation of motion of equation (3.97) and multiplying with $\boldsymbol{T}^T$

$$C\boldsymbol{T}^T\left(\boldsymbol{A^{(2)}} - \alpha^2\boldsymbol{A^{(4)}}\right)\left(\boldsymbol{T}\boldsymbol{w_{d_s}}\sin\omega t + \boldsymbol{T}\boldsymbol{w_{d_c}}\cos\omega t\right) \tag{B.8}$$

This multiplication can be done with any other order derivative as long as there is no time derivative involved, and if it is involved it can be written as,

$$C\boldsymbol{T}^T\left(\boldsymbol{A^{(2)}} - \alpha^2\boldsymbol{A^{(4)}}\right)\omega\eta^*\left(\boldsymbol{T}\boldsymbol{w_{d_s}}\cos\omega t - \boldsymbol{T}\boldsymbol{w_{d_c}}\sin\omega t\right) \tag{B.9}$$

expanding equation (B.8)

$$\begin{gathered}\boldsymbol{T}^T\left(\boldsymbol{A^{(2)}} - \alpha^2\boldsymbol{A^{(4)}}\right)\boldsymbol{T}\\ \left[\left(\beta^{ss}\sin^3\omega t + 2\beta^{sc}\sin^2\omega t\cos\omega t + \beta^{cc}\cos^2\omega t\sin\omega t\right)\boldsymbol{w_{d_s}} +\right.\\ \left.\left(\beta^{ss}\sin^2\omega t\cos\omega t + 2\beta^{sc}\sin\omega t\cos^2\omega t + \beta^{cc}\cos^3\omega t\right)\boldsymbol{w_{d_c}}\right]\end{gathered} \tag{B.10}$$

Using the trigonometric identities,

$$\begin{aligned}\sin^3\omega t &= \frac{1}{4}(3\sin\omega t - \sin 3\omega t)\\ \sin^2\omega t\cos\omega t &= \frac{1}{4}(\cos\omega t - \cos 3\omega t)\\ \sin\omega t\cos^2\omega t &= \frac{1}{4}(\sin\omega t + \sin 3\omega t)\\ \cos^3\omega t &= \frac{1}{4}(3\cos\omega t + \sin 3\omega t)\end{aligned} \tag{B.11}$$

Since, only single harmonic balance is used higher order harmonics (i.e., $3\omega t$) are ignored and substituted back into the equation (B.10) to obtain the single harmonic approximation of the nonlinearity at hand which directly produces nonlinear forcing term,

$$\begin{aligned}\boldsymbol{f_{NL}} =& \boldsymbol{T}^T\left(\boldsymbol{A^{(2)}} - \alpha^2\boldsymbol{A^{(4)}}\right)\boldsymbol{T}\\ &\left[\left(\beta^{ss}\frac{3}{4}\sin\omega t + 2\beta^{sc}\frac{1}{4}\cos\omega t + \beta^{cc}\frac{1}{4}\sin\omega t\right)\boldsymbol{w_{d_s}} +\right.\\ &\left.\left(\beta^{ss}\frac{1}{4}\cos\omega t + 2\beta^{sc}\frac{1}{4}\sin\omega t + \beta^{cc}\frac{3}{4}\cos\omega t\right)\boldsymbol{w_{d_c}}\right]\end{aligned} \tag{B.12}$$

which can equivalently can be written in terms of matrix form by separately considering sine coefficients and cosine coefficients,

$$\boldsymbol{f_{NL}} = \begin{bmatrix} \left(\frac{3}{4}\beta^{ss} + \frac{1}{4}\beta^{cc}\right)\boldsymbol{G} & \frac{1}{2}\beta^{sc}\boldsymbol{G} \\ \frac{1}{2}\beta^{sc}\boldsymbol{G} & \left(\frac{3}{4}\beta^{cc} + \frac{1}{4}\beta^{ss}\right)\boldsymbol{G} \end{bmatrix} \begin{Bmatrix} \boldsymbol{w_{d_s}} \\ \boldsymbol{w_{d_c}} \end{Bmatrix} \tag{B.13}$$

where $\boldsymbol{G}$ is the respective derivatives defined as,

$$\boldsymbol{G} = \boldsymbol{T}^T \left(\boldsymbol{A^{(2)}} - \alpha^2 \boldsymbol{A^{(4)}}\right)\boldsymbol{T} \tag{B.14}$$

Same can be calculated for equation (B.9)

$$\boldsymbol{f'_{NL}} = \omega\eta^* \begin{bmatrix} \frac{1}{2}\beta^{sc}\boldsymbol{G} & -\left(\frac{3}{4}\beta^{ss} + \frac{1}{4}\beta^{cc}\right)\boldsymbol{G} \\ \left(\frac{3}{4}\beta^{cc} + \frac{1}{4}\beta^{ss}\right)\boldsymbol{G} & -\frac{1}{2}\beta^{sc}\boldsymbol{G} \end{bmatrix} \begin{Bmatrix} \boldsymbol{w_{d_s}} \\ \boldsymbol{w_{d_c}} \end{Bmatrix} \tag{B.15}$$